Theory of Electronic States and Transport in Carbon Nanotubes

Tsuneya ANDO

Department of Physics, Tokyo Institute of Technology
2–12–1 Ookayama, Meguro-ku, Tokyo 152-8551

A brief review is given of electronic and transport properties of carbon nanotubes obtained mainly in a $\boldsymbol{k \cdot p}$ scheme. The topics include a giant Aharonov-Bohm effect on the band gap and a Landau-level formation in magnetic fields, magnetic properties, interaction effects on the band structure, optical absorption spectra, and exciton effects. Transport properties are also discussed including absence of backward scattering except for scatterers with a potential range smaller than the lattice constant, its extension to multi-channel cases, a conductance quantization in the presence of short-range and strong scatterers such as lattice vacancies, and transport across junctions between nanotubes with different diameters. A continuum model for phonons in the long-wavelength limit and the resistivity determined by phonon scattering is reviewed as well.

§1. Introduction

Graphite needles called carbon nanotubes (CN's) have been a subject of an extensive study. When discovered first by Iijima,[1,2] they were multi-wall nanotubes consisting of concentric tubes of two-dimensional (2D) graphite arranged in a helical fashion about the axis. The distance of adjacent sheets or walls is larger than the distance between nearest neighbor atoms in a graphite sheet and therefore electronic properties of multi-wall tubes are dominated by those of a single layer CN. Single-wall nanotubes were later produced.[3,4] The purpose of this paper is to give a brief review of theoretical study on electronic and transport properties of carbon nanotubes.

Carbon nanotubes can be either a metal or semiconductor, depending on their diameters and helical arrangement. The condition whether a CN is metallic or semiconducting can be obtained based on the band structure of a 2D graphite sheet and periodic boundary conditions along the circumference direction. This result was first predicted by means of a tight-binding model ignoring the effect of the tube curvature.[5-11]

These properties can be well reproduced in a $\boldsymbol{k \cdot p}$ method or an effective-mass approximation.[12] In fact, the effective-mass scheme has been used successfully in the study of wide varieties of electronic properties of CN. Some of such examples are magnetic properties[13] including the Aharonov-Bohm effect on the band gap, optical absorption spectra,[14] exciton effects,[15,16] interaction effects on band gaps,[17] lattice instabilities in the absence[18,19] and presence of a magnetic field,[20] magnetic properties of ensembles of nanotubes,[21] effects of spin-orbit interaction,[22] and electronic properties of nanotube caps.[23] The $\boldsymbol{k \cdot p}$ scheme is particularly useful for the study of transport properties including the absence of backward scattering,[24] the presence of a perfectly conducting channel,[25] and effects of strong and short-range scatterers such as lattice defects,[26] junctions and topological defects,[27] and a Stone-Wales defect.[28]

Long wavelength phonons and electron-phonon scattering have also been studied.[29]

In this paper we shall mainly discuss electronic states and transport properties of nanotubes obtained theoretically in the $\boldsymbol{k \cdot p}$ method. It is worth mentioning that several papers or books giving general reviews of electronic properties of nanotubes were published.[30-37] Various theoretical results obtained in other methods and many relevant experiments not discussed below are contained in these review articles.

Nanotubes have unique mechanical properties characterized by a huge Young's modulus, making them the material with the highest tensile strength known so far and capable of sustaining high strains without fracture. They are proposed as the functional units for the construction of the future molecular-scale machines. As highly robust mechanical structures, they are being used as probes in scanning tunneling microscopy and atomic force microscopy, tweezers used for atomic-scale manipulation, etc. Such topics will not be discussed here, however.

In §2 electronic states of 2D graphite or a graphene sheet are discussed first in a nearest-neighbor tight-binding model, then an effective-mass equation equivalent to that of a 2D neutrino is introduced, and a characteristic topological anomaly is discussed. In §3 the band structure of nanotubes are discussed first from a general point of view and then based on the effective-mass scheme. An Aharonov-Bohm effect and formation of Landau levels in magnetic fields are discussed together with effects of trigonal warping, finite curvature, and strain. In §4 a short description is made on magnetic response of nanotubes. In §5 optical absorption is discussed in the effective-mass scheme and the nanotube is shown to behave differently in light polarization parallel or perpendicular to the axis. In §6 the importance of exciton effects and electron-electron interaction on band gaps is emphasized and some related experiments are
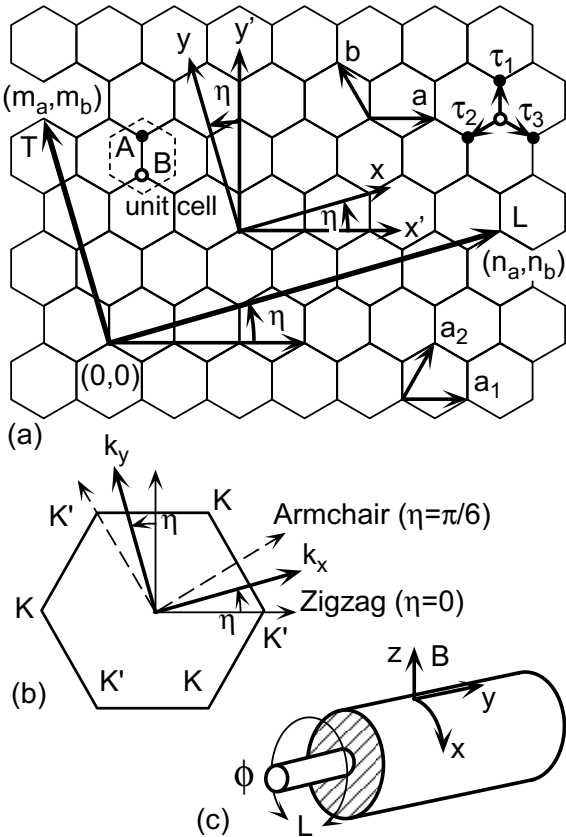
Fig. 1   (a) The lattice structure of 2D graphite and the
coordinate system. Two primitive translation vectors
are denoted by $\boldsymbol{a}$ and $\boldsymbol{b}$. A hexagonal unit cell repre-
sented by a dashed line contains two carbon atoms de-
noted by A and B. Three vectors directed from a B site
to nearest neighbor A sites are given by $\vec{\tau}_l$ ($l=1,2,3$).
A nanotube is specified by a chiral vector $\boldsymbol{L}$ corre-
sponding to the circumference of the nanotube with
$\boldsymbol{T}$ being a primitive translation vector perpendicular
to $\boldsymbol{L}$. The coordinates x' and y' are fixed onto the
graphite, x and y are along the circumference and axis,
respectively, and η denotes a chiral angle. Another
choice of primitive translation vectors is $\boldsymbol{a}_1$ and $\boldsymbol{a}_2$.
(b) The first Brillouin zone of the 2D graphite. The
vertices of the hexagon are called K and K' points.
(c) The coordinate system (x,y) in the nanotube, an
Aharonov-Bohm magnetic flux ϕ, and a magnetic field
$\boldsymbol{B}$ perpendicular to the axis.

discussed.

In §7 effects of impurity scattering are discussed and
the total absence of backward scattering is predicted ex-
cept for scatterers with a potential range smaller than
the lattice constant. Further, the presence of a perfectly
conducting channel and its sensitivity to the presence of
various symmetry breaking effects such as inelastic scat-
tering, magnetic field and flux, short-range scatterers,
and trigonal warping are discussed. In §8 a continuum
model for phonons is introduced and effective Hamilto-
nian describing electron-phonon interaction is derived.
In §9 the conductance quantization in the presence of
lattice vacancies, i.e., strong and short-range scatterers,
is discussed. In §10 the transport across a junction of
nanotubes with different diameters through a pair of
topological defects such as five- and seven-member rings
is discussed. A short summary is given in §11.

§2. Two-Dimensional Graphite

2.1 Preliminaries

The structure of 2D graphite sheet and the first Bril-
louin zone are shown in Fig. 1. We have the primitive
translation vectors $\boldsymbol{a}=a(1,0)$ and $\boldsymbol{b}=a(-1/2,\sqrt{3}/2)$, and
the vectors connecting nearest neighbor carbon atoms
$\vec{\tau}_1 = a(0,1/\sqrt{3})$, $\vec{\tau}_2 = a(-1/2,-1/2\sqrt{3})$, and $\vec{\tau}_3 = a(1/2,-1/2\sqrt{3})$, where a is the lattice constant given
by $a=0.246$ nm. A hexagonal unit cell with area

$$\Omega_0 = \frac{\sqrt{3}}{2}a^2, \tag{2.1}$$

contains two carbon atoms, which will be denoted by A
and B in the following as shown in Fig. 1.

The primitive reciprocal lattice vectors $\boldsymbol{a}^*$ and $\boldsymbol{b}^*$
are given by $\boldsymbol{a}^* = (2\pi/a)(1,1/\sqrt{3})$ and $\boldsymbol{b}^* = (2\pi/a)(0,2/\sqrt{3})$, The hexagonal first Brillouin zone has the area

$$\Omega_0^* = \frac{2}{\sqrt{3}}\left(\frac{2\pi}{a}\right)^2. \tag{2.2}$$

The K and K' points at the corners of the Brillouin
zone are given as $\boldsymbol{K} = (2\pi/a)(1/3,1/\sqrt{3})$ and $\boldsymbol{K}' = (2\pi/a)(2/3,0)$, respectively. We have the relations
$\exp(\mathrm{i}\boldsymbol{K}\cdot\vec{\tau}_1) = \omega$, $\exp(\mathrm{i}\boldsymbol{K}\cdot\vec{\tau}_2) = \omega^{-1}$, $\exp(\mathrm{i}\boldsymbol{K}\cdot\vec{\tau}_3) = 1$,
$\exp(\mathrm{i}\boldsymbol{K}'\cdot\vec{\tau}_1)=1$, $\exp(\mathrm{i}\boldsymbol{K}'\cdot\vec{\tau}_2)=\omega^{-1}$, and $\exp(\mathrm{i}\boldsymbol{K}'\cdot\vec{\tau}_3)=\omega$,
with $\omega=\exp(2\pi\mathrm{i}/3)$.

In a graphite sheet, the conduction and valence
bands consisting of π states touch at the K and K' point.
For CN's with a large diameter, effects of the curvature
of the graphite sheet can safely be neglected and there-
fore electronic states in the vicinity of the Fermi level are
determined by the states near the K and K' points. In
the following we shall confine ourselves to global proper-
ties of nanotubes mainly and discuss effects arising from
finite curvature when necessary. First-principles calcu-
lations showed that electronic properties can be altered
for tubes with an extremely small diameter because of
a hybridization of π states with σ bands which lie well
above the Fermi level in 2D graphite.[38,39]

2.2 Nearest-Neighbor Tight-Binding Model

In a tight-binding model, the wave function is writ-
ten as

$$\psi(\boldsymbol{r}) = \sum_{\boldsymbol{R}_A}\psi_A(\boldsymbol{R}_A)\phi(\boldsymbol{r}-\boldsymbol{R}_A) + \sum_{\boldsymbol{R}_B}\psi_B(\boldsymbol{R}_B)\phi(\boldsymbol{r}-\boldsymbol{R}_B), \tag{2.3}$$

where $\phi(\boldsymbol{r})$ is the wave function of the p_z orbital of a
carbon atom located at the origin, $\boldsymbol{R}_A = n_a\boldsymbol{a}+n_b\boldsymbol{b}+\vec{\tau}_1$,
and $\boldsymbol{R}_B = n_a\boldsymbol{a}+n_b\boldsymbol{b}$ with integer n_a and n_b. Let $-\gamma_0$
be the transfer integral between nearest-neighbor carbon
atoms and choose the energy origin at that of the carbon
p_z level. Then, we have

$$\varepsilon\psi_A(\boldsymbol{R}_A) = -\gamma_0\sum_{l=1}^{3}\psi_B(\boldsymbol{R}_A-\vec{\tau}_l),$$

$$\varepsilon\psi_B(\boldsymbol{R}_B) = -\gamma_0\sum_{l=1}^{3}\psi_A(\boldsymbol{R}_B+\vec{\tau}_l), \tag{2.4}$$

where the overlap integral between nearest A and B sites
is completely neglected for simplicity.

Assuming $\psi_A(\boldsymbol{R}_A)\propto f_A(\boldsymbol{k})\exp(\mathrm{i}\boldsymbol{k}\cdot\boldsymbol{R}_A)$ and $\psi_B(\boldsymbol{R}_B)$
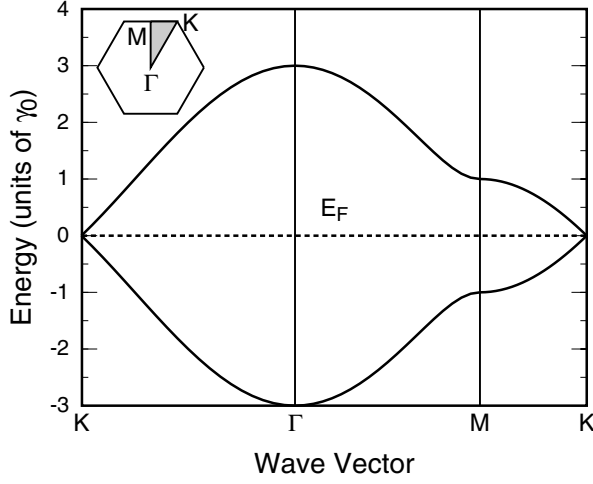
Fig. 2 The π band structure of a two-dimensional graphite obtained in a nearest-neighbor tight-binding model along K $\rightarrow$ Γ $\rightarrow$ M $\rightarrow$ K shown in the inset. The Fermi level lies at the center $\varepsilon = 0$.

$\propto f_B(\boldsymbol{k}) \exp(\mathrm{i}\boldsymbol{k}\cdot\boldsymbol{R}_B)$, we have

$$\begin{pmatrix} 0 & h_{AB}(\boldsymbol{k}) \\ h_{AB}(\boldsymbol{k})^* & 0 \end{pmatrix} \begin{pmatrix} f_A(\boldsymbol{k}) \\ f_B(\boldsymbol{k}) \end{pmatrix} = \varepsilon \begin{pmatrix} f_A(\boldsymbol{k}) \\ f_B(\boldsymbol{k}) \end{pmatrix}, \quad (2.5)$$

with

$$h_{AB}(\boldsymbol{k}) = -\gamma_0 \sum_l \exp(-\mathrm{i}\boldsymbol{k}\cdot\vec{\tau}_l). \quad (2.6)$$

The energy bands are given by

$$\varepsilon_\pm(\boldsymbol{k}) = \pm\gamma_0\sqrt{1 + 4\cos\frac{ak_x}{2}\cos\frac{\sqrt{3}ak_y}{2} + 4\cos^2\frac{ak_x}{2}}. \quad (2.7)$$

It is clear that $\varepsilon_\pm(\boldsymbol{K}) = \varepsilon_\pm(\boldsymbol{K}') = 0$. Near the K and K' points, we have $\varepsilon_\pm(\boldsymbol{k}+\boldsymbol{K}) = \varepsilon_\pm(\boldsymbol{k}+\boldsymbol{K}') = \pm\gamma\sqrt{k_x^2 + k_y^2}$ with

$$\gamma = \frac{\sqrt{3}a\gamma_0}{2}, \quad (2.8)$$

for $|\boldsymbol{k}|a \ll 1$. This linear dispersion in the vicinity of the K and K' points plays decisive roles in various electronic and transport properties of 2D graphite and nanotubes as will be clear in the following. The band structure is shown in Fig. 2.

2.3 Effective-Mass Description

In the following, we shall derive an effective-mass or $\boldsymbol{k}\cdot\boldsymbol{p}$ equation describing states in the vicinity of K and K' points based on the nearest-neighbor tight-binding model. It should be noted, however, the effective-mass scheme itself is much more general if band parameters are chosen appropriately because the form of the effective Hamiltonian is determined by symmetry of the system. We consider the coordinates (x, y) rotated around the origin by η as well as original (x', y') as shown in Fig. 1.

For states in the vicinity of the Fermi level $\varepsilon = 0$ of the 2D graphite, we assume that the total wavefunction is written as

$$\psi_A(\boldsymbol{R}_A) = \mathrm{e}^{\mathrm{i}\boldsymbol{K}\cdot\boldsymbol{R}_A} F_A^K(\boldsymbol{R}_A) + \mathrm{e}^{\mathrm{i}\eta}\mathrm{e}^{\mathrm{i}\boldsymbol{K}'\cdot\boldsymbol{R}_A} F_A^{K'}(\boldsymbol{R}_A),$$
$$\psi_B(\boldsymbol{R}_B) = -\omega\mathrm{e}^{\mathrm{i}\eta}\mathrm{e}^{\mathrm{i}\boldsymbol{K}\cdot\boldsymbol{R}_B} F_B^K(\boldsymbol{R}_B) + \mathrm{e}^{\mathrm{i}\boldsymbol{K}'\cdot\boldsymbol{R}_B} F_B^{K'}(\boldsymbol{R}_B), \quad (2.9)$$

in terms of the slowly-varying envelope functions F_A^K,

F_B^K, $F_A^{K'}$, and $F_B^{K'}$. This can be written as

$$\begin{aligned} \psi_A(\boldsymbol{R}_A) &= \boldsymbol{a}(\boldsymbol{R}_A)^\dagger \boldsymbol{F}_A(\boldsymbol{R}_A), \\ \psi_B(\boldsymbol{R}_B) &= \boldsymbol{b}(\boldsymbol{R}_B)^\dagger \boldsymbol{F}_B(\boldsymbol{R}_B), \end{aligned} \quad (2.10)$$

with two-component vectors,

$$\begin{aligned} \boldsymbol{a}(\boldsymbol{R}_A)^\dagger &= (\, \mathrm{e}^{\mathrm{i}\boldsymbol{K}\cdot\boldsymbol{R}_A} \quad \mathrm{e}^{\mathrm{i}\eta}\mathrm{e}^{\mathrm{i}\boldsymbol{K}'\cdot\boldsymbol{R}_A} \,), \\ \boldsymbol{b}(\boldsymbol{R}_B)^\dagger &= (\, -\omega\mathrm{e}^{\mathrm{i}\eta}\mathrm{e}^{\mathrm{i}\boldsymbol{K}\cdot\boldsymbol{R}_B} \quad \mathrm{e}^{\mathrm{i}\boldsymbol{K}'\cdot\boldsymbol{R}_B} \,), \end{aligned} \quad (2.11)$$

and

$$\boldsymbol{F}_A = \begin{pmatrix} F_A^K \\ F_A^{K'} \end{pmatrix}, \quad \boldsymbol{F}_B = \begin{pmatrix} F_B^K \\ F_B^{K'} \end{pmatrix}. \quad (2.12)$$

In order to obtain equations for $\boldsymbol{F}$, we first substitute eq. (2.10) into eq. (2.4). Multiply the first equation by $g(\boldsymbol{r}'-\boldsymbol{R}_A)\boldsymbol{a}(\boldsymbol{R}_A)$ and then sum it over $\boldsymbol{R}_A$, where $g(\boldsymbol{r})$ is a smoothing function which varies smoothly in the range $|r| \lesssim a$ and decays rapidly and vanishes for $|r| \gg a$. It should satisfy the conditions:

$$\sum_{\boldsymbol{R}_A} g(\boldsymbol{r}'-\boldsymbol{R}_A) = \sum_{\boldsymbol{R}_B} g(\boldsymbol{r}'-\boldsymbol{R}_B) = 1, \quad (2.13)$$

and

$$\int \mathrm{d}\boldsymbol{r}'\, g(\boldsymbol{r}'-\boldsymbol{R}_A) = \int \mathrm{d}\boldsymbol{r}'\, g(\boldsymbol{r}'-\boldsymbol{R}_B) = \Omega_0. \quad (2.14)$$

The function $g(\boldsymbol{r}'-\boldsymbol{R})$ can be replaced by a delta function when it is multiplied by a smooth function such as envelopes, i.e., $g(\boldsymbol{r}'-\boldsymbol{R}) \approx \Omega_0\delta(\boldsymbol{r}'-\boldsymbol{R})$. Then, the equation is rewritten as

$$\begin{aligned} \varepsilon &\sum_{\boldsymbol{R}_A} g(\boldsymbol{r}'-\boldsymbol{R}_A)\boldsymbol{a}(\boldsymbol{R}_A)\boldsymbol{a}(\boldsymbol{R}_A)^\dagger \boldsymbol{F}_A(\boldsymbol{r}') \\ &= -\gamma_0 \sum_l \sum_{\boldsymbol{R}_A} g(\boldsymbol{r}'-\boldsymbol{R}_A)\boldsymbol{a}(\boldsymbol{R}_A)\boldsymbol{b}(\boldsymbol{R}_A-\vec{\tau}_l)^\dagger \quad (2.15) \\ &\quad \times \left[\boldsymbol{F}_B(\boldsymbol{r}') - \left(\vec{\tau}_l\cdot\frac{\partial}{\partial\boldsymbol{r}'}\right)\boldsymbol{F}_B(\boldsymbol{r}') + \cdots \right], \end{aligned}$$

where $\boldsymbol{F}_A(\boldsymbol{R}_A)$ and $\boldsymbol{F}_B(\boldsymbol{R}_A - \vec{\tau}_l)$ have been replaced by $\boldsymbol{F}_A(\boldsymbol{r}')$ and $\boldsymbol{F}_B(\boldsymbol{r}' - \vec{\tau}_l)$, respectively, because it is multiplied by $g(\boldsymbol{r}'-\boldsymbol{R}_A)$. Noting that

$$\sum_{\boldsymbol{R}_A} g(\boldsymbol{r}'-\boldsymbol{R}_A)\boldsymbol{a}(\boldsymbol{R}_A)\boldsymbol{a}(\boldsymbol{R}_A)^\dagger \approx \begin{pmatrix} 1 & 0 \\ 0 & 1 \end{pmatrix}, \quad (2.16)$$

we immediately obtain the left hand side of eq. (2.15) as $\varepsilon\boldsymbol{F}_A(\boldsymbol{r})$. As for the right hand side, we should note first that

$$\begin{aligned} &\sum_{\boldsymbol{R}_A} g(\boldsymbol{r}'-\boldsymbol{R}_A)\boldsymbol{a}(\boldsymbol{R}_A)\boldsymbol{b}(\boldsymbol{R}_A-\vec{\tau}_l)^\dagger \\ &\approx \begin{pmatrix} -\omega\mathrm{e}^{\mathrm{i}\eta}\mathrm{e}^{-\mathrm{i}\boldsymbol{K}\cdot\vec{\tau}_l} & 0 \\ 0 & \mathrm{e}^{-\mathrm{i}\eta}\mathrm{e}^{-\mathrm{i}\boldsymbol{K}'\cdot\vec{\tau}_l} \end{pmatrix}. \end{aligned} \quad (2.17)$$

This immediately leads to the conclusion that the first term in the right hand side of eq. (2.15) vanishes identically. To calculate the second term we first note that

$$\begin{aligned} \sum_l \mathrm{e}^{-\mathrm{i}\boldsymbol{K}\cdot\vec{\tau}_l} (\, \tau_l^x \quad \tau_l^y \,) &= \frac{\sqrt{3}}{2}\omega^{-1}a(\, +\mathrm{i} \quad +1 \,), \\ \sum_l \mathrm{e}^{-\mathrm{i}\boldsymbol{K}'\cdot\vec{\tau}_l} (\, \tau_l^x \quad \tau_l^y \,) &= \frac{\sqrt{3}}{2}a(\, -\mathrm{i} \quad +1 \,), \end{aligned} \quad (2.18)$$

and the final result is

$$\varepsilon\boldsymbol{F}_A(\boldsymbol{r}) = \gamma \begin{pmatrix} \hat{k}_x - \mathrm{i}\hat{k}_y & 0 \\ 0 & \hat{k}_x + \mathrm{i}\hat{k}_y \end{pmatrix} \boldsymbol{F}_B(\boldsymbol{r}), \quad (2.19)$$
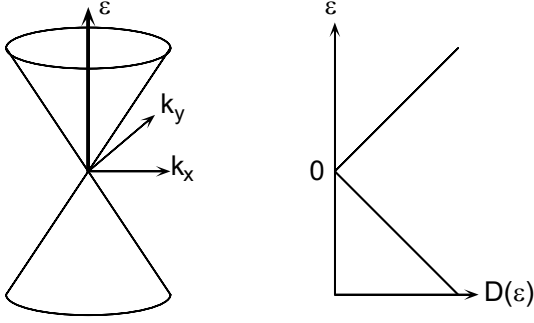
Fig. 3   The energy bands in the vicinity of the K and K' points and the density of states in 2D graphite.

where $\boldsymbol{r}'$ has been replaced by $\boldsymbol{r}$ and $\hat{\boldsymbol{k}}' \equiv -i\boldsymbol{\nabla}'$ by $\hat{\boldsymbol{k}} \equiv -i\boldsymbol{\nabla}$.

The equation for $\boldsymbol{F}_B(\boldsymbol{r})$ can be obtained in a similar manner and the full Schrödinger equation is given by

$$\mathcal{H}_0 \boldsymbol{F}(\boldsymbol{r}) = \varepsilon \boldsymbol{F}(\boldsymbol{r}), \qquad (2.20)$$

with

$$
\begin{array}{cccc}
KA & KB & K'A & K'B
\end{array}
$$
$$
\mathcal{H}_0 = \begin{pmatrix}
0 & \gamma(\hat{k}_x - i\hat{k}_y) & 0 & 0 \\
\gamma(\hat{k}_x + i\hat{k}_y) & 0 & 0 & 0 \\
0 & 0 & 0 & \gamma(\hat{k}_x + i\hat{k}_y) \\
0 & 0 & \gamma(\hat{k}_x - i\hat{k}_y) & 0
\end{pmatrix},
$$
$$(2.21)$$

where

$$\boldsymbol{F}^K(\boldsymbol{r}) = \begin{pmatrix} F_A^K(\boldsymbol{r}) \\ F_B^K(\boldsymbol{r}) \end{pmatrix}, \quad \boldsymbol{F}^{K'}(\boldsymbol{r}) = \begin{pmatrix} F_A^{K'}(\boldsymbol{r}) \\ F_B^{K'}(\boldsymbol{r}) \end{pmatrix}, \quad (2.22)$$

and

$$\boldsymbol{F}(\boldsymbol{r}) = \begin{pmatrix} \boldsymbol{F}^K(\boldsymbol{r}) \\ \boldsymbol{F}^{K'}(\boldsymbol{r}) \end{pmatrix}. \qquad (2.23)$$

This is rewritten as

$$
\begin{aligned}
\gamma(\hat{\boldsymbol{k}} \cdot \vec{\sigma}) \boldsymbol{F}^K(\boldsymbol{r}) &= \varepsilon \boldsymbol{F}^K(\boldsymbol{r}), \\
\gamma(\hat{\boldsymbol{k}}' \cdot \vec{\sigma}) \boldsymbol{F}^{K'}(\boldsymbol{r}) &= \varepsilon \boldsymbol{F}^{K'}(\boldsymbol{r}),
\end{aligned}
\qquad (2.24)
$$

with $\boldsymbol{\sigma} = (\sigma_x, \sigma_y)$ being the Pauli spin matrices, $\hat{k}_x' = \hat{k}_x$, and $\hat{k}_y' = -\hat{k}_y$. These are relativistic Dirac equation with vanishing rest mass known as Weyl's equation for a neutrino.

Note again that the above Schrödinger equation for the envelope function has been derived based on the nearest-neighbor tight-binding model, but is actually quite general and valid for more general band structure of 2D graphite. The energy bands are given by

$$\varepsilon_s(k) = s\gamma|k|, \qquad (2.25)$$

where $s = +1$ and -1 denote conduction and valence bands, respectively. The corresponding density of states becomes

$$D(\varepsilon) = \frac{1}{S} \sum_{s,\boldsymbol{k}} \delta[\varepsilon - \varepsilon_s(k)] = \frac{|\varepsilon|}{2\pi\gamma^2}. \qquad (2.26)$$

Figure 3 gives a schematic illustration of the conic dispersion and the corresponding density of states. The density of states varies linearly as a function of the energy and vanishes at $\varepsilon = 0$.

2.4 Topological Singularity and Berry's Phase

The eigen wave functions and energies of the Hamiltonian for the K point are written in the absence of a magnetic field as

$$\boldsymbol{F}_{s\boldsymbol{k}}(\boldsymbol{r}) = \frac{1}{\sqrt{LA}} \exp(i\boldsymbol{k}\cdot\boldsymbol{r})\, \boldsymbol{F}_{s\boldsymbol{k}}. \qquad (2.27)$$

In general, we can write eigenvector $\boldsymbol{F}_{s\boldsymbol{k}}$ as

$$\boldsymbol{F}_{s\boldsymbol{k}} = \exp[i\phi_s(\boldsymbol{k})]\, R^{-1}[\theta(\boldsymbol{k})] |s\rangle, \qquad (2.28)$$

where $\phi_s(\boldsymbol{k})$ is an arbitrary phase factor, $\theta(\boldsymbol{k})$ is the angle between wave vector $\boldsymbol{k}$ and the k_y axis, i.e., $k_x + ik_y = +i|\boldsymbol{k}|e^{i\theta(\boldsymbol{k})}$ and $k_x - ik_y = -i|\boldsymbol{k}|e^{-i\theta(\boldsymbol{k})}$, $R(\theta)$ is a spin-rotation operator, given by

$$R(\theta) = \exp\left(i\frac{\theta}{2}\sigma_z\right) = \begin{pmatrix} \exp(+i\theta/2) & 0 \\ 0 & \exp(-i\theta/2) \end{pmatrix}, \qquad (2.29)$$

with σ_z being a Pauli matrix, and $|s\rangle$ is the eigenvector for the state with $\boldsymbol{k}$ in the positive k_y direction, given by

$$|s\rangle = \frac{1}{\sqrt{2}} \begin{pmatrix} -is \\ 1 \end{pmatrix}. \qquad (2.30)$$

Obviously, we have

$$
\begin{aligned}
R(\theta_1)R(\theta_2) &= R(\theta_1 + \theta_2), \\
R(-\theta) &= R^{-1}(\theta).
\end{aligned}
\qquad (2.31)
$$

Further, because $R(\theta)$ describes the rotation of a spin, it has the property

$$R(\theta \pm 2\pi) = -R(\theta), \qquad (2.32)$$

which gives $R(-\pi) = -R(+\pi)$. The appearance of the spin rotation operator and the corresponding signature change under the 2π rotation around $\boldsymbol{k} = 0$ correspond to a topological singularity at $\boldsymbol{k} = 0$.

The presence of the singularity can be understood more clearly in terms of Berry's phase.[40,41] Consider the case that the Hamiltonian contains a parameter s. Let the parameter s change from $s(0)$ to $s(T)$ as a function of time t from $t = 0$ to $t = T$ and assume that $\mathcal{H}[s(T)] = \mathcal{H}[s(0)]$. Note that $s(T)$ is not necessarily same as $s(0)$. When there is no degeneracy, the state at $t = T$ is completely same as that at $t = 0$ when the process is sufficiently slow and adiabatic. Therefore, the wave function at $t = T$ is equal to that at $t = 0$ except for the presence of a phase factor $\exp(-i\varphi)$. This extra phase called Berry's phase is given by

$$\varphi = -i \int_0^T dt \left\langle \psi[s(t)] \Big| \frac{d\psi[s(t)]}{dt} \right\rangle. \qquad (2.33)$$

Consider a wave function given by

$$\psi_s(\boldsymbol{k}) = \frac{1}{\sqrt{2}} \begin{pmatrix} -is\exp[-i\theta(\boldsymbol{k})] \\ 1 \end{pmatrix}. \qquad (2.34)$$

This is the "spin" part of an eigenfunction, obtained by choosing $\phi_s(\boldsymbol{k}) = -\theta(\boldsymbol{k})/2$ in such a way that the wave function becomes continuous as a function of $\theta(\boldsymbol{k})$. When the wave vector $\boldsymbol{k}$ is rotated in the anticlockwise direction adiabatically as a function of time t around the origin for a time interval $0 < t < T$, the wavefunction is changed into $\psi_s(\boldsymbol{k}) \exp(-i\varphi)$, where φ is Berry's phase given by

$$\varphi = -i \int_0^T dt \left\langle \psi_s[\boldsymbol{k}(t)] \Big| \frac{d}{dt} \psi_s[\boldsymbol{k}(t)] \right\rangle = -\pi. \qquad (2.35)$$

This shows that the rotation in the $\boldsymbol{k}$ space by 2π leads to

the change in the phase by $-\pi$, i.e., a signature change. Note that $R^{-1}[\theta(\boldsymbol{k})]|s)$ is obtained from eq. (2.34) by continuously varying the direction of $\boldsymbol{k}$ including Berry's phase. Note also that the signature change occurs only when the closed contour encircles the origin $\boldsymbol{k} = 0$ but not when the contour does not contain $\boldsymbol{k} = 0$, showing the prepense of a singularity at $\boldsymbol{k} = 0$.

This topological singularity at $\boldsymbol{k} = 0$ causes various zero-mode anomalies.[42,43] For example, the conductivity calculated with the use of the Boltzmann transport equation is independent of the Fermi energy and the 2D graphite shows a metallic behavior if being extrapolated to $\varepsilon = 0$. Therefore, the 2D graphite is not a zero-gap semiconductor as commonly believed. A more refined treatment in a self-consistent Born approximation gives the result that the conductivity at $\varepsilon = 0$ is given by a universal value $e^2/\pi\hbar$ and rapidly approaches the Boltzmann result with the deviation from $\varepsilon = 0$.[42] This quantum conductivity at $\varepsilon = 0$ is a typical example of anomalies. This subject will not be discussed further including similar anomalies in the magneto-conductivity and the dynamical conductivity.[43,44]

2.5 Magnetic Field

In a magnetic field B perpendicular to the 2D graphite sheet, we have to replace $\hat{\boldsymbol{k}} = -\mathrm{i}\vec{\nabla}$ by $\hat{\boldsymbol{k}} = -\mathrm{i}\vec{\nabla} + (e/c\hbar)\boldsymbol{A}$ with $\boldsymbol{A}$ being a vector potential giving the field $B = (\partial A_y/\partial x) - (\partial A_x/\partial y)$. Then, we have $[\hat{k}_x, \hat{k}_y] = -\mathrm{i}l^{-2}$ where l is the magnetic length given by

$$l = \sqrt{\frac{c\hbar}{eB}}. \qquad (2.36)$$

Define $a = (l/\sqrt{2})(\hat{k}_x - \mathrm{i}\hat{k}_y)$ and $a^\dagger = (l/\sqrt{2})(\hat{k}_x + \mathrm{i}\hat{k}_y)$. Then, we have $[a, a^\dagger] = 1$. In terms of these operators the Hamiltonian for the K point is rewritten as

$$\mathcal{H}_0 = \frac{\sqrt{2}\gamma}{l} \begin{pmatrix} 0 & a \\ a^\dagger & 0 \end{pmatrix}. \qquad (2.37)$$

We shall define a function $h_n(x, y)$ such that

$$h_n(x, y) = \frac{(a^\dagger)^n}{\sqrt{n!}} h_0(x, y), \qquad (2.38)$$

with

$$a\, h_0(x, y) = 0. \qquad (2.39)$$

Then, we have

$$\begin{aligned} a^\dagger\, h_n &= \sqrt{n+1}\, h_{n+1}, \\ a\, h_{n+1} &= \sqrt{n+1}\, h_{n+1}, \\ a^\dagger a\, h_n &= n\, h_n. \end{aligned} \qquad (2.40)$$

Therefore, there is a Landau level with vanishing energy $\varepsilon_0 = 0$ with the wave function

$$\boldsymbol{F}_0^K = \begin{pmatrix} 0 \\ h_0 \end{pmatrix}. \qquad (2.41)$$

Other Landau levels are at

$$\varepsilon_n = \mathrm{sgn}(n) \frac{\sqrt{2}\gamma}{l} \sqrt{|n|}, \qquad (2.42)$$

with wave function

$$\boldsymbol{F}_n^K = \frac{1}{\sqrt{2}} \begin{pmatrix} \mathrm{sgn}(n) h_{|n|-1} \\ h_{|n|} \end{pmatrix}, \qquad (2.43)$$

where $n = \pm 1, \pm 2, \ldots$ and $\mathrm{sgn}(t)$ denotes the signature of t, i.e., $\mathrm{sgn}(t) = +1$ for $t > 0$ and -1 for $t < 0$. Similar expressions can be derived for the K' point. The presence of the Landau level at $\varepsilon = 0$ independent of the magnetic-field strength is a remarkable feature of the Weyl equation, leading to a divergent magnetic susceptibility as discussed in §4.

§3. Nanotubes

3.1 Chiral Vector and Unit Cell

Every structure of single tube CN's can be constructed from a monatomic layer of graphite as shown in Fig. 1 (a). Each lattice-translation vector is specified by a set of two integers $[n_a, n_b]$ such that

$$\boldsymbol{L} = n_a\boldsymbol{a} + n_b\boldsymbol{b} = \left(n_a - \frac{1}{2}n_b, \frac{\sqrt{3}}{2}n_b\right). \qquad (3.1)$$

A nanotube can be constructed in such a way that the hexagon at $\boldsymbol{L}$ is rolled onto the hexagon at the origin. This $\boldsymbol{L}$ is called the chiral vector and becomes a circumference of CN. The direction angle η of $\boldsymbol{L}$ is called the chiral angle. We have

$$L = |\boldsymbol{L}| = a\sqrt{n_a^2 + n_b^2 - n_a n_b}, \qquad (3.2)$$

where use has been made of $\boldsymbol{a} \cdot \boldsymbol{b} = -a^2/2$. In the following, the origin $x = 0$ is chosen usually at a point corresponding to the top side when the sheet is rolled and the point $x = L/2$ at point corresponding to the bottom side as is shown in Fig. 1 (c).

In another convention for the choice of primitive translation vectors, $\boldsymbol{a}_1 = \boldsymbol{a}$ and $\boldsymbol{a}_2 = \boldsymbol{a} + \boldsymbol{b}$, $\boldsymbol{L}$ is characterized by two integers (n_1, n_2) such that $\boldsymbol{L} = n_1\boldsymbol{a}_1 + n_2\boldsymbol{a}_2$, and the corresponding CN is sometimes called a (n_1, n_2) nanotube They are related to n_a and n_b through $n_1 = n_a - n_b$ and $n_2 = n_b$, i.e., $(n_1, n_2) = (n_a - n_b, n_b)$.

A primitive translation vector in the axis y direction is written as

$$\boldsymbol{T} = m_a\boldsymbol{a} + m_b\boldsymbol{b}, \qquad (3.3)$$

with integer m_a and m_b. Now, $\boldsymbol{T}$ is determined by the condition $\boldsymbol{T} \cdot \boldsymbol{L} = 0$, which can be written as

$$m_a(2n_a - n_b) - m_b(n_a - 2n_b) = 0. \qquad (3.4)$$

This can be solved as

$$p m_a = n_a - 2n_b, \quad p m_b = 2n_a - n_b, \qquad (3.5)$$

where p is the greatest common divisor of $n_a - 2n_b$ and $2n_a - n_b$. The first Brillouin zone of the nanotube is given by the region $-\pi/T \le k_y < \pi/T$ with

$$T = |\boldsymbol{T}| = a\sqrt{m_a^2 + m_b^2 - m_a m_b}. \qquad (3.6)$$

The unit cell is formed by the rectangular region determined by $\boldsymbol{L}$ and $\boldsymbol{T}$. The number of atoms in the unit cell becomes

$$2\frac{|\boldsymbol{L} \times \boldsymbol{T}|}{\Omega_0} = 2|n_a m_b - n_b m_a|. \qquad (3.7)$$

3.2 Band Structure

For nanotubes with a sufficiently large diameter, the energy bands are obtained simply by imposing periodic
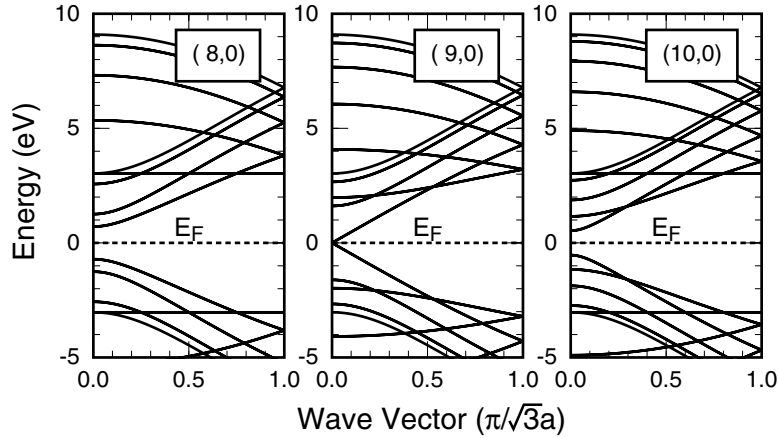
Fig. 4 Some examples of the band structure obtained in a tight-binding model for zigzag nanotubes. $[n_a, n_b] = [m, 0]$ or $(n_1, n_2) = (m, 0)$ with $m = 8, 9, 10$.

Type	n_a	n_b	ν	m_a	m_b	T	μ	k_0
Zigzag	m	0	0	1	2	$\sqrt{3}a$	0	0
	m	0	± 1	1	2	$\sqrt{3}a$		
Armchair	$2m$	m	0	0	1	a	1	$\pm 2\pi/3a$

Table I   Parameters for zigzag and armchair nanotubes.

boundary conditions along the circumference direction, i.e., $\psi(\boldsymbol{r} + \boldsymbol{L}) = \psi(\boldsymbol{r})$. This leads to the condition

$$\exp(\mathrm{i}\boldsymbol{k} \cdot \boldsymbol{L}) = 1. \tag{3.8}$$

It makes the wave vector along the circumference direction discrete, i.e., $k_x = 2\pi j / L$ with integer j, but the wave vector perpendicular to $\boldsymbol{L}$ remains continuous. The one-dimensional (1D) energy bands are given by these straight lines in the $\boldsymbol{k}$ space.

The actual value $\tilde{k}_y$ within the 1D first Brillouin zone $-T/\pi \leq \tilde{k}_y < T/\pi$ can be obtained by

$$\exp(\mathrm{i}\boldsymbol{k} \cdot \boldsymbol{T}) = \exp(\mathrm{i}\tilde{k}_y T). \tag{3.9}$$

In order to avoid multiple counting of states we have to consider $\boldsymbol{k}$ which is independent of each other. This can be achieved by imposing the condition that two wave vectors $\boldsymbol{k}_1$ and $\boldsymbol{k}_2$ should not be related to each other by any reciprocal lattice vector. The number of 1D bands in the 1D first Brillouin zone is given by the total number of carbon atoms in a unit cell determined by $\boldsymbol{L}$ and $\boldsymbol{T}$.

The band structure of a nanotube depends critically on whether the K and K' points in the Brillouin zone of the 2D graphite are included in the allowed wave vectors when the 2D graphite is rolled into a nanotube. This can be understood by considering $\exp(\mathrm{i}\boldsymbol{K} \cdot \boldsymbol{L})$ and $\exp(\mathrm{i}\boldsymbol{K}' \cdot \boldsymbol{L})$. We have

$$\exp(\mathrm{i}\boldsymbol{K} \cdot \boldsymbol{L}) = \exp\left[+\frac{2\pi\mathrm{i}}{3}(n_a + n_b)\right] = \exp\left(+\mathrm{i}\frac{2\pi\nu}{3}\right),$$
$$\exp(\mathrm{i}\boldsymbol{K}' \cdot \boldsymbol{L}) = \exp\left[-\frac{2\pi\mathrm{i}}{3}(n_a + n_b)\right] = \exp\left(-\mathrm{i}\frac{2\pi\nu}{3}\right), \tag{3.10}$$

where ν is an integer $(0, \pm 1)$ determined by

$$n_a + n_b = 3N + \nu, \tag{3.11}$$

with integer N. This shows that for $\nu = 0$ the nanotube becomes metallic because two bands cross at the wave
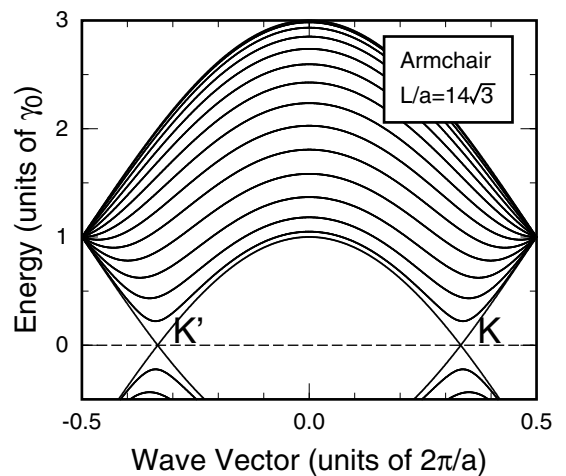

Fig. 5   An example of the band structure of an armchair nanotube. $[n_a, n_b] = [2m, m]$ or $(n_1, n_2) = (m, m)$ with $m = 14$.

vector corresponding to K and K' points without a gap. When $\nu = \pm 1$, on the other hand, there is a nonzero gap between valence and conduction bands and the nanotube is semiconducting. For another choice of the primitive translation vectors $\boldsymbol{a}_1$ and $\boldsymbol{a}_2$ or $\boldsymbol{L} = n_1 \boldsymbol{a}_1 + n_2 \boldsymbol{a}_2$, the integer ν is determined by the condition

$$n_1 - n_2 = 3N' + \nu, \tag{3.12}$$

with $N' = N - 3n_b$.

For translation $\boldsymbol{r} \to \boldsymbol{r} + \boldsymbol{T}$ the Bloch function at the K and K' points acquires the phase

$$\exp(\mathrm{i}\boldsymbol{K} \cdot \boldsymbol{T}) = \exp\left(+\mathrm{i}\frac{2\pi\mu}{3}\right),$$
$$\exp(\mathrm{i}\boldsymbol{K}' \cdot \boldsymbol{T}) = \exp\left(-\mathrm{i}\frac{2\pi\mu}{3}\right), \tag{3.13}$$

where $\mu = 0$ or ± 1 is determined by

$$m_a + m_b = 3M + \mu, \tag{3.14}$$

with integer M. The K and K' points are mapped onto $k_0 = +2\pi\mu/3T$ and $k_0' = -2\pi\mu/3T$, respectively, in the 1D Brillouin zone of the nanotube. When $\nu = 0$, therefore, two 1D bands cross each other without a gap at these points.

A nanotube has a helical or chiral structure for

general L. There are two kinds of non-chiral nanotubes, zigzag tube with $[n_a, n_b] = [m, 0]$ and armchair tube with $[n_a, n_b] = [2m, m]$. A zigzag nanotube is metallic when m is divided by three and semiconducting otherwise. We have $pm_a = n_a - 2n_b = m$ and $pm_b = 2n_a - n_b = 2m$, which give $[m_a, m_b] = [1, 2]$, $\mu = 0$. and $T = \sqrt{3}a$. When a zigzag nanotube is metallic, two conduction and valence bands having a linear dispersion cross at the Γ point of the 1D Brillouin zone.

On the other hand, an armchair nanotube is always metallic because $\nu = 0$. Further, we have $pm_a = n_a - 2n_b = 0$ and $pm_b = 2n_a - n_b = 3m$, which gives $[m_a, m_b] = [0, 1]$, $\mu = 1$, and $T = a$. Thus, the conduction and valence bands cross each other always at $k_0 = \pm 2\pi/3a$. These parameters are summarized in Table I. Figures 4 and 5 show some examples of the band structure obtained in the nearest-neighbor tight-binding model for zigzag and armchair nanotubes.

In order to discuss more general nanotubes, we shall introduce $L_0 = n_{a0}a + n_{b0}b$, with $L = rL_0$ or

$$n_a = r\, n_{a0}, \quad n_b = r\, n_{b0}, \qquad (3.15)$$

where r is the greatest common devisor of n_a and n_b. Introduce further a reciprocal lattice vector G_0 perpendicular to L or L_0 and parallel to T with the smallest length,

$$G_0 = n_{a0}^* a^* + n_{b0}^* b^*. \qquad (3.16)$$

The condition $G_0 \cdot L_0 = 0$ gives immediately

$$n_{a0}^* = -n_{b0}, \quad n_{b0}^* = n_{a0}. \qquad (3.17)$$

Define $k_0 \equiv k_0 L_0/|L_0|$ with $k_0 G_0 = \Omega_0^*$. Then, all k points in the rectangle given by k_0 and G_0 are independent and all other k points outside the rectangle can be

folded back to points in the rectangle by an appropriate reciprocal vector.

Therefore, the 1D energy bands are given by straight lines parallel to G_0 inside the rectangle. The distance between adjacent lines is given by

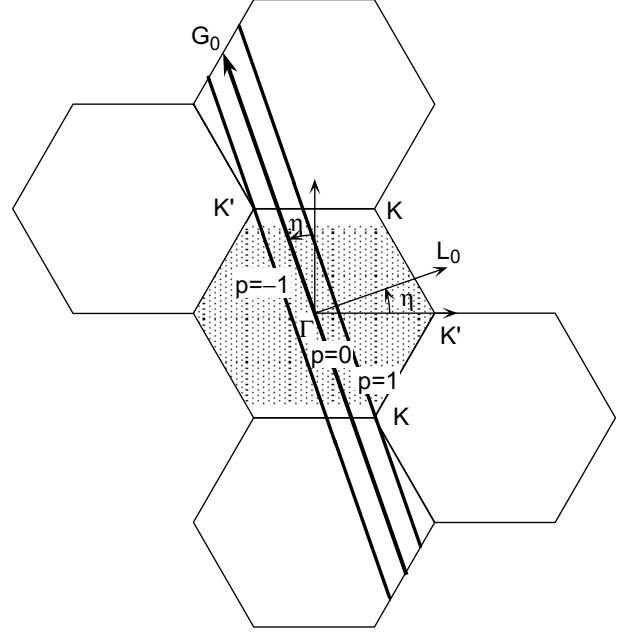$$\Delta k = \frac{2\pi}{r|L_0|} = \frac{2\pi}{ra\sqrt{n_{a0}^2 - n_{a0}n_{b0} + n_{b0}^2}}. \qquad (3.18)$$

Fig. 6   An example of the wave vectors giving the bands in a metallic nanotube with chiral vector $L = 3(3a+b)$. The bands are given by thick solid lines with $p = 0$, 1, and -1.
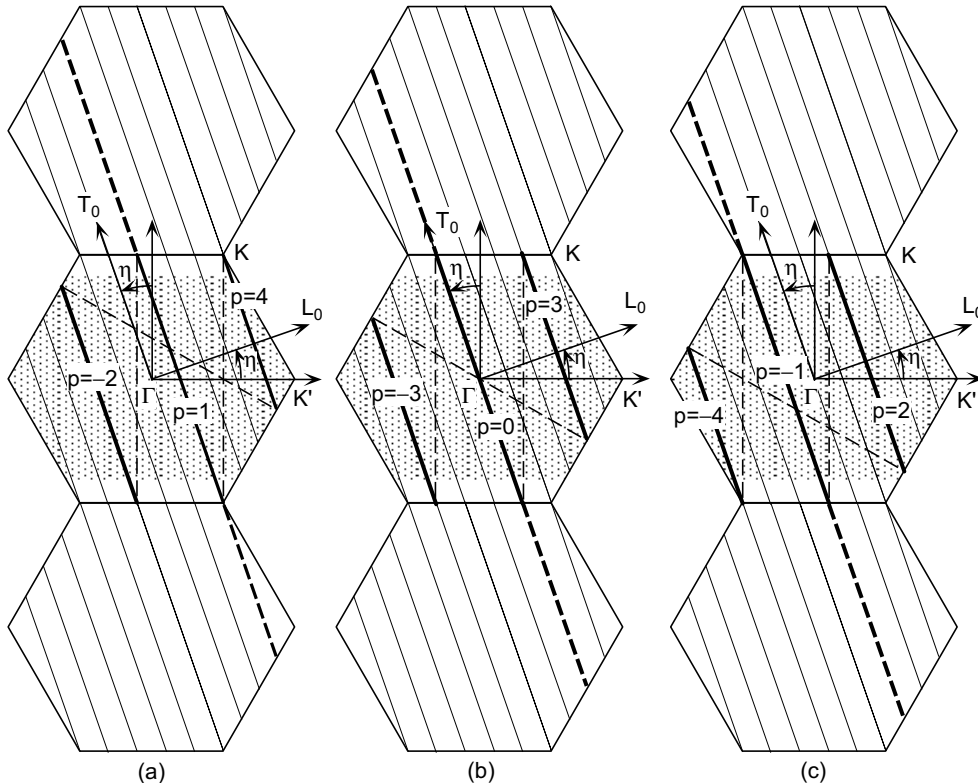

Fig. 7   A schematic illustration of three lines folded into those in the first Brillouin zone in a metallic nanotube with chiral vector $L = 3(3a+b)$.
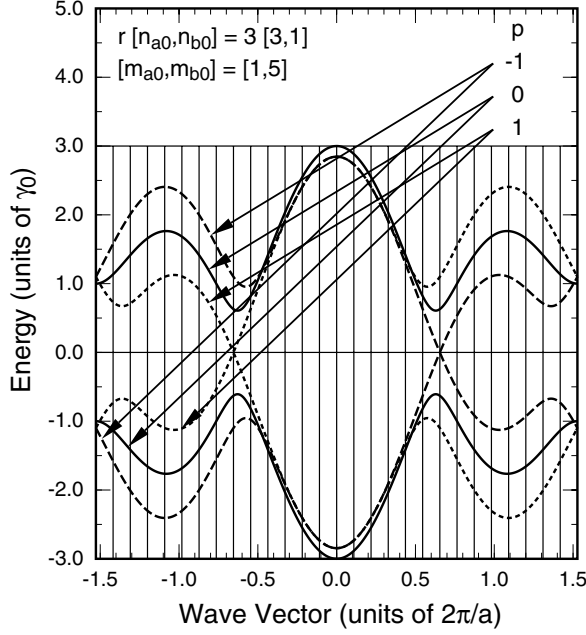
Fig. 8 An example of the band structure in a metallic nanotube with chiral vector $L = 3(3a + b)$. The thin vertical lines show the boundaries of the 1D Brillouin zone.

On the other hand, we have

$$k_0 = \frac{\Omega_0^*}{|G_0|} = \frac{2\pi}{a\sqrt{n_{a0}^2 - n_{a0}n_{b0} + n_{b0}^2}}. \quad (3.19)$$

Therefore, we have r independent straight lines in the rectangle. Thus, the energy bands are given by the wave vector

$$\boldsymbol{k} = p\Delta k\frac{\boldsymbol{L}_0}{|\boldsymbol{L}_0|} + t\frac{\boldsymbol{G}_0}{|\boldsymbol{G}_0|}, \quad (3.20)$$

with $p = 1, 2, \ldots, r$ and $-|\boldsymbol{G}_0|/2 \leq k < |\boldsymbol{G}_0|/2$. A straightforward calculation gives $|G_0|(2\pi/T)^{-1} = |n_{a0}m_b - n_{b0}m_a|$, showing that the number of valence bands associated with each line specified by integer p is the same as the number of atoms in the rectangle given by $\boldsymbol{L}_0$ and $\boldsymbol{T}$ as is expected.

For example, we consider the case $[n_a, n_b] = [9, 3]$ corresponding to a metallic nanotube. We have $[n_{a0}, n_{b0}] = [3, 1]$, giving $[m_a, m_b] = [1, 5]$ and $[n_{a0}^*, n_{b0}^*] = [-1, 3]$. The bands are given by straight lines with length G_0 specified by $p = 0, 1, 2$ or $p = 0, \pm 1$. This is illustrated in Fig. 6. Three straight lines can be folded into the

first Brillouin zone of the 2D graphite as illustrated in Fig. 7. Each line gives $|n_{a0}m_{b0} - n_{b0}m_{a0}| = 14$ valence bands and therefore in total $3 \times 14 = 42$ valence bands. The bands $p = +1$ and -1 ($p = 2$) are identical and degenerate for the wave vector in the first Brillouin zone of the nanotube because of the symmetry of the band of the two-dimensional graphite under inversion $\boldsymbol{k} \rightarrow -\boldsymbol{k}$. Figure 8 shows the resulting band structure obtained from the band structure of the 2D graphite calculated in a nearest-neighbor tight-binding model.

3.3 Effective-Mass Description

To derive the boundary conditions for the envelope function we can again start with eq. (2.10). The boundary conditions are given by $\psi_A(\boldsymbol{R}_A + \boldsymbol{L}) = \psi_A(\boldsymbol{R}_A)$ and $\psi_B(\boldsymbol{R}_B + \boldsymbol{L}) = \psi_B(\boldsymbol{R}_B)$. The substitution of eq. (2.10), the multiplication by $g(\boldsymbol{r} - \boldsymbol{R}_A)\boldsymbol{a}(\boldsymbol{R}_A)$ or $g(\boldsymbol{r} - \boldsymbol{R}_B)\boldsymbol{a}(\boldsymbol{R}_B)$, and finally the summation of them over $\boldsymbol{R}_A$ or $\boldsymbol{R}_B$ give immediately

$$\boldsymbol{F}^K(\boldsymbol{r} + \boldsymbol{L}) = e^{-i\boldsymbol{K}\cdot\boldsymbol{L}}\boldsymbol{F}^K(\boldsymbol{r}) = \exp\left(-\frac{2\pi i\nu}{3}\right)\boldsymbol{F}^K(\boldsymbol{r}),$$
$$\boldsymbol{F}^{K'}(\boldsymbol{r} + \boldsymbol{L}) = e^{-i\boldsymbol{K'}\cdot\boldsymbol{L}}\boldsymbol{F}^K(\boldsymbol{r}) = \exp\left(+\frac{2\pi i\nu}{3}\right)\boldsymbol{F}^{K'}(\boldsymbol{r}). \quad (3.21)$$

This means simply that the extra phases appearing in the boundary conditions for $\boldsymbol{F}^K$ and $\boldsymbol{F}^{K'}$ just cancel those of the Bloch functions at the K and K' points. Further, they correspond to the presence of a fictitious magnetic flux $\phi = -(\nu/3)\phi_0$ for the K point and $\phi = +(\nu/3)\phi_0$ for the K' point, where ϕ_0 is the magnetic flux given by

$$\phi_0 = \frac{ch}{e}. \quad (3.22)$$

The wave function on the cylinder surface is given by a plane wave $\boldsymbol{F}^K(\boldsymbol{r}) \propto \exp(ik_x x + ik_y y)$. Energy levels in CN for the K point are obtained by putting $k_x = \kappa_\nu(n)$ with

$$\kappa_\nu(n) = \frac{2\pi}{L}\left(n - \frac{\nu}{3}\right), \quad (3.23)$$

and $k_y = k$ in the above $\boldsymbol{k}\cdot\boldsymbol{p}$ equation as[12]

$$\varepsilon_{snk} = s\,\varepsilon(n, k), \quad (3.24)$$

with

$$\varepsilon(n, k) = \gamma\sqrt{\kappa_\nu(n)^2 + k^2}, \quad (3.25)$$

where $L = |\boldsymbol{L}|$, n is an integer, and $s = +1$ and -1 represent the conduction and valence bands, respectively.
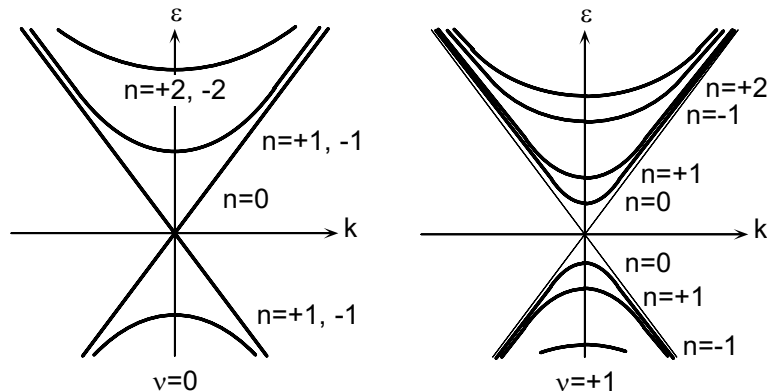

Fig. 9 Schematic illustration of energy bands obtained in the $\boldsymbol{k}\cdot\boldsymbol{p}$ scheme for $\nu = 0$ (left) and $\nu = +1$ (right).

The corresponding wave functions are written as

$$\boldsymbol{F}^K_{snk}(\boldsymbol{r}) = \frac{1}{\sqrt{AL}} \boldsymbol{F}^K_{snk} \exp\left[i\kappa_\nu(n)x + iky\right], \qquad (3.26)$$

with

$$\boldsymbol{F}^K_{snk} = \frac{1}{\sqrt{2}} \begin{pmatrix} sb_\nu(n,k) \\ 1 \end{pmatrix}, \qquad (3.27)$$

and

$$b_\nu(n,k) = \frac{\kappa_\nu(n) - ik}{\sqrt{\kappa_\nu(n) + k^2}}, \qquad (3.28)$$

where A is the length of the nanotube. Figure 9 shows the band structure in the vicinity of the K point for $\nu = 0$ and $+1$.

The wave equation for the K' point is obtained by replacing $\hat{k}_y$ by $-\hat{k}_y$ and also ν by $-\nu$ in the boundary conditions. Correspondingly, we have $\kappa'_\nu(n) = \kappa_{-\nu}(n)$ and $b'_\nu(n,k) = b_{-\nu}(n,k)^*$. The density of states associated with metallic linear bands is given by

$$D(\varepsilon) = \frac{4}{A} \sum_{s,k} \delta(\varepsilon - s\gamma|k|) = \frac{4}{\pi\gamma}, \qquad (3.29)$$

where the factor four comes from the electron spin and the presence of K and K' point. This is quite in contrast to the graphite sheet for which the density of states vanishes at $\varepsilon = 0$ even if the band gap vanishes. Each energy band of metallic CN's is two-fold degenerate except those for $n = 0$. For $\nu = \pm 1$, on the other hand, CN's become semiconducting with gap $\varepsilon_G = 4\pi\gamma/3L$ for the bands with $n = 0$.

3.4 Aharonov-Bohm Effect

When a magnetic field is applied parallel to the axis, i.e., in the presence of a magnetic flux ϕ passing through the cross section, the flux leads to the change in the boundary condition $\psi(\boldsymbol{r} + \boldsymbol{L}) = \psi(\boldsymbol{r})\exp(+2\pi i\varphi)$ with

$$\varphi = \frac{\phi}{\phi_0}. \qquad (3.30)$$

Consequently, $\kappa_\nu(n)$ is replaced by $\kappa_{\nu\varphi}(n)$ with

$$\kappa_{\nu\varphi}(n) = \frac{2\pi}{L}\left(n + \varphi - \frac{\nu}{3}\right), \qquad (3.31)$$

and $b_\nu(n,k)$ by $b_{\nu\varphi}(n,k)$. The corresponding result for the K' point is again obtained by the replacement $\nu \to -\nu$ and $k \to -k$. The gap gives an oscillation between 0 and $2\pi\gamma/L$ with period ϕ_0 as shown in Fig. 10.[12] This giant Aharonov-Bohm (AB) effect on the band gap is a unique property of CN's. The AB effect on the gap should appear in a tunneling conductance across a finite-length CN.[45]

As will be discussed in more details in §5, the interband optical absorption corresponding to the states in the vicinity of the K and K' points can be observed only for the light polarization parallel to the CN axis. Further, for the parallel polarization transitions are allowed only between bands with same n. The corresponding band gap is given by $\varepsilon^K_G(n) = 2\gamma|\kappa_{\nu\varphi}(n)|$ for the K point and by $\varepsilon^{K'}_G(n) = 2\gamma|\kappa'_{\nu\varphi}(n)|$ for the K' point, respectively.

Consider a semiconducting nanotube with $\nu = 1$, for example. Figure 11 shows band edges as a function of the flux. For a small magnetic flux $\varphi \ll 1$, the lowest
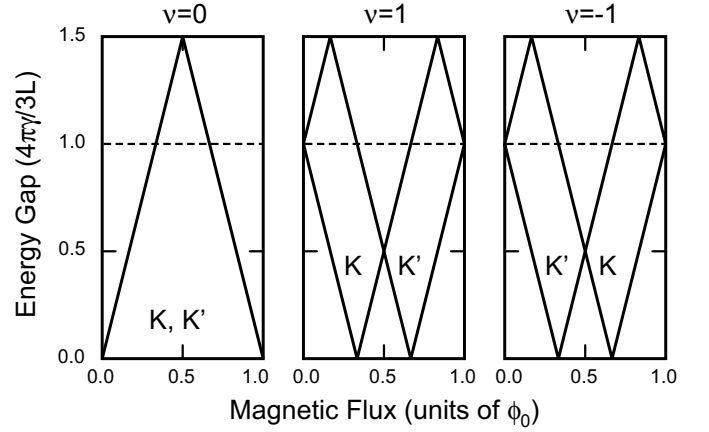

Fig. 10   Aharonov-Bohm effect on the band gap. In the case of a semiconducting nanotube with $\nu = +1$, the gap at the K point decreases and that at the K' point increases first in the presence of a small flux. The behavior is opposite for $\nu = -1$.
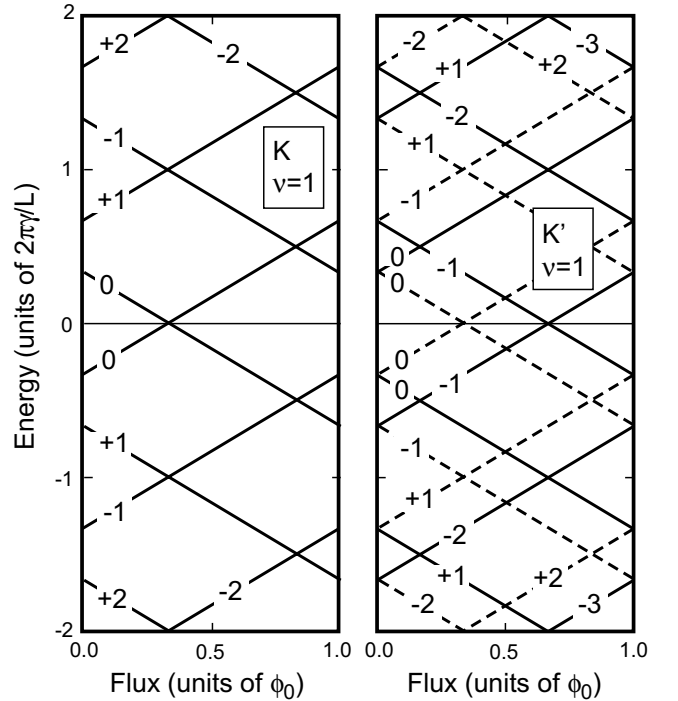

Fig. 11   The band edges as a function of the magnetic flux (solid lines) and of the effective flux associated with strain (dashed lines) in a semiconducting nanotube with $\nu = 1$. For the K point the dependence is exactly the same between the magnetic flux and the strain flux, while for the K' point the dependence is opposite. The result for a semiconducting tube with $\nu = -1$ can be obtained by the exchange between K and K'.

conduction band and the highest valence band are given by $n = 0$ for both K and K' points. At the K point, $\kappa_{\nu\varphi}(0) = -(2\pi/L)[(1/3) - \varphi]$ and the corresponding band gap is given by $\varepsilon^K_{G\varphi}(0) = (2/3)(2\pi\gamma/L)(1 - 3\varphi)$. At the K' point, on the other hand, $\kappa'_{\nu\varphi}(0) = (2\pi/L)[(1/3) + \varphi]$ and the corresponding band gap is given by $\varepsilon^{K'}_{G\varphi}(0) = (2/3)(2\pi\gamma/L)(1 + 3\varphi)$. Therefore, the band gaps of the K and K' points, degenerate in the absence of φ, split in the presence of φ. The splitting is proportional to the flux, i.e.,

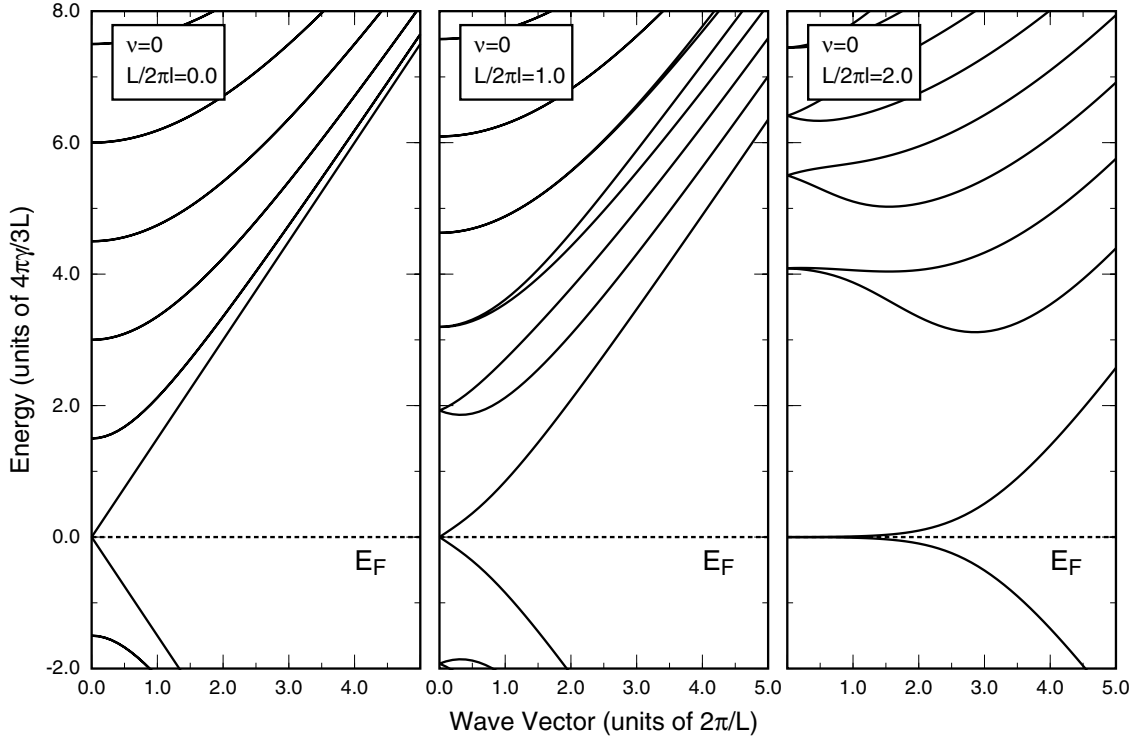$$\varepsilon^K_{G\varphi}(0) - \varepsilon^{K'}_{G\varphi}(0) = -2\tilde{\varepsilon}_0\varphi, \qquad (3.32)$$

Fig. 12   Some examples of calculated energy bands of a metallic tube in magnetic fields perpendicular to the axis.

Circumference (nm)		5	10	20	40	80
Diameter (nm)		1.6	3.2	6.4	12.7	25.5
Gap (meV)		541	270	135	68	34
Magnetic	$\phi = \phi_0$	2080	520	130	32	8
Field (T)	$(L/2\pi l)^2 = 1$	1040	260	65	16	4

Table II   Some examples of magnetic-field strength corresponding to the conditions $(L/2\pi l)^2 = 1$ and $\phi/\phi_0 = 1$ as a function of the circumference and the radius. The band gap of a semiconducting nanotube is also shown. ($\gamma = 0.646$ eV·nm).

with $\tilde{\varepsilon}_0 = 4\pi\gamma/L$. This splitting was recently observed in optical absorption and emission spectra.[46]

The second conduction and valence bands are given by $n = +1$ for the K point and $n = -1$ for the K' point. The corresponding band gaps are given by $\varepsilon_{G\varphi}^K(+1) = (2/3)(2\pi\gamma/L)(2+3\varphi)$ and $\varepsilon_{G\varphi}^{K'}(-1) = (2/3)(2\pi\gamma/L)(2-3\varphi)$. The amount of the splitting is same as that of the lowest gap, but the direction is different, i.e.,

$$\varepsilon_{G\varphi}^K(+1) - \varepsilon_{G\varphi}^{K'}(-1) = +2\frac{4\pi\gamma}{L}\varphi. \qquad (3.33)$$

The results for $\nu = -1$ can be obtained by exchanging K and K' points.

3.5 Landau Levels

In the presence of a magnetic field B perpendicular to the tube axis, the effective field for electrons in a CN is given by the component perpendicular to the surface, i.e., $B(x) = B\cos(2\pi x/L)$. The corresponding vector potential can be chosen as

$$\boldsymbol{A} = \left(0, \frac{LB}{2\pi}\sin\frac{2\pi x}{L}\right). \qquad (3.34)$$

The parameter characterizing its strength is given by

$$\zeta = \left(\frac{L}{2\pi l}\right)^2 = \left(\frac{R}{l}\right)^2, \qquad (3.35)$$

where l is the magnetic length defined by eq. (2.36) and R is the radius of CN. In the case $\zeta \ll 1$, the field can be regarded as a small perturbation, while in the case $\zeta \gg 1$, Landau levels are formed on the cylinder surface.

Figure 12 gives some examples of energy bands of a metallic CN in perpendicular magnetic fields,[12] which clearly shows the formation of flat Landau levels at the Fermi level in high fields. It is worth mentioning that there is no difference in the spectra between metallic and semiconducting CN's and in the presence and absence of an AB flux for $(L/2\pi l)^2 \gg 1$, because the wave function is localized in the circumference direction and the boundary condition becomes irrelevant. Energy levels in strong magnetic fields were calculated also in a nearest-neighbor tight-binding model.[47,48]

Table II shows some examples of magnetic-field strength corresponding to the conditions $(L/2\pi l)^2 = 1$ and $\phi/\phi_0 = 1$ as a function of the circumference and the radius. For a typical single-wall armchair nanotube having circumference $L = \sqrt{3}ma$ with $m = 10$, the required magnetic field is too large, but can be easily accessible by using a pulse magnet for typical multi-wall nanotubes with a diameter ~ 5 nm.

In a metallic nanotube, the wavefunctions are analytically obtained for $\varepsilon = 0$.[49] First, define a non-unitary matrix

$$P(\boldsymbol{r}) = \begin{pmatrix} \exp[-\zeta(\boldsymbol{r})] & 0 \\ 0 & \exp[+\zeta(\boldsymbol{r})] \end{pmatrix}, \qquad (3.36)$$

with

$$\zeta(\boldsymbol{r}) = \zeta\cos\frac{2\pi x}{L}. \qquad (3.37)$$

Then, we have

$$P(\boldsymbol{r})\mathcal{H}P(\boldsymbol{r}) = \mathcal{H}_0, \qquad (3.38)$$

for the K point, where $\mathcal{H}_0$ is the Hamiltonian in the absence of a magnetic field. This shows that for an eigen wave-function $\boldsymbol{F}_0^K(\boldsymbol{r})$ of $\mathcal{H}_0$ at $\varepsilon = 0$, i.e., $\mathcal{H}_0\boldsymbol{F}_0^K(\boldsymbol{r}) = 0$, the function $P(\boldsymbol{r})\boldsymbol{F}_0^K(\boldsymbol{r})$ satisfies the corresponding equation $\mathcal{H}P(\boldsymbol{r})\boldsymbol{F}_0^K(\boldsymbol{r}) = 0$ in nonzero B.

Therefore, the wave functions are given by

$$\boldsymbol{F}_{sk}^K = \frac{1}{\sqrt{2A}} \begin{pmatrix} -\mathrm{i}s(k/|k|)F_-(x) \\ F_+(x) \end{pmatrix} \exp(\mathrm{i}ky), \qquad (3.39)$$

with

$$F_\pm(x) = \frac{1}{\sqrt{LI_0(2\zeta)}} \exp\left(\pm\zeta\cos\frac{2\pi x}{L}\right), \qquad (3.40)$$

where $s = +1$ and -1 for the conduction and valence band, respectively, and $I_0(z)$ is the modified Bessel function of the first kind defined as

$$I_0(z) = \int_0^\pi \frac{\mathrm{d}\theta}{\pi} \exp(z\cos\theta). \qquad (3.41)$$

In high magnetic fields ($\zeta \gg 1$), $\boldsymbol{F}_-$ is localized around $x = \pm L/2$, i.e., at the bottom side of the cylinder and $\boldsymbol{F}_+$ is localized around the top side $x = 0$. The corresponding eigen-energies are given by $\varepsilon_s(k) = s\gamma|k|/I_0(2\zeta)$ which gives the group velocity $v = \gamma/\hbar I_0(2\zeta)$, and the density of states $D(\varepsilon) = I_0(2\zeta)/\pi\gamma$ at at $\varepsilon = 0$. We should note that

$$I_0(2\zeta) \approx \begin{cases} 1 + \zeta^2 + \cdots & (\zeta \ll 1), \\ e^{2\zeta}/\sqrt{4\pi\zeta} & (\zeta \gg 1). \end{cases} \qquad (3.42)$$

This means that the group velocity for states at $\varepsilon = 0$ decreases and consequently the density of states increases exponentially with the increase of the magnetic field in the high-field regime. The wavefunction for the K' point can be obtained in a similar manner.

3.6 Trigonal Warping

In thin nanotubes various effects, neglected completely in the present approximation scheme, start to manifest themselves. First, the trigonal warping of the bands which increases when the energy is away from that at the K and K' point should be considered. In the $\boldsymbol{k}\cdot\boldsymbol{p}$ scheme the warping can be incorporated by the inclusion of a higher order $\boldsymbol{k}\cdot\boldsymbol{p}$ term.[47] For the K point, for example, the Hamiltonian becomes

$$\mathcal{H} = \gamma \begin{pmatrix} 0 & \hat{k}_x - i\hat{k}_y + \dfrac{\delta a}{4\sqrt{3}}e^{3i\eta}(\hat{k}_x + i\hat{k}_y)^2 \\ \hat{k}_x + i\hat{k}_y + \dfrac{\delta a}{4\sqrt{3}}e^{-3i\eta}(\hat{k}_x - i\hat{k}_y)^2 & 0 \end{pmatrix}, \qquad (3.43)$$

with δ being a dimensionless constant of the order of unity ($\delta = 1$ in a nearest-neighbor tight-binding model). This gives trigonal warping of the band around the K point in 2D graphite. Figure 13 shows some examples of equi-energy lines for $\delta = 1$.

This Hamiltonian gives the energy bands

$$\varepsilon_{s,n,k} \approx s\gamma\Big[\kappa_{\nu\varphi}(n)^2\Big(1 + \frac{\delta a\kappa_{\nu\varphi}(n)}{2\sqrt{3}}\cos 3\eta\Big) \\ + \Big(1 - \frac{\sqrt{3}\delta a\kappa_{\nu\varphi}(n)}{2}\cos 3\eta\Big)(k - \Delta k)^2\Big]^{1/2}, \qquad (3.44)$$
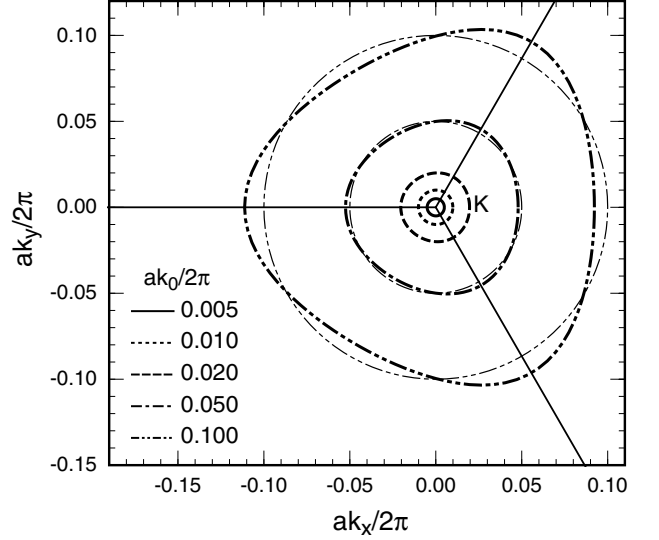

Fig. 13 Some examples of equi-energy lines in the vicinity of a K point in the 2D graphite in the presence of a trigonal warping for $\delta = 1$ (thick lines). The wave vector k_0 is the radius of the circular Fermi line in the absence of warping (thin lines), i.e., $\varepsilon = \pm\gamma k_0$ for given energy ε.

with

$$\Delta k = \frac{\sqrt{3}\delta a}{4}\kappa_{\nu\varphi}(n)^2\sin 3\eta. \qquad (3.45)$$

It gives rise to a shift in the origin of k by $\Delta k \propto \sin 3\eta$ which becomes maximum for $\eta = \pi/6$ (armchair nanotube). The band gap becomes

$$\varepsilon_{G\varphi}^K(n) \approx 2\gamma|\kappa_{\nu\varphi}(n)|\Big(1 + \frac{\delta a\kappa_{\nu\varphi}(n)}{4\sqrt{3}}\cos 3\eta\Big), \qquad (3.46)$$

and the band-edge effective mass m^* becomes

$$\frac{1}{m^*} \approx \frac{s\gamma}{\hbar^2|\kappa_{\nu\varphi}(n)|}\Big(1 - \frac{7\delta a\kappa_{\nu\varphi}(n)}{4\sqrt{3}}\cos 3\eta\Big). \qquad (3.47)$$

The correction of the effective mass is seven times as large as that of the band gap and they are both largest for $\eta = 0$ (zigzag nanotube).

Figures 14 (a) and (b) show the comparison of the band gap and the effective mass, respectively, with those obtained in the nearest neighbor tight-binding model for which $\delta = 1$. Figure 14 (b) shows a considerable dependence of the band-edge effective mass on the chirality, i.e., on ν and η, particularly for high-energy bands. The tight-binding results are reproduced almost exactly by the inclusion of higher-order terms.

In the presence of a magnetic field perpendicular to the axis, the higher order term was shown to cause the appearance of a small band-gap except in armchair nanotubes and a shift of the wave vector corresponding to $\varepsilon = 0$ in armchair nanotubes.[47]

3.7 Curvature

In thin nanotubes effects of a nonzero curvature should also be considered. The nonzero curvature causes a shift in the origin of $\hat{k}_x$ and $\hat{k}_y$ in the $\boldsymbol{k}\cdot\boldsymbol{p}$ Hamiltonian.[22,50] The shift in the circumference x direction can be replaced by an effective magnetic flux passing through the cross section, i.e., $\Delta k_x = (2\pi/L)(\phi/\phi_0)$,
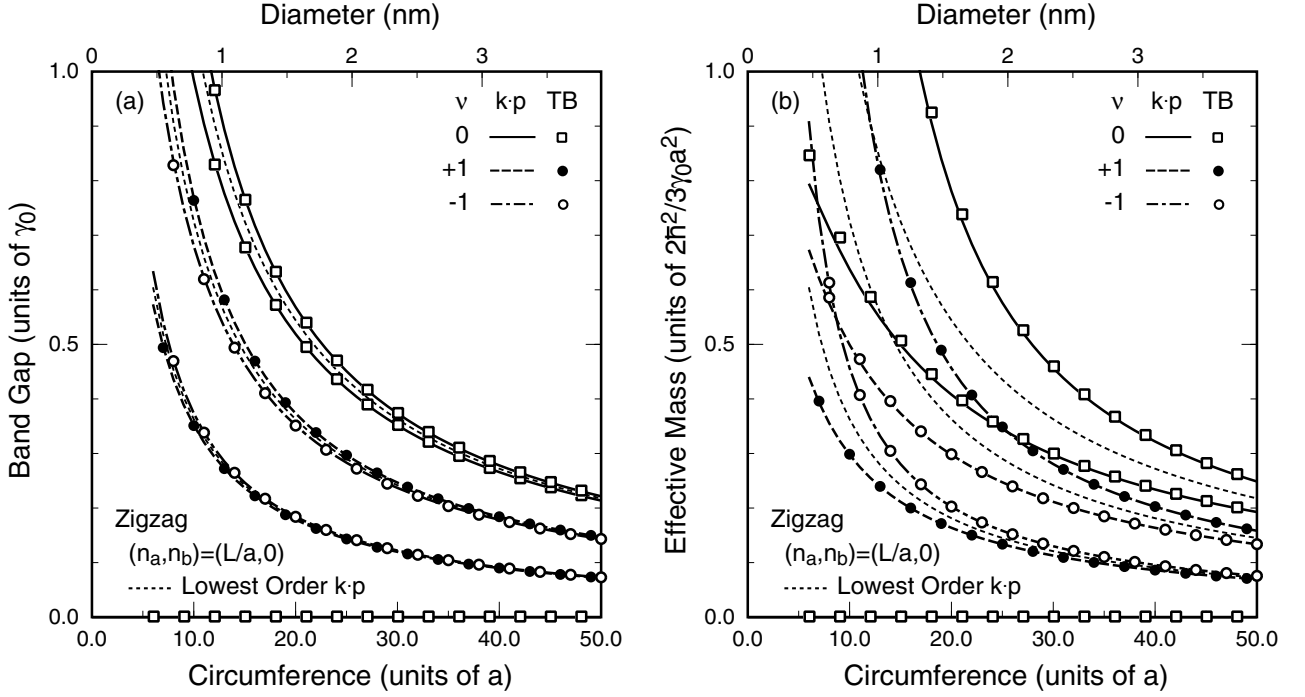
Fig. 14 Comparison of (a) the band gap and (b) the effective mass of zigzag nanotubes obtained in the higher order **$k\cdot p$** approximation with those of a nearest neighbor tight-binding (TB) model. The dotted lines represent results in the absence of trigonal warping. We have $2\hbar^2/3\gamma_0 a^2 \approx 0.838 \times m_0/\gamma_0$ with γ_0 in eV units, where m_0 is the free electron mass.

although the effective flux has a different signature between the K and K' points. For the K point, for example, it was estimated as[22]

$$\frac{\phi}{\phi_0} = -\frac{2\pi}{4\sqrt{3}}\frac{a}{L}p\cos 3\eta, \qquad (3.48)$$

with $p = 1 - (3/8)(\gamma'/\gamma)$, $\gamma' = -(\sqrt{3}/2)V_{pp}^\pi a$, and $\gamma = -(\sqrt{3}/2)(V_{pp}^\sigma - V_{pp}^\pi)a$, where η is the chiral angle, and V_{pp}^π and V_{pp}^σ are the conventional tight-binding parameters for neighboring p orbitals.[22] The curvature effect is largest in zigzag nanotubes with $\eta = 0$.

For usual parameters, we have $\gamma'/\gamma \sim 8/3$ and therefore it is very difficult to make a reliable estimation of p although $|p| < 1$.[22] For negative p, the first band gap tends to be reduced and the second gap enhanced for $\nu = +1$ and the behavior is opposite for positive p. Figure 15 shows the band gap and effective mass of zigzag nanotubes obtained in the lowest order **$k\cdot p$** approximation in the presence of curvature effects with (a) $p = -0.5$ and (b) $p = +0.5$. In the presence of finite curvature, nanotubes metallic in its absence become narrow-gap semiconductors except in armchair nanotubes with $\eta = \pi/6$ and the gap is largest in zigzag nanotubes as has been shown first in ref. 5. This fact is independent of the signature of the parameter p. In semiconducting nanotubes, however, effects for $\nu = +1$ and $\nu = -1$ become opposite depending on the signature of p.

A finite curvature gives rise to the shift Δk of the wave vector in the axis direction, although it does not cause any appreciable effect. For the K point we have

$$\Delta k = -\frac{\pi^2 a}{4\sqrt{3}L^2}\left(\frac{5}{8}\frac{\gamma'}{\gamma} - 1\right)\sin 3\eta. \qquad (3.49)$$

Several first-principles calculations were reported on the

band structure of nanotubes, which seems to show that the shift is quite sensitive to details of methods. In fact, ref. 5 gave $\Delta k < 0$ for $[n_a, n_b] = [12, 6]$ (so-called (6,6) armchair nanotube) and ref. 6 gave $\Delta k > 0$ for $[n_a, n_b] = [10, 5]$ (so-called (5,5) tube). The situation is expected to be applicable to the signature of p.

3.8 Strain

As will be shown in §8, the presence of a lattice distortion (u_x, u_y, u_z) causes a shift in $\hat{k}_x$ and $\hat{k}_y$ in the **$k\cdot p$** Hamiltonian.[29,50–53] The shift in the x direction can be replaced by an effective magnetic flux (its signature is opposite between the K and K' points).[29,54] The flux for the K point is written as

$$\frac{\phi}{\phi_0} = \frac{Lg_2}{2\pi\gamma}[(u_{xx} - u_{yy})\cos 3\eta - 2u_{xy}\sin 3\eta], \qquad (3.50)$$

where $u_{\mu\nu}$ $(\mu, \nu = x, y)$ denotes the lattice strain given by

$$u_{xx} = \frac{\partial u_x}{\partial x} + \frac{u_z}{R}, \quad u_{yy} = \frac{\partial u_y}{\partial y}, \quad u_{xy} = \frac{1}{2}\left(\frac{\partial u_x}{\partial y} + \frac{\partial u_y}{\partial x}\right), \qquad (3.51)$$

with $R = L/2\pi$ being the CN radius, and g_2 is the electron phonon interaction energy given by $g_2 \sim -V_{pp}^\pi/2$ with V_{pp}^π being the transfer integral of nearest-neighbor π orbitals.[29,54] This shows that twist and stretch deformation give rise to flux in armchair $\eta = \pi/6$ and zigzag $(\eta = 0)$ nanotubes, respectively.

The critical difference lies in the fact that the effective flux changes its signature between K and K' points as in the case of effects of finite curvature, showing that there is only a shift and no splitting between the K and K' points like in the case of magnetic flux. Figure 11 contains the band edges as a function of the effective flux for a semiconducting tube with $\nu = 1$. The results for
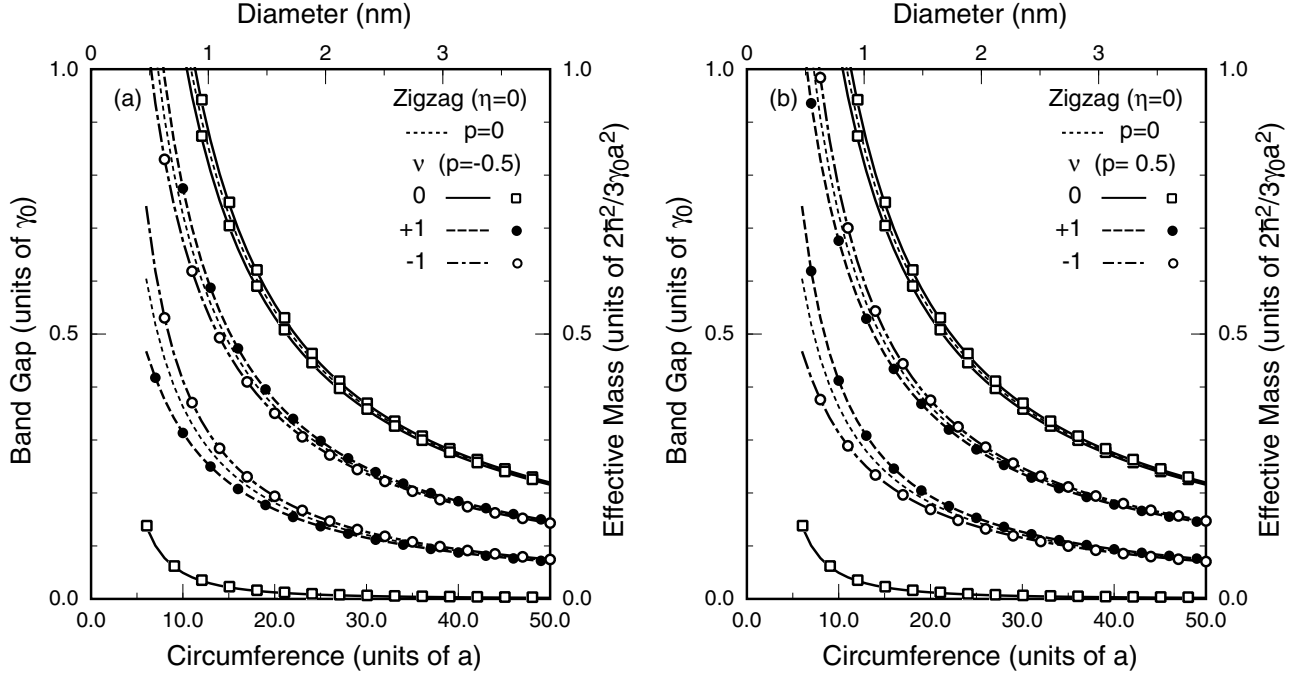
Fig. 15 The band gap and the effective mass obtained in the lowest order $\boldsymbol{k \cdot p}$ approximation in zigzag nanotubes when curvature effects are included. (a) $p = -0.5$ and (b) $p = +0.5$. The dotted lines represent results in the absence of curvature effects.

$\nu = -1$ are given by those with $\nu = +1$ of the K' point in the presence of the magnetic flux. The band gap increases or decreases linearly in proportion to the strain depending on the signature of ϕ, the index n, and the structure specified by ν. When the strain is such that it increases the first gap with $n = 0$, for example, the second gap ($n = +1$ for the K point and $n = -1$ for the K' point) decreases with the strain. These behaviors are qualitatively in agreement with optical experiments.[55,56]

§4. Magnetic Properties

Energy bands in AB flux and perpendicular magnetic field discussed in the previous section can be used for the study of magnetic properties of nanotubes.[13,21] In the following, $B_\parallel$ and $B_\perp$ represent the magnetic field in the direction parallel and perpendicular to the tube axis, respectively, $M^\parallel$ and $M^\perp$ the corresponding magnetic moments, and $\chi^\parallel$ and $\chi^\perp$ the susceptibilities. The spin-Zeeman energy is small and therefore neglected for simplicity. The free energy is given by

$$F = N\mu - k_B T \sum_\alpha g_0(\varepsilon_\alpha) \ln\left[1 + \exp\left(-\frac{\varepsilon_\alpha - \mu}{k_B T}\right)\right], \quad (4.1)$$

where α denotes a set of whole quantum numbers specifying the energy band, T is temperature, k_B is the Boltzmann constant, and μ is the chemical potential satisfying the condition that the electron number is constant. Further, we have introduced a cutoff function $g_0(\varepsilon)$ in order to extract contributions of states in the vicinity of the K and K' points. It is chosen as

$$g_0(\varepsilon) = \frac{\varepsilon_c^{\alpha_c}}{|\varepsilon|^{\alpha_c} + \varepsilon_c^{\alpha_c}}, \quad (4.2)$$

which contains two parameters α_c and ε_c. Results do not depend on these parameters, as long as ε_c is sufficiently

large and α_c is not extremely large. In fact, this cutoff function can be eliminated in an appropriate procedure.

The magnetic moment is calculated by taking a first derivative of F with respect to the field under the condition that the total number of electrons is fixed. The result is represented as

$$M^{\parallel,\perp} = \int_{-\infty}^{\infty} d\varepsilon\left(-\frac{\partial f(\varepsilon)}{\partial \varepsilon}\right) M^{\parallel,\perp}(\varepsilon), \quad (4.3)$$

where $f(\varepsilon)$ is the Fermi distribution function and $M^{\parallel,\perp}(\varepsilon)$ is the magnetic moment at zero temperature for the Fermi level ε, given by

$$M^{\parallel,\perp}(\varepsilon) = -\sum_\alpha \frac{\partial \varepsilon_\alpha}{\partial B_{\parallel,\perp}} g_1(\varepsilon_\alpha)\theta(\varepsilon - \varepsilon_\alpha), \quad (4.4)$$

where

$$g_1(\varepsilon) = g_0(\varepsilon) + \varepsilon\frac{\partial g_0(\varepsilon)}{\partial \varepsilon}, \quad (4.5)$$

and $\theta(t)$ is the step function defined by

$$\theta(t) = \begin{cases} 1 & (t > 0); \\ 0 & (t < 0). \end{cases} \quad (4.6)$$

The zero-field susceptibility per unit area at nonzero temperatures can also be written in terms of the susceptibility at zero temperature in the same way as the magnetic moment,

$$\chi^{\parallel,\perp} = \int_{-\infty}^{\infty} d\varepsilon\left(-\frac{\partial f(\varepsilon)}{\partial \varepsilon}\right)\chi^{\parallel,\perp}(\varepsilon), \quad (4.7)$$

with

$$\chi^{\parallel,\perp}(\varepsilon) = \frac{1}{AL}\lim_{B_{\parallel,\perp}\to 0}\frac{\partial M^{\parallel,\perp}(\varepsilon)}{\partial B_{\parallel,\perp}}. \quad (4.8)$$

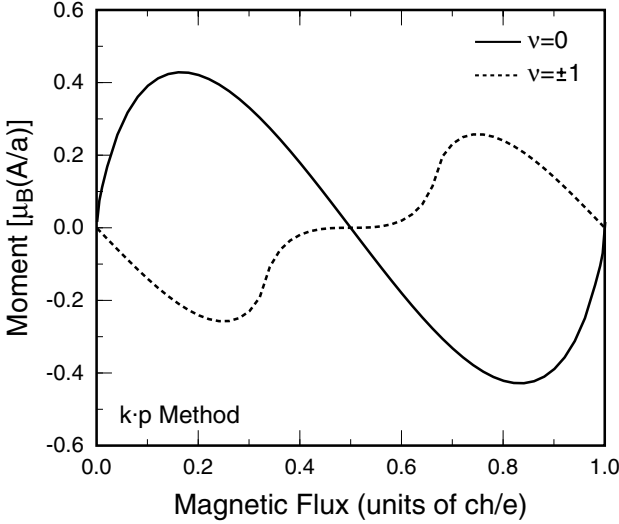First, we consider the magnetization in the presence of AB flux at zero temperature. The magnetization is

Fig. 16 Magnetic moment of metallic (solid line) and semiconducting (dotted line) CN's versus magnetic flux parallel to the tube axis.
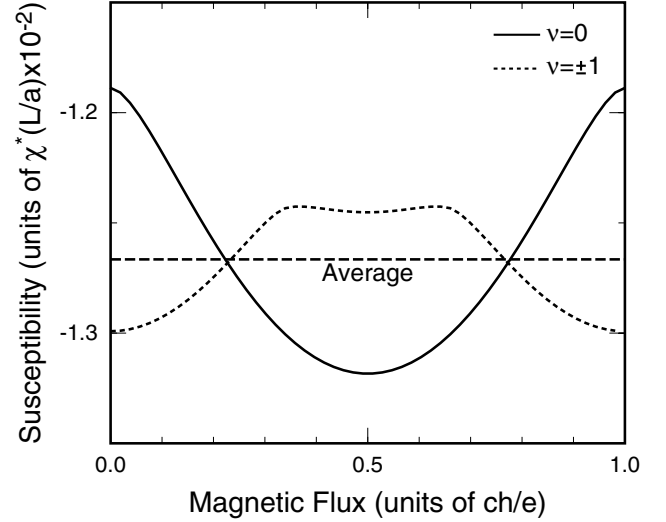

Fig. 17 Susceptibility of metallic (solid line) and semiconducting (dotted line) CN's versus magnetic flux parallel to the tube.

written as

$$M^{\parallel}(\varphi) = 2\mu_B \frac{A}{a} \frac{2ma\gamma}{\hbar^2} \left[W_1\left(\varphi + \frac{\nu}{3}\right) + W_1\left(\varphi - \frac{\nu}{3}\right) \right], \quad (4.9)$$

where $\mu_B = e\hbar/2mc$ is the Bohr magneton and $W_1(\varphi)$ is dimensionless quantity given by

$$W_1(\varphi) = \frac{1}{4\pi} \sum_{n=-\infty}^{\infty} \int_{-\infty}^{\infty} d\tilde{k} \, \frac{\kappa_{0\varphi}(n)}{\sqrt{\kappa_{0\varphi}(n)^2 + k^2}} \, g_1[\varepsilon(n+\varphi, k)],$$
$$(4.10)$$

with $\tilde{k} = Lk/2\pi$. This can be calculated analytically as

$$W_1(\varphi) = -\frac{1}{2\pi} \int_0^{\varphi} \ln(2\sin\pi t) \, dt, \quad (4.11)$$

for $0 < \varphi < 1$.[19] The value of $W_1(\varphi)$ outside this region is obtained by using $W_1(\varphi + j) = W_1(\varphi)$ with integer j.

In the vicinity of $\varphi = j$ with j being an integer, $W_1 \approx -(2\pi)^{-1}(\varphi - j)\ln|\varphi - j|$. Therefore, the moment itself vanishes but its derivative diverges logarithmically (positive infinite) at $\varphi = j$ and metallic CN's exhibit paramagnetism in a weak parallel field. Figure 16 shows the magnetic moment of a metallic and semiconducting CN as a function of φ. The magnetic moment is a periodic function of flux with period of magnetic flux quantum since the moment is induced by the AB flux. In a weak field metallic and semiconducting CN's show paramagnetism and diamagnetism, respectively.

In the presence of a weak magnetic field perpendicular to the tube axis, the vector potential (3.34) has matrix elements between states with quantum number n and n' where $n' = n \pm 1$ and therefore the energy shift $\Delta\varepsilon_\alpha$ appears in general in the second order in magnetic-field strength $B_\perp$. The shift in the total energy becomes

$$\Delta E = \sum_\alpha \left[(\varepsilon_\alpha + \Delta\varepsilon_\alpha) g_0(\varepsilon_\alpha + \Delta\varepsilon_\alpha) - \varepsilon_\alpha g_0(\varepsilon_\alpha) \right]$$
$$\approx \sum_\alpha \Delta\varepsilon_\alpha g_1(\varepsilon_\alpha), \quad (4.12)$$

where the summation is over occupied states α. The zero-field susceptibility per unit area becomes

$$\chi^{\perp} = -\sum_\alpha \frac{\partial^2 \Delta\varepsilon_\alpha}{\partial B_\perp^2} g_1(\varepsilon_\alpha). \quad (4.13)$$

After a straightforward manipulation, $\chi(\varphi)$ is calculated as

$$\chi^{\perp}(\varphi) = -2\chi^* \frac{L}{a} \left[W_2\left(\varphi + \frac{\nu}{3}\right) + W_2\left(\varphi - \frac{\nu}{3}\right) \right], \quad (4.14)$$

where $W_2(\varphi)$ is the dimensionless quantity defined by

$$W_2(\varphi) = \frac{1}{2\pi^4} \sum_{n=-\infty}^{\infty} \int_{-\infty}^{\infty} d\tilde{k} \, \frac{\sqrt{(n+\varphi)^2 + \tilde{k}^2}}{1 - 4(n+\varphi)^2} g_1[\varepsilon(n+\varphi, k)],$$
$$(4.15)$$

and χ^* is a characteristic susceptibility defined by

$$\chi^* = \frac{2\pi\gamma}{a} \left(\frac{\pi a^2}{\phi_0}\right)^2 \frac{1}{a^2}, \quad (4.16)$$

corresponding to 1.46×10^{-4} emu/mol or 1.21×10^{-5} emu/g for $\gamma = 0.646$ eV·nm. Figure 17 shows the susceptibility as a function of φ.

The function $W_2(\varphi)$ varies only weakly as a function of φ and the approximate value can be obtained by taking the average over φ as $\bar{W}_2 = (32\pi^2)^{-1}$. Then, the (averaged) susceptibility becomes independent of whether the nanotube is metallic or semiconducting and is given by

$$\bar{\chi}^{\perp} = -\frac{1}{8\pi^2} \frac{L}{a} \chi^*. \quad (4.17)$$

The susceptibility is proportional to the circumference L and therefore diverges in the limit of infinitely large L. This dependence is closely related to the susceptibility of a 2D graphite sheet. In fact, the following expression was derived for the susceptibility per unit area of a graphite sheet:[57]

$$\chi = -\frac{\gamma^2}{3\pi} \frac{1}{\mu} \left(\frac{e}{c\hbar}\right)^2. \quad (4.18)$$

For a single ideal 2D graphite layer, the Fermi energy μ vanishes and the susceptibility diverges at zero tem-
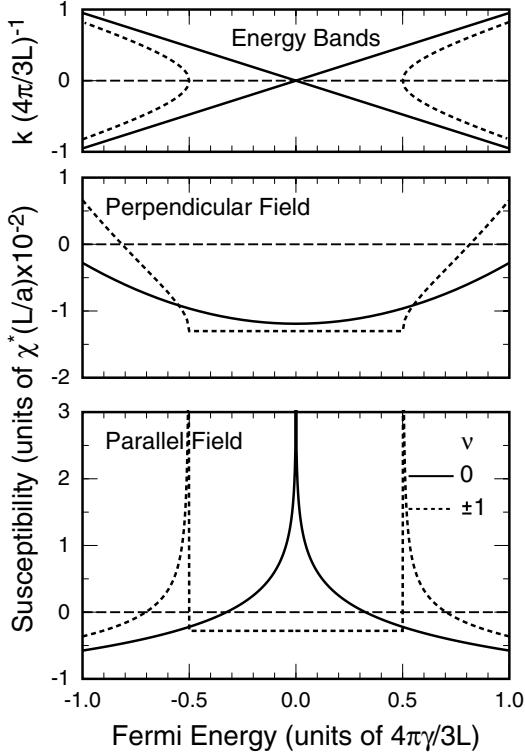
Fig. 18 The top panel shows the band structure of metallic (solid lines) and semiconducting (dotted lines) CN's. Calculated susceptibility of metallic (solid lines) and semiconducting (dotted lines) CN's in the direction of perpendicular (middle panel) and parallel (bottom panel) to the tube axis are shown as a function of the chemical potential at zero temperature.
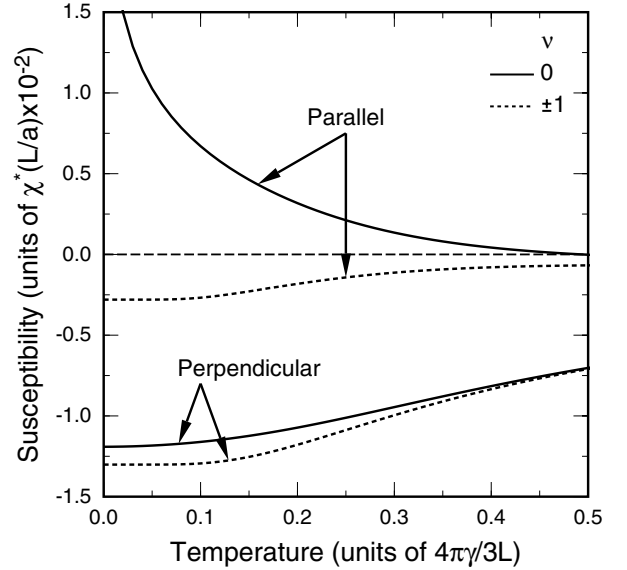

Fig. 19 Calculated susceptibility of metallic (solid lines) and semiconducting (dotted lines) CN's in the direction parallel and perpendicular to the tube axis versus temperature.
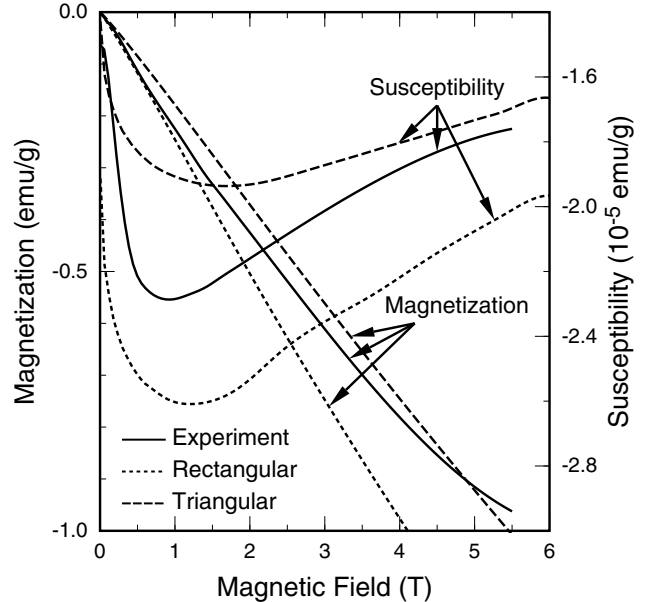

Fig. 20 Calculated ensemble average of magnetic moment and differential susceptibility for CN's with rectangular (dotted lines) and triangular (dashed lines) circumference distribution having $L_{mn} = 2.2$ nm and $L_{mx} = 94.3$ nm. Solid lines denote the experimental results of magnetization and differential susceptibility.[58]

perature. The susceptibility of CN, $\bar{\chi}^{\perp}$, can be obtained from that of 2D graphite if we replace μ by $0.85 \times \gamma(2\pi/L)$ which is the typical confining energy due to a finite circumference.

Numerical results are shown in Fig. 18 as a function of the Fermi energy. Both metallic and semiconducting CN's show positive divergent susceptibility in the parallel field where the Fermi energy lies at band edges. The divergence for metallic CN's is logarithmic as has been discussed above, while that for semiconducting CN's corresponds to that of the density of states at band edges. When the Fermi energy moves away from band edges, the parallel susceptibility becomes negative (diamagnetic). For a perpendicular field, CN is diamagnetic but turns into paramagnetic when the Fermi energy becomes away from $\varepsilon = 0$. These results were obtained numerically also in a nearest-neighbor tight-binding model.[59]

Figure 19 shows the susceptibility in the parallel and perpendicular directions for undoped tubes as a function of temperature. The positive susceptibility of metallic CN's in the parallel direction decreases rapidly with temperature, while the other negative susceptibilities rise very slowly. The results show clearly that both semiconducting and metallic nanotubes have a lower energy when aligned in the direction of a magnetic field, i.e, nanotubes have a strong tendency to align in the field direction. The difference $|\chi^{\perp} - \chi^{\parallel}|$ and its dependence on the circumference were estimated recently in optical experiments and gave results in semi-quantitative agree-

ment with those obtained above.[60]

Because interactions between adjacent layers of a multi-wall CN are weak, its magnetic properties are given by those of an ensemble of single-wall CN's. By assuming that two thirds of nanotubes are semiconducting and remaining one third metallic, we can calculate magnetization and susceptibility of ensembles of multi-wall nanotubes. Figure 20 compares results of such calculations with experiments.[58] In the calculation a rectangular distribution is assumed for the circumference in the range $L_{mn} = 2.2$ nm corresponding to the thinnest multi-wall CN so far observed and $L_{mx} = 94.3$ nm corresponding to the thickest CN. Another choice is a triangular distri-

bution with its maximum at $L = L_{\mathrm{mn}}$ and minimum at $L = L_{\mathrm{mx}}$. The latter roughly corresponds to the fact that thick multi-wall tubes consist of many walls. The calculation can explain the experiments qualitatively, but detailed information on the distribution of CN's is indispensable for quantitative comparison.

§5. Optical Properties

Experimentally, the one-dimensional electronic structure of CN was directly observed by scanning tunneling microscopy and spectroscopy[61,62] and the resonant Raman scattering.[63] However, most direct and accurate information can be obtained by optical spectroscopy.

5.1 Dynamical Conductivity

We shall consider the optical absorption of CN using the linear response theory. For this purpose it it convenient to use the angle $\theta \equiv 2\pi x/L$ measured from the top side of the nanotube instead of x. We first expand electric field $E_\xi(\theta,\omega)$ and induced current density $j_\xi(\theta,\omega)$ into a Fourier series:

$$E_\xi(\theta,\omega) = \sum_l E_\xi^l(\omega)\exp(\mathrm{i}l\theta - \mathrm{i}\omega t),$$
$$j_\xi(\theta,\omega) = \sum_l j_\xi^l(\omega)\exp(\mathrm{i}l\theta - \mathrm{i}\omega t),$$

(5.1)

with integer l, where ξ denotes x or y. It is quite straightforward to show that the induced current has the same Fourier component as that of the electric field as follows:

$$j_\xi^l(\omega) = \sigma_{\xi\xi}^l(\omega)E_\xi^l(\omega),$$

(5.2)

where $\sigma_{\xi\xi}^l(\omega)$ is the dynamical conductivity.

The dynamical conductivity is calculated using the Kubo formula as

$$\sigma_{\xi\xi}^l(\omega) = \frac{4\hbar}{\mathrm{i}AL}\sum_{n,k}\sum_{s,s'}\frac{|(s,n,k|\hat{j}_\xi^l|s',n+l,k)|^2}{\varepsilon_{s,n,k} - \varepsilon_{s',n+l,k}}$$
$$\times \frac{f(\varepsilon_{s',n+l,k})[1 - f(\varepsilon_{s,n,k})]2\hbar\omega}{(\varepsilon_{s,n,k} - \varepsilon_{s',n+l,k})^2 - (\hbar\omega)^2 - 2\mathrm{i}\hbar^2\omega/\tau}$$

(5.3)

where phenomenological relaxation time τ has been introduced. where $f(\varepsilon)$ is the Fermi distribution function and the factor 2 comes from the spin degeneracy. The

current-density operator $\hat{j}_\xi^l$ at the K point is given by

$$\hat{j}_\xi^l = \frac{-e}{\mathrm{i}\hbar}[\hat{\xi}, \gamma\vec{\sigma}\cdot\hat{\mathbf{k}}]\mathrm{e}^{-\mathrm{i}l\theta} = -\frac{e\gamma}{\hbar}\sigma_\xi \mathrm{e}^{-\mathrm{i}l\theta}.$$

(5.4)

At the K' point, operator $\hat{j}_x^l$ is the same as that at the K' point but j_y^l has the opposite sign of that at the K point. The factor $|(s,n,k|j_\xi^l|s',n+l,k)|^2$, however, provides the same value for both K and K' points.

5.2 Parallel Polarization

When the polarization of external electric field $\mathbf{D}$ is parallel to the tube axis, the Fourier components of a total field are written as

$$E_y^l = D_y\delta_{l,0}.$$

Thus the absorption in a unit area is given by

$$P_y(\omega) = \frac{1}{2}\frac{1}{2\pi}\sum_l\int_0^{2\pi}\mathrm{d}\theta\mathrm{Re}[j_y^l(\omega)E_y^{l\,*}] = \frac{1}{2}\mathrm{Re}[\sigma_{yy}^{l=0}(\omega)]D_y^2.$$

(5.5)

For $l = 0$, transitions occur between bands with the same band index n as is seen from eq. (5.3). Since all the conduction bands are specified by different n's, there is no transition within conduction bands and within valence bands. At a band edge $k = 0$, in particular, the wave function is an eigen function of σ_x and therefore transitions between valence and conduction bands having the same index n are all allowed. An exception occurs for bands with $n = 0$ in a metallic nanotube. In this case the wave function is an eigenfunction of σ_y because $\kappa_{\nu\varphi}(n) = 0$ and therefore there is no matrix element between the conduction and valence bands with $n = 0$ for $j_y \propto \sigma_y$. Figure 21 shows such allowed transitions.

In the limit $\tau \to \infty$ absorption spectra except for intraband Drude terms is proportional to

$$\mathrm{Re}[\sigma_{yy}^{l=0}(\omega)] = \frac{e^2}{h}\sum_n\left[\frac{2\gamma\kappa_{\nu\varphi}(n)}{\hbar\omega}\right]^2\frac{4\pi\gamma\theta[|\hbar\omega| - 2\gamma|\kappa_{\nu\varphi}(n)|]}{L\sqrt{(\hbar\omega)^2 - [2\gamma\kappa_{\nu\varphi}(n)]^2}}.$$

(5.6)

The conductivity exhibits 1D singularity at the band gaps with same n.

5.3 Perpendicular Polarization

When an external electric field $\mathbf{D}$ is polarized in the direction perpendicular to the CN axis, the electric field has components $l = \pm 1$ and therefore transitions between states with $\Delta n = \pm 1$ become allowed in general. Figure
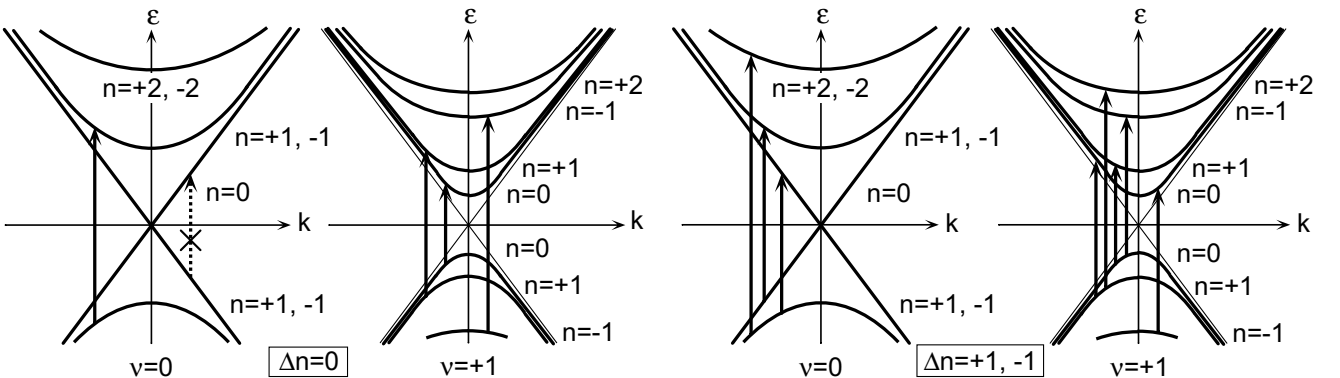

Fig. 21   The band structures of a metallic ($\nu = 0$) and semiconducting ($\nu = \pm 1$) CN. The allowed optical transitions for the parallel ($\Delta n = 0$) and perpendicular ($\Delta n = \pm 1$) polarization are denoted by arrows.

21 includes also allowed transitions for perpendicular polarization. At the band edges, however, there are some complications due to the fact that the band-edge ($k=0$) is always an eigen-state of σ_x and $j_x \propto \sigma_x$. In fact, transitions between states with same eigen-value of σ_x are allowed and those with different eigen-values are forbidden. This dependence disappears with the increase of k because the wave functions deviate from eigen-functions of σ_s.

When an external electric field is polarized in the direction perpendicular to the CN axis, effects of an electric field induced by the polarization of nanotubes should be considered. This depolarization effect is quite significant for absorption spectra, as shown below.

Suppose an external electric field $D_x^l \exp(il\theta - i\omega t)$ is applied in the direction normal to the tube axis and let j_x^l be the induced current. With the use of the equation of continuity

$$\frac{\partial}{\partial t}\rho^l e^{il\theta - i\omega t} + \frac{2\pi}{L}\frac{\partial}{\partial \theta}j_x^l e^{il\theta - i\omega t} = 0, \qquad (5.7)$$

the corresponding induced charge density localized on the cylinder surface is written as

$$\rho^l = \frac{2\pi}{L}\frac{l}{\omega}j_x^l. \qquad (5.8)$$

The potential $\phi(\theta)$ formed by a line charge along the axis direction at θ' with the density ρ is given at θ by

$$\phi(\theta) = -\frac{2\rho}{\kappa}\ln\left|\frac{L}{\pi}\sin\frac{\theta - \theta'}{2}\right|. \qquad (5.9)$$

Here, the static dielectric constant κ approximately describes effects of polarization of core states, σ bands, π bands except those lying in the vicinity of the Fermi level, and materials surrounding the nanotube. In bulk graphite we have $\kappa \approx 2.4$.[64] In nanotubes, this simple constant screening is a rough approximation because of the cylindrical form with hollow vacuum inside and surrounding material outside.

Then it is found that the induced charge leads to potential

$$\phi(\theta) = -2\frac{L}{2\pi}\int_0^{2\pi}d\theta'\frac{\rho^l}{\kappa}\exp(il\theta')\ln\left|\frac{L}{\pi}\sin\frac{\theta - \theta'}{2}\right|$$
$$= \frac{L}{\kappa|l|}\rho^l e^{il\theta} \equiv \phi^l e^{il\theta}. \qquad (5.10)$$

The potential gives rise to electric field $-(2\pi/L)(\partial\phi/\partial\theta)$ and therefore the total electric field is obtained as

$$E_x^l = D_x^l - il\frac{2\pi}{L}\phi^l = D_x^l - i|l|\frac{4\pi^2}{\kappa L\omega}j_x^l. \qquad (5.11)$$

With the use of $j_x^l = \sigma_{xx}^l E_x^l$ we get

$$j_x^l = \tilde{\sigma}_{xx}^l D_x^l, \qquad (5.12)$$

with

$$\tilde{\sigma}_{xx}^l = \sigma_{xx}^l\left(1 + i|l|\frac{4\pi^2}{\kappa L\omega}\sigma_{xx}^l\right)^{-1}. \qquad (5.13)$$

For the external field $\boldsymbol{D} = (D_x\sin\theta, 0)$, the Fourier components of the external field and the induced current
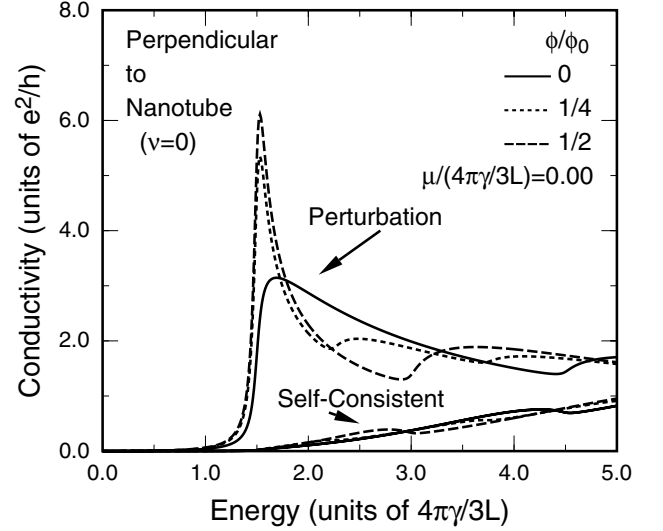

Fig. 22 Calculated real part of σ_{xx} (indicated by 'Perturbation') and $\tilde{\sigma}_{xx}$ (indicated by 'Self-Consistent') of undoped metallic CN's for $\varphi = 0$, $1/4$, and $1/2$.

are written as

$$D_x^l = \frac{D_x}{2i}\delta_{l,1} - \frac{D_x}{2i}\delta_{l,-1},$$
$$j_x^l = \frac{D_x}{2i}\sigma_{xx}^{l=1}(\omega)\delta_{l,1} - \frac{D_x}{2i}\sigma_{xx}^{l=-1}(\omega)\delta_{l,-1}. \qquad (5.14)$$

Thus the absorption is given by

$$P_x(\omega) = \frac{1}{2}\frac{1}{2\pi}\sum_l\int_0^{2\pi}d\theta\,\text{Re}[j_x^l(\omega)E_x^{l\,*}] = \frac{1}{4}\text{Re}[\tilde{\sigma}_{xx}(\omega)]D_x^2, \qquad (5.15)$$

with

$$\tilde{\sigma}_{xx} = \frac{1}{2}(\tilde{\sigma}_{xx}^{l=1} + \tilde{\sigma}_{xx}^{l=-1}). \qquad (5.16)$$

In Fig. 22 $\text{Re}\tilde{\sigma}_{xx}$ (indicated by 'Self-Consistent') and $\text{Re}\sigma_{xx}$ (indicated by 'Perturbation') are shown for a metallic CN with magnetic flux $\varphi = 0$, $1/4$, and $1/2$. The peaks around $(5/3)(2\pi\gamma/L)$ correspond to the allowed transitions at the band edges ($k=0$). Other transitions which are not allowed at the band edges and become allowed with the increase of k give weaker and broader structures in the absorption. In magnetic flux $\varphi = 0$, the peak of σ_{xx} is suppressed in comparison with the others. This is because of the absence of the divergence in the joint density of states at the band edge. These peaks disappear almost completely when the depolarization effect is taken into account.

To understand the strong suppression of absorption peaks for perpendicular polarization, we consider a simple model in which the real part of conductivity is proportional to a joint density of states of one-dimensional materials and the oscillator strength is constant. The model conductivity is written as

$$\text{Re}\,\sigma_{xx}(\omega) = \frac{ne^2}{m}\frac{\theta(\omega - \omega_1)\theta(\omega_2 - \omega)}{\sqrt{(\omega - \omega_1)(\omega_2 - \omega)}}, \qquad (5.17)$$

for $\omega > 0$, where $0 < \omega_1 < \omega_2$, n is the electron density in an unit area, and m is the mass of the electron. This conductivity satisfies the intensity sum rule given by

$$\frac{1}{\pi}\int_0^\infty d\omega\,\text{Re}\sigma_{xx}(\omega) = \frac{ne^2}{m}. \qquad (5.18)$$

By the use of the Kramers-Krönig relation, we get the imaginary part of the conductivity as

$$\mathrm{Im}\sigma_{xx}(\omega) = -\frac{\mathrm{P}}{\pi}\int_{-\infty}^{\infty}\mathrm{d}\omega'\frac{\mathrm{Re}\sigma_{xx}(\omega')}{\omega'-\omega}$$

$$= \begin{cases} 0 & (\omega_1 \le \omega \le \omega_2); \\ -\dfrac{ne^2}{m}\dfrac{1}{\sqrt{(\omega-\omega_1)(\omega-\omega_2)}} & (0 \le \omega < \omega_1); \\ +\dfrac{ne^2}{m}\dfrac{1}{\sqrt{(\omega-\omega_1)(\omega-\omega_2)}} & (\omega > \omega_2), \end{cases} \quad (5.19)$$

where P stands for the principal value. As is seen from eq. (5.15) absorption peaks exist at the frequency where $\mathrm{Re}[\tilde{\sigma}_{xx}(\omega)]$ diverges. From eq. (5.12) it is found that an absorption peak occurs at a frequency ω_p higher than the absorption edge ω_2. For $\omega_\mathrm{p} \gg \omega_2$, we have $\omega_\mathrm{p}^2 = (\pi/L)(4\pi ne^2/m)$, which is nothing but the plasma frequency corresponding to the three-dimensional electron density $\pi n/L$. This is the reason for the strong suppression of absorption peaks for perpendicular polarized field.

The above reasoning shows also that sharp interband transition may be observed even for the perpendicular polarization if exciton effects to be discussed in §6.6 are sufficiently large. If an exciton has a sufficiently large binding energy associated with bands edges corresponding to allowed transitions, it gives rise to a δ function peak in $\sigma_{xx}(\omega)$. Such a δ function peak is shifted by the depolarization effect but is likely to remain as an observable peak.

§6. Interaction Effects and Exciton

6.1 Effective Coulomb Interaction

Interaction effects on the band structure were calculated in the $\boldsymbol{k}\cdot\boldsymbol{p}$ scheme using a screened Hartree-Fock approximation together with exciton energy levels.[15] Calculations based on a full random-phase approximation (RPA) were performed later.[17] A brief review is given first on interaction effects based on the latter work.

The Coulomb potential between two electrons on the cylindrical surface at $\boldsymbol{r} = (x, y)$ and $\boldsymbol{r}' = (x', y')$ is written as[65−68]

$$\begin{aligned} &v(x-x', y-y') \\ &= \sum_q \exp[\mathrm{i}q(y-y')]\frac{2e^2}{\kappa A}K_0\Big(\frac{L|q|}{2\pi}\Big|2\sin\frac{\pi(x-x')}{L}\Big|\Big), \end{aligned}$$
$$(6.1)$$

where $K_n(t)$ is the modified Bessel function of the second kind. In the effective-mass approximation, this potential appears only in the diagonal part of the matrix $\boldsymbol{k}\cdot\boldsymbol{p}$ Hamiltonian, and the Coulomb matrix elements are given by

$$\langle\alpha, k, K; \beta', k'+q, K|v|\beta, k+q, K; \alpha', k', K\rangle$$
$$= \frac{1}{A}\delta_{n-m,n'-m'}\big(\boldsymbol{F}_{\alpha k}^{K*}\cdot\boldsymbol{F}_{\beta k+q}^{K}\big)\big(\boldsymbol{F}_{\beta' k'+q}^{K*}\cdot\boldsymbol{F}_{\alpha' k'}^{K}\big)v_{n-m}(q),$$
$$(6.2)$$

with

$$v_{n-m}(q) = \frac{2e^2}{\kappa}I_{|n-m|}\Big(\frac{L|q|}{2\pi}\Big)K_{|n-m|}\Big(\frac{L|q|}{2\pi}\Big), \quad (6.3)$$

where $I_n(t)$ is the modified Bessel function of the first kind and $\alpha = (s, n)$, $\beta = (s', m)$, etc. Matrix elements

corresponding to the scattering between the K and K' points are safely neglected because it involves a large momentum transfer.

In RPA, the Coulomb interaction is screened by the dynamical dielectric function $\varepsilon_{n-m}(q, \omega)$, given by

$$\varepsilon_{n-m}(q, \omega) = 1 + v_{n-m}(q)P_{n-m}(q, \omega). \quad (6.4)$$

The polarization function $P_{n-m}(q, \omega)$ is expressed as

$$P_{n-m}(q, \omega) = -\frac{2}{A}\sum_{G=K,K'}\sum_{n',m'}\sum_{k'}\delta_{n-m,n'-m'}$$
$$\times|\boldsymbol{F}_{\alpha,k}^{G*}\cdot\boldsymbol{F}_{\beta,k+q}^{G}|^2\,g_0(\varepsilon_{+,m',k'}^{G})\,g_0(\varepsilon_{-,n',-k'+q}^{G})$$
$$\times\Big[\frac{1}{\omega-\varepsilon_{+,m',k'}^{G}+\varepsilon_{-,n',k'+q}^{G}+\mathrm{i}\delta}$$
$$-\frac{1}{\omega+\varepsilon_{+,m',k'}^{G}-\varepsilon_{-,n',k'+q}^{G}-\mathrm{i}\delta}\Big], \quad (6.5)$$

with δ being a positive infinitesimal, where G takes the K and K' points.

6.2 Self-Energy

Formally, the effective interaction gives the self-energy for electrons in the dynamical RPA including the cutoff function as

$$\tilde{\Sigma}_\alpha^K(k, \omega) = \frac{\mathrm{i}}{2\pi A}\int\mathrm{d}\omega'\sum_{\beta,q}G_\beta^K(k+q, \omega+\omega')|\boldsymbol{F}_{\alpha,k}^{K*}\cdot\boldsymbol{F}_{\beta,k+q}^{K}|^2$$
$$\times\frac{v_{n-m}(q)}{\varepsilon_{n-m}(q, \omega')}e^{\mathrm{i}\delta\omega'}g_0(\varepsilon_{\beta,k+q}^{K}), \quad (6.6)$$

where $G_\alpha^K(k, \omega)$ is the non-interacting Green's function written as

$$G_\alpha^K(q, \omega) = \frac{1}{\omega-\varepsilon_{\alpha,q}^K+\mathrm{i}s_\alpha\delta}, \quad (6.7)$$

and $g_0(\varepsilon)$ is the cutoff function given by eq. (4.2).

The original $\boldsymbol{k}\cdot\boldsymbol{p}$ Hamiltonian has the particle-hole symmetry about $\varepsilon = 0$, and therefore, the quasi-particle energies have also the symmetry about $\varepsilon = 0$, apart from a constant energy shift common to all bands. Consequently, we can redefine the self-energy by subtracting a constant energy shift as

$$\Sigma_{\pm,n}^K(k, \pm\omega) \equiv \pm\frac{1}{2}\big[\tilde{\Sigma}_{+,n}^K(k, \omega) - \tilde{\Sigma}_{-,n}^K(k, -\omega)\big], \quad (6.8)$$

with the upper sign in the right hand side corresponding to $\Sigma_{+,n}^K(k, \omega)$ and the lower sign $\Sigma_{-,n}^K(k, -\omega)$. We then obtain the particle-hole symmetric self-energy, i.e., $\Sigma_{+,n}^K(k, \omega) = -\Sigma_{-,n}^K(k, -\omega)$.

When the frequency dependence of the dielectric function in eq. (6.6) is neglected and $\varepsilon_{n-m}(q, \omega)$ is replaced by $\varepsilon_{n-m}(q, 0)$, the self-energy is reduced to that in the screened Hartree-Fock approximation, which has been used in ref. 15. This approximation can also be called the static RPA. The Hartree-Fock approximation corresponds to putting $\varepsilon_{n-m}(q, \omega) = 1$. The comparison between the results of different approximations gives information on the effective strength of interaction effects and the validity of the approximations.

6.3 Quasi-Particle Energy

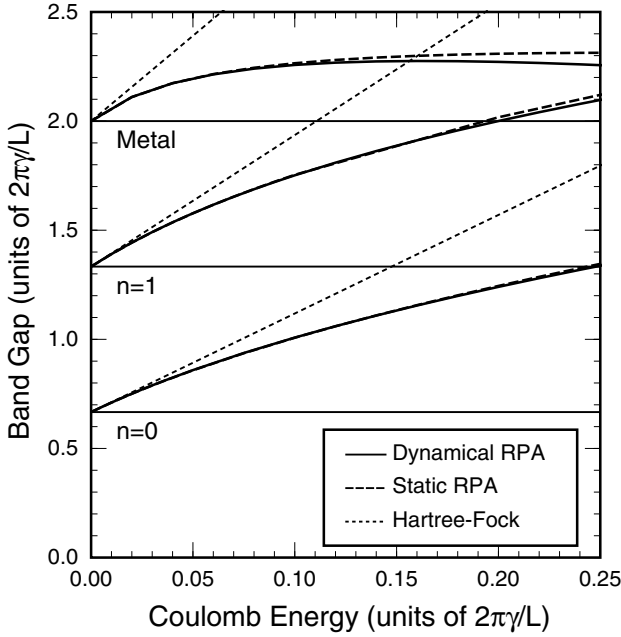The single-particle energy $E_{s,n,k}^K$ around the K point

Fig. 23 Calculated first and second band gaps in semiconducting nanotubes and first gap in metallic nanotubes. $\varepsilon_c(2\pi\gamma/L) = 5$.
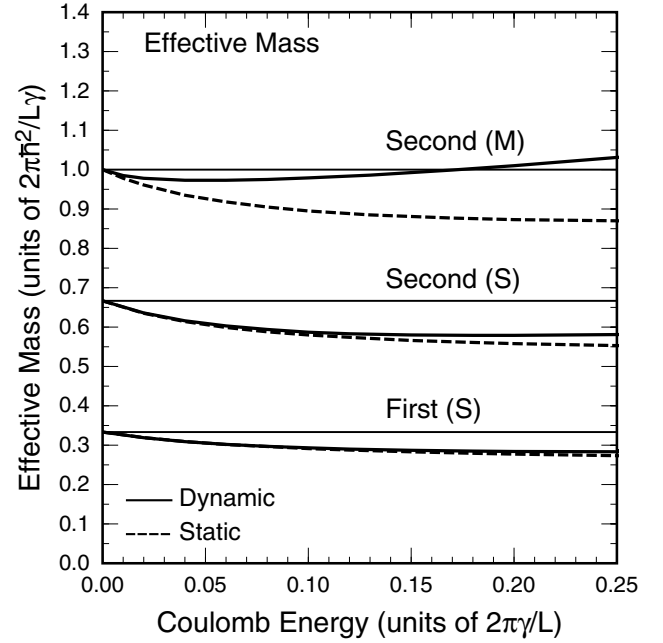

Fig. 24 Calculated effective mass of the bottom of the first and second band gaps in semiconducting nanotubes and that of the first gap in metallic nanotubes. $\varepsilon_c(2\pi\gamma/L) = 5$.

is given by

$$E_{\pm,n,k}^K = \varepsilon_{\pm,n,k}^K + \Sigma_{\pm,n}^K(k, \varepsilon_{\pm,n,k}^K). \qquad (6.9)$$

Originally, the single-particle energy is determined by the equation obtained from the above by the replacement of $\Sigma_{\pm,n}^K(k, \varepsilon_{\pm,n,k}^K)$ by $\Sigma_{\pm,n}^K(k, E_{\pm,n,k}^K)$. However, eq. (6.9) is known to give more accurate results if the self-energy is calculated only in the lowest order.[69,70] Using the above singe-particle energy, we can calculate the band gap $\varepsilon_G^K(n) = E_{+,n,0}^K - E_{-,n,0}^K$ and $\varepsilon_G^{K'}(n) = E_{+,n,0}^{K'} - E_{-,n,0}^{K'}$. The effective mass $m_{\pm,n}^{K*}$ and $m_{\pm,n}^{K'*}$ at the band edges can also be calculated.

The effective strength of the Coulomb interaction is specified by the ratio between the effective Coulomb energy $e^2/\kappa L$ and the typical kinetic energy $2\pi\gamma/L$, i.e., $(e^2/\kappa L)/(2\pi\gamma/L)$, which is independent of the circumference length L. For $\gamma_0 \sim 3$ eV and $a = 0.246$ nm, this gives $(e^2/\kappa L)/(2\pi\gamma/L) \sim 0.35/\kappa$. As long as κ is independent of L, the interaction parameter is independent of the CN diameter and therefore the band gap and also the exciton binding energy are inversely proportional to the circumference length L or the diameter $d = L/\pi$ for a fixed cutoff.

In many cases a finite result is obtained even if we let the cutoff-energy infinite at the final stage. Typical examples can be found in problems of magnetic properties as has been discussed in §4. The same is applicable to spontaneous in-plane Kekule and out-of-plane lattice-distortions, and acoustic-phonon distortion.[18,19] In the case of scattering by strong short-range scatterers such as lattice vacancies and Stone-Wales defects as will discussed in §§9 and 10, respectively, and localized eigenstates in nanotube caps,[23] results are quite sensitive to the choice of the cutoff. In such cases, the cutoff should be chosen as $\varepsilon_c \sim 3\gamma_0$ corresponding to the half of the π band width of the 2D graphite. This leads to

$\varepsilon_c(2\pi\gamma/L)^{-1} \sim (\sqrt{3}/\pi)(L/a)$.

In the present problem, the cutoff function induces a small logarithmic correction to the band gap $\propto (2\pi\gamma/L)\ln[\varepsilon_c/(2\pi\gamma/L)] \sim (2\pi\gamma/L)\ln(d/a)$ in addition to a term scaled as $2\pi\gamma/L \propto 1/d$. This means that the band gap scaled by the inverse of the diameter contains a term that shows a weak but non-negligible logarithmic dependence on the diameter.

6.4 Numerical Results

Figure 23 gives the numerical results of the first and second band gaps for a semiconducting CN and the first gap in a metallic CN versus the effective strength of the Coulomb interaction. The cutoff is chosen as $\varepsilon_c(2\pi\gamma/L) = 5$. The first band means $n = 0$ in eq. (6.9) for the K and K' point and the second $n = 1$ for the K point or $n = -1$ for the K' point. In the parameter range of the Coulomb interaction shown in the figure, the results in the static RPA are almost the same as those in the full dynamical approximation, showing that the static approximation is sufficient in this parameter range. A deviation becomes larger in metallic nanotubes, although it can still safely be neglected. Even in this weak coupling regime, the band gaps are considerably enhanced due to the Coulomb interaction. For $(e^2/\kappa L)/(2\pi\gamma/L) = 0.1$, for example, the first band gap with interaction is about 1.5 times as large as that without interaction. Furthermore, for $(e^2/\kappa L)/(2\pi\gamma/L) < 0.05$, the results in the Hartree-Fock approximation become equally valid in semiconducting tubes, but the deviation becomes more apparent in metallic tubes.

Figure 24 shows the band-edge effective mass. In semiconducting tubes the effective mass is slightly reduced by interaction and dynamic RPA and static RPA give almost identical results. In metallic nanotubes, on the other hand, the deviation is much more important,

presumably due to the presence of metallic electrons for which dynamical effects are crucial. The amount of the change in the effective mass is less than 10 % and therefore is not so important.

There exists a large difference in the interaction effect on the band gap and the effective mass. This fact shows that the interaction effects cannot be absorbed into a simple renormalization of the single band parameter γ. In the absence of interaction, the first and second band gaps become $4\pi\gamma/3L$ and $8\pi\gamma/3L$, respectively, and the corresponding effective masses are given by $2\pi\hbar^2/3L\gamma$ and $4\pi\hbar^2/3L\gamma$, respectively. Therefore, a renormalization of γ should give the result that the ratio between the first and second gaps should remain the same and that the effective mass should also be reduced by the same amount as that of the band-gap enhancement.

6.5 Tomonaga-Luttinger Liquid

A metallic CN has energy bands having a linear dispersion in the vicinity of the Fermi level and therefore is expected to be an ideal one-dimensional conductor. Interacting 1D electrons with a linear dispersion usually exhibit Tomonaga-Luttinger-liquid behavior[71,72] characterized by, for example, the absence of quasi-particle states, charge-spin separation, and interaction-dependent power laws for transport quantities. In fact, each term in perturbation series of the self-energy diverges for the linear band of $n = 0$. This divergence occurs because the momentum conservation automatically satisfies the energy conservation for a linear band. The exact low-energy excitations in such systems can be derived using the so-called bosonization method.

For armchair CN's, in particular, there have been many theoretical works in which an effective low-energy theory was formulated and explicit predictions were made on various quantities like the energy gap at the Fermi level, tunneling conductance between the CN and a metallic contact, etc.[73−77] Some experiments suggested the presence of such many-body effects.[78−81]

In ref. 80, for example, the conductance of bundles (ropes) of single-wall CN's are measured as a function of temperature and voltage. Electrical connections to nanotubes were achieved by either depositing electrode metal over the top of the tubes (end contacted) or by placing the tubes on the top of metal leads (bulk contacted). The measured differential conductance displays a power-law dependence on temperature and applied bias. The obtained different values of the power between two samples are consistent with the theoretical predictions for the Tomonaga-Luttinger liquid.[75] The power-law dependence of the density of states of the linear bands were observed directly in photoemission experiments.[81]

If we employ the same approximation scheme in metallic nanotubes, we can calculate the self-energy for the linear bands with $n = 0$, giving a gapless linear band with a renormalized velocity. In fact, although each term of perturbation expansion of the self-energy is known to exhibit a divergence, the RPA self-energy itself does not diverge because of the cancellation of a divergent polarization function. This result is in clear contradiction with the fact that only a charge-density and a spin-density excitation can exist and there are no well-defined quasi-particle excitations.

This apparent inconsistency arises from the way of determining the quasi-particle energy from the self-energy. Even in RPA, the spectral function (the imaginary part of the Green's function) exhibits double sharp peaks in a system with only metallic linear bands.[17] This peak splitting, into charge-density and spin-density excitations presumably, is qualitatively in agreement with that of the spectral function for a Tomonaga-Luttinger liquid reported in refs. 82 and 83. For the parabolic bands both in semiconducting and metallic CN's, no singular behavior appears in the polarization function and in the perturbation expansion of the self-energy and therefore quasi-particle states are expected to give a good picture of their low-energy excitations.

6.6 Exciton

It is well known that the exciton binding energy becomes infinite in an ideal one-dimensional electron-hole system.[84,85] This means that the exciton effect can be quite important and modify the absorption spectra drastically in CN's. Exciton energy levels and corresponding optical spectra have been calculated in the conventional screened Hartree-Fock approximation within a $\boldsymbol{k\cdot p}$ scheme,[15] in which slight insufficiencies are present for the absolute values of the band gaps due to a small cutoff.[16]

The exciton states are described by the many-body wave function

$$|u\rangle = \sum_n \sum_k \psi_n(k) c^\dagger_{+,n,k} c_{-,n,k} |g\rangle, \qquad (6.10)$$

where $|g\rangle$ is the ground-state wave function, and $c_{s,n,k}$ and $c^\dagger_{s,n,k}$ are the annihilation and creation operator, respectively. The equation of motion for $\psi_n(k)$ is written as

$$\varepsilon_u \, \psi_n(k) = \left(2\gamma\sqrt{\kappa_{\nu\varphi}(n)^2+k^2}+\Delta\varepsilon_{nk}\right)\psi_n(k)$$
$$-\sum_m \int \frac{dq}{2\pi}\frac{2e^2}{\kappa\,\varepsilon_{|n-m|}(q)}I_{|n-m|}\!\left(\frac{L|q|}{2\pi}\right)K_{|n-m|}\!\left(\frac{L|q|}{2\pi}\right)$$
$$\times \frac{1}{2}\left(1+\frac{\kappa_{\nu\varphi}(n)\kappa_{\nu\varphi}(m)+k(k+q)}{\sqrt{\kappa_{\nu\varphi}(n)^2+k^2}\sqrt{\kappa_{\nu\varphi}(m)^2+(k+q)^2}}\right)\psi_m(k+q),$$
$$(6.11)$$

where, $\Delta\varepsilon_{nk}$ is the difference of the self-energy of the conduction and valence band. In the screened Hartree-Fock approximation, it is given by

$$\Delta\varepsilon_{nk} = \sum_m\sum_q \frac{2e^2}{A\kappa\,\varepsilon_{|n-m|}(q)}I_{|n-m|}\!\left(\frac{L|q|}{2\pi}\right)K_{|n-m|}\!\left(\frac{L|q|}{2\pi}\right)$$
$$\times \frac{\kappa_{\nu\varphi}(n)\kappa_{\nu\varphi}(m)+k(k+q)}{\sqrt{\kappa_{\nu\varphi}(n)^2+k^2}\sqrt{\kappa_{\nu\varphi}(m)^2+(k+q)^2}}$$
$$\times g_0\!\left(\gamma\sqrt{\kappa_{\nu\varphi}(m)^2+(k+q)^2}\right). \qquad (6.12)$$

The optical absorption is described by the dynamical conductivity $\sigma_{yy}(\omega)$. The dynamical conductivity for the K point is given by

$$\sigma_{yy}(\omega) = \frac{\hbar e^2}{AL}\sum_u \frac{-2i\hbar\omega|\langle u|v_y|g\rangle|^2}{\varepsilon_u[\varepsilon_u^2-(\hbar\omega)^2-2i\hbar^2\omega/\tau]}, \qquad (6.13)$$

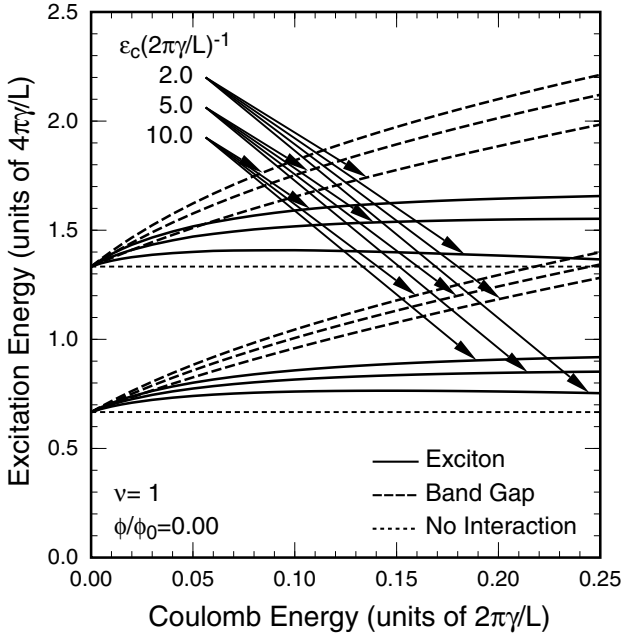where broadening described by a phenomenological re-

Fig. 25 Calculated band gaps (dashed lines) and exciton absorption energies (solid lines) of the first and second bands as a function of the effective Coulomb energy $(e^2/\kappa L)(2\pi\gamma/L)$ in the absence of flux for various cut-off energies.
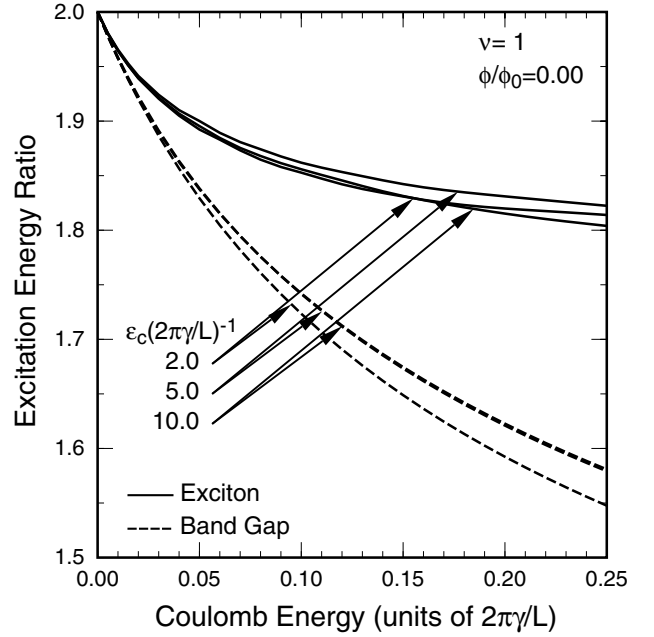

Fig. 26 The ratio of the absorption energies (solid lines) and band gaps (dashed lines) between the first and second bands as a function of the effective Coulomb energy.
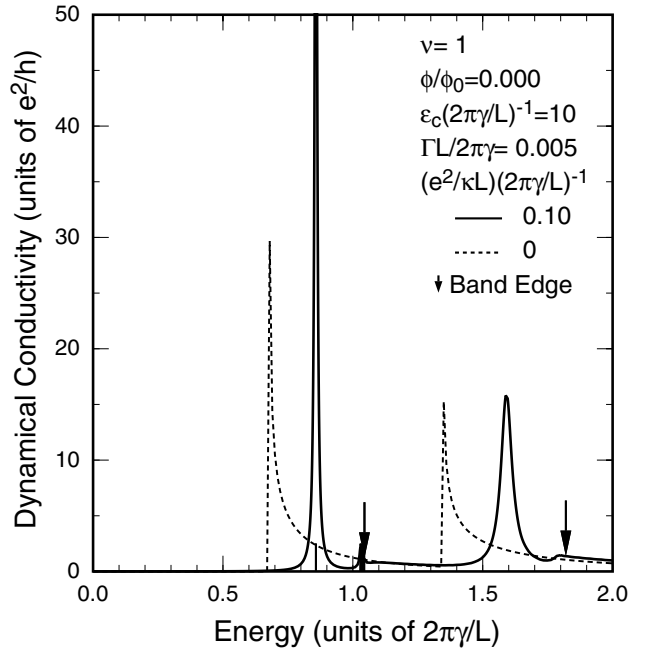

Fig. 27 Calculated optical absorption spectra of a semi-conducting nanotube in the presence of AB magnetic flux. The solid lines represent spectra in the presence of interaction $(e^2/\kappa L)(2\pi\gamma/L)^{-1}=0.1$ and the dotted lines those in the absence of interaction.

laxation time τ has been introduced and

$$\langle u|v_y|g\rangle = i\frac{\gamma}{\hbar}\sum_n\sum_k\frac{\kappa_{\nu\varphi}(n)}{\sqrt{\kappa_{\nu\varphi}(n)^2+k^2}}\psi_n(k)^*. \quad (6.14)$$

As can be understood in eq. (6.13), the intensity of the absorption is proportional to $|\langle u|v_y|g\rangle|^2/\varepsilon_u$. Following a convention in free-electron systems, we shall introduce a dimensionless oscillator strength

$$f_u = 2m^*\frac{|\langle u|v_y|g\rangle|^2}{\varepsilon_u}, \quad (6.15)$$

where m^* is chosen as the effective mass of the bottom of the lowest conduction band, i.e., $m^* = 2\pi\hbar^2/3\gamma L$. We have $f_u \sim 1$ for the lowest exciton. In free-electron systems the oscillator strength satisfies the f sum rule, $\sum_u f_u = 1$. In the present case, however, this sum rule is not satisfied because the electron motion is governed by Weyl's equation for massless neutrino.

Figure 25 shows the band gaps and the lowest exciton absorption energies associated with fundamental and second gaps as a function of the effective Coulomb energy $(e^2/\kappa L)(2\pi\gamma/L)^{-1}$ in the absence of magnetic flux.[16] A dominant feature is the enhancement of the band gaps with the increase of the interaction strength. The binding energy of excitons increases with the interaction but remains smaller than the band-gap enhancement. As a result, the absorption energies become higher than the band gap without interaction. Further, interaction effects on the band gap and the exciton binding energy are larger for the second band than for the first band.

Figure 26 shows the ratio of the excitation energies for the first and second gap as a function of the effective Coulomb energy. The ratio of the absorption energies decreases from 2 to ~ 1.8 with the increase of the Coulomb energy, while that of the band gaps decreases much more

strongly. It is noteworthy that the ratio is almost independent of the cutoff parameter. This ratio ~ 1.8 except in the case of small interaction parameter explains the existing experiments quite well.

Figure 27 shows the calculated absorption spectrum for $\varepsilon_c(2\pi\gamma/L)^{-1}=10$ and $(e^2/\kappa L)(2\pi\gamma/L)^{-1}=0.1$. The energy levels of excitons are denoted by vertical straight lines and the band gaps are denoted by downward arrows. Most of the optical intensity is transferred to the exciton bound states and the intensity of band-to-band transitions is almost absent. This behavior is a direct
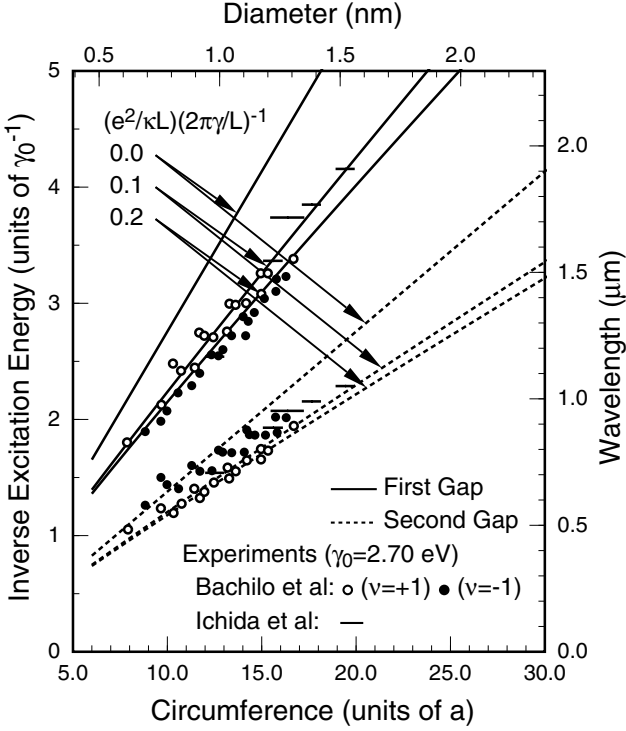
Fig. 28   The inverse of the absorption energies obtained by an interpolation as a function of the circumference and the diameter. The experimental results (Ichida et al.[88,89] and Bachilo et al.[55]) are plotted using $\gamma_0 = 2.7$ eV.

consequence of the one-dimensional nature of nanotubes and is similar to that in a model 1D system.[86]

Optical absorption spectra of thin film samples of single-wall nanotubes were observed.[87] Careful comparison of the observed spectrum with calculated in a simple tight-binding model based on measured distribution of diameter suggested the importance of excitonic effects.[88,89] Quite recently, optical absorption and photoluminescence of individual nanotubes were observed.[55,56,90,91] Splitting of the absorption and emission peaks due to AB effect associated with magnetic flux passing through the cross section was observed also.[46] The AB splitting due to magnetic flux and the shift due to strain were shown to be enhanced slight by electron-electron interactions.[16]

In the $\boldsymbol{k}\cdot\boldsymbol{p}$ scheme the only remaining parameter is γ or γ_0 related to each other through $\gamma = \sqrt{3}a\gamma_0/2$. Figure 28 shows the comparison of the calculated absorption energies with some of existing experiments[55,88,89] for $\gamma_0 = 2.7$ eV. It is concluded that the overall dependence on the circumference and the diameter is in good agreement with the experiments. Experimental results depend on the chirality as well as the diameter, in particular, for thin nanotubes. In thin nanotubes various higher-order effects such as trigonal warping and finite curvature as discussed in §3 manifest themselves.

In particular, the energy shifts of the first and second gap due to higher-order effects are opposite and also change the signature between semiconducting nanotubes with $\nu = +1$ and -1. This family behavior has been used extensively for the determination of the structure of individual single-wall tubes by the combination of absorption due to transitions corresponding to the second gap

and photoluminescence due to transitions corresponding to the first gap.[55,56,91,92] Because of strong effects of excitons and electron-electron interaction, accurate estimation of these effects is quite difficult even in the $\boldsymbol{k}\cdot\boldsymbol{p}$ scheme. In very thin nanotubes, further, mixing between π and σ bands, etc., which is likely to cause anisotropy inherent in the formation of a cylindrical structure, should also be considered.[5,38,39] An extension of a tight-binding model was proposed such that the family effect can be explained partly.[93]

Quasi-particle spectra of nanotubes were calculated using a first-principles GW method,[94] and calculations were performed also for optical absorption spectra with the inclusion of excitonic final state interactions.[95,96] These calculations are limited to nanotubes with a very small diameter including those grown in a special method.[97] There have been some reports on a phenomenological description of excitons in nanotubes also.[98,99]

§7. Absence of Backward Scattering

7.1 Effective Hamiltonian

In the following, we shall derive an effective Hamiltonian based on the nearest-neighbor tight-binding model considered in §2.[24] In the presence of impurity potential, the equation of motion (2.4) is replaced by

$$[\varepsilon - u_A(\boldsymbol{R}_A)]\psi_A(\boldsymbol{R}_A) = -\gamma_0 \sum_l \psi_B(\boldsymbol{R}_A - \vec{\tau}_l),$$
$$[\varepsilon - u_B(\boldsymbol{R}_B)]\psi_B(\boldsymbol{R}_B) = -\gamma_0 \sum_l \psi_A(\boldsymbol{R}_B + \vec{\tau}_l), \quad (7.1)$$

where $u_A(\boldsymbol{R}_A)$ and $u_B(\boldsymbol{R}_B)$ represent local site energy. When being multiplied by $g(\boldsymbol{r} - \boldsymbol{R}_A)\boldsymbol{a}(\boldsymbol{R}_A)$ and summed over $\boldsymbol{R}_A$, the term containing this impurity potential $u_A(\boldsymbol{R}_A)$ becomes

$$\sum_{\boldsymbol{R}_A} g(\boldsymbol{r} - \boldsymbol{R}_A)u_A(\boldsymbol{R}_A)\boldsymbol{a}(\boldsymbol{R}_A)\boldsymbol{a}(\boldsymbol{R}_A)^\dagger \boldsymbol{F}_A(\boldsymbol{r})$$
$$= \begin{pmatrix} u_A(\boldsymbol{r}) & e^{i\eta}u'_A(\boldsymbol{r}) \\ e^{-i\eta}u'_A(\boldsymbol{r})^* & u_A(\boldsymbol{r}) \end{pmatrix} \boldsymbol{F}_A(\boldsymbol{r}), \quad (7.2)$$

with

$$u_A(\boldsymbol{r}) = \sum_{\boldsymbol{R}_A} g(\boldsymbol{r} - \boldsymbol{R}_A)u_A(\boldsymbol{R}_A),$$
$$u'_A(\boldsymbol{r}) = \sum_{\boldsymbol{R}_A} g(\boldsymbol{r} - \boldsymbol{R}_A)e^{i(\boldsymbol{K}' - \boldsymbol{K})\cdot\boldsymbol{R}_A}u_A(\boldsymbol{R}_A). \quad (7.3)$$

Similarly, the term containing this impurity potential $u_B(\boldsymbol{R}_B)$ becomes

$$\sum_{\boldsymbol{R}_B} g(\boldsymbol{r} - \boldsymbol{R}_B)u_B(\boldsymbol{R}_B)\boldsymbol{b}(\boldsymbol{R}_B)\boldsymbol{b}(\boldsymbol{R}_B)^\dagger \boldsymbol{F}_B(\boldsymbol{r})$$
$$= \begin{pmatrix} u_B(\boldsymbol{r}) & -\omega e^{-i\eta}u'_B(\boldsymbol{r}) \\ -\omega^{-1}e^{i\eta}u'_B(\boldsymbol{r})^* & u_B(\boldsymbol{r}) \end{pmatrix} \boldsymbol{F}_B(\boldsymbol{r}), \quad (7.4)$$

with

$$u_B(\boldsymbol{r}) = \sum_{\boldsymbol{R}_B} g(\boldsymbol{r} - \boldsymbol{R}_B)u_B(\boldsymbol{R}_B),$$
$$u'_B(\boldsymbol{r}) = \sum_{\boldsymbol{R}_B} g(\boldsymbol{r} - \boldsymbol{R}_B)e^{i(\boldsymbol{K}' - \boldsymbol{K})\cdot\boldsymbol{R}_B}u_B(\boldsymbol{R}_B). \quad (7.5)$$

Therefore, the 4×4 effective potential of an impurity is
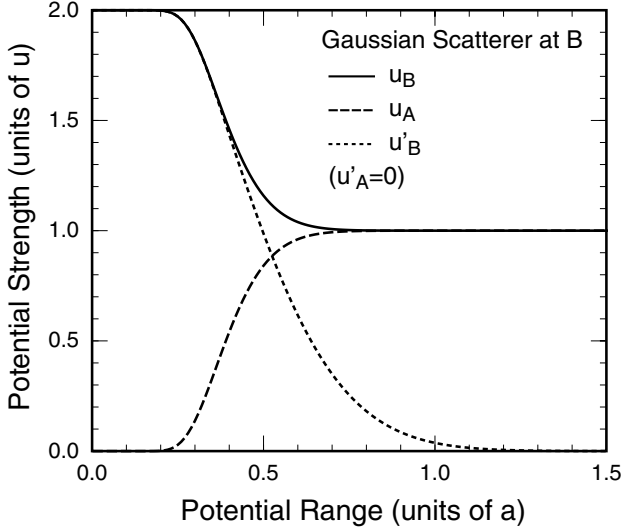
Fig. 29 Calculated effective strength of the potential for a model Gaussian impurity at a B site.

Fig. 30 Calculated effective scattering matrix elements versus the potential range at $\varepsilon = 0$ in the absence of a magnetic field.

written as

$$
V = \begin{pmatrix}
u_A(\boldsymbol{r}) & 0 & e^{i\eta}u'_A(\boldsymbol{r}) & 0 \\
0 & u_B(\boldsymbol{r}) & 0 & -\omega^{-1}e^{-i\eta}u'_B(\boldsymbol{r}) \\
e^{-i\eta}u'_A(\boldsymbol{r})^* & 0 & u_A(\boldsymbol{r}) & 0 \\
0 & -\omega e^{i\eta}u'_B(\boldsymbol{r})^* & 0 & u_B(\boldsymbol{r})
\end{pmatrix}.
\tag{7.6}
$$

When the potential range is much shorter than the circumference L and the potential at each site is sufficiently weak, we have

$$
\begin{aligned}
u_A(\boldsymbol{r}) &= u_A\delta(\boldsymbol{r}-\boldsymbol{r}_A), \\
u_B(\boldsymbol{r}) &= u_B\delta(\boldsymbol{r}-\boldsymbol{r}_B), \\
u'_A(\boldsymbol{r}) &= u'_A\delta(\boldsymbol{r}-\boldsymbol{r}_A), \\
u'_B(\boldsymbol{r}) &= u'_B\delta(\boldsymbol{r}-\boldsymbol{r}_B),
\end{aligned}
\tag{7.7}
$$

with

$$
\begin{aligned}
u_A &= \Omega_0 \sum_{\boldsymbol{R}_A} u_A(\boldsymbol{R}_A), \\
u_B &= \Omega_0 \sum_{\boldsymbol{R}_B} u_B(\boldsymbol{R}_B),
\end{aligned}
\tag{7.8}
$$

and

$$
\begin{aligned}
u'_A &= \Omega_0 \sum_{\boldsymbol{R}_A} e^{i(\boldsymbol{K}'-\boldsymbol{K})\cdot\boldsymbol{R}_A} u_A(\boldsymbol{R}_A), \\
u'_B &= \Omega_0 \sum_{\boldsymbol{R}_B} e^{i(\boldsymbol{K}'-\boldsymbol{K})\cdot\boldsymbol{R}_B} u_B(\boldsymbol{R}_B),
\end{aligned}
\tag{7.9}
$$

where $\boldsymbol{r}_A$ and $\boldsymbol{r}_B$ are the center-of-mass position of the effective impurity potential and Ω_0 is the area of a unit cell defined by eq. (2.1). The integrated intensities u_A, etc. have been obtained by the $\boldsymbol{r}$ integral of $u_A(\boldsymbol{r})$, etc. given by eqs. (7.3)–(7.5). This short-range potential becomes invalid when the site potential is as strong as the effective band width of 2D graphite as will be shown in the end of §9.

7.2 Ideal Conductance

In the vicinity of $\varepsilon = 0$, we have two right-going channels $K+$ and $K'+$, and two left-going channels $K-$
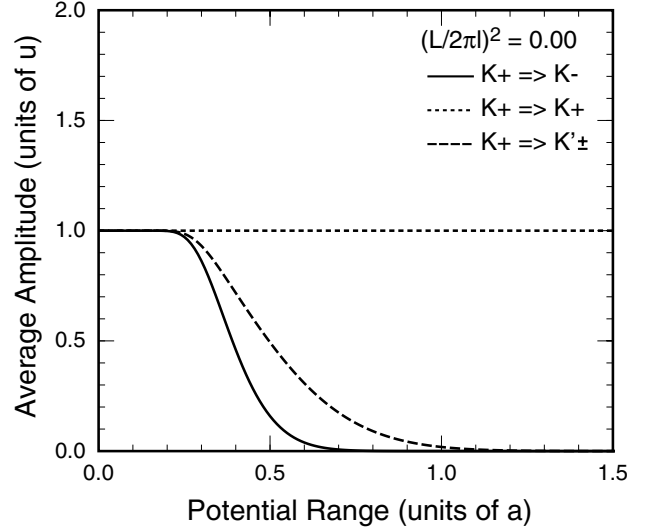
and $K'-$. The matrix elements are calculated as[24]

$$
\begin{aligned}
V_{K\pm K+} &= V_{K'\pm K'+} = \frac{1}{2}(\pm u_A + u_B), \\
V_{K\pm K'+} &= V_{K'\pm K+}^* = \frac{1}{2}(\mp e^{i\eta}u'_A - \omega^{-1}e^{-i\eta}u'_B).
\end{aligned}
\tag{7.10}
$$

When the impurity potential has a range larger than the lattice constant, we have $u_A = u_B$ and both u'_A and u'_B become much smaller and can be neglected because of the phase factor $e^{i(\boldsymbol{K}'-\boldsymbol{K})\cdot\boldsymbol{R}_A}$ and $e^{i(\boldsymbol{K}'-\boldsymbol{K})\cdot\boldsymbol{R}_B}$.

Figure 29 gives an example of calculated effective potential u_A, u_B, and u'_B as a function of d/a for a Gaussian potential $(u/\pi d^2)\exp(-r^2/d^2)$ located at a B site and having the integrated intensity u. Because of the symmetry corresponding to the 120° rotation around a lattice point, we have $u'_A = 0$ independent of d/a. When the range is sufficiently small, u_B and u'_B stay close to $2u$ because the potential is localized only at the impurity B site. With the increase of d the potential becomes nonzero at neighboring A sites and u_A starts to increase and at the same time both u_B and u'_B decrease. The diagonal elements u_A and u_B rapidly approach u and the off-diagonal element u'_B vanishes.

Figure 30 shows calculated averaged scattering amplitude, given by $AL\sqrt{\langle|V_{K\pm K+}|^2\rangle}$ and $AL\sqrt{\langle|V_{K'\pm K+}|^2\rangle}$ where $\langle|V_{K\pm K+}|^2\rangle$ and $\langle|V_{K'\pm K+}|^2\rangle$ are the squared matrix elements averaged over impurity position, as a function of d in the absence of a magnetic field. The backward scattering probability decreases rapidly with d and becomes exponentially small for $d/a \gg 1$. The same is true of the inter-valley scattering although the dependence is slightly weaker because of the slower decrease of u'_B shown in Fig. 29.

This absence of the backward scattering for long-range scatterers disappears in the presence of magnetic fields. In the presence of a magnetic field perpendicular to the axis, the matrix elements for an impurity located
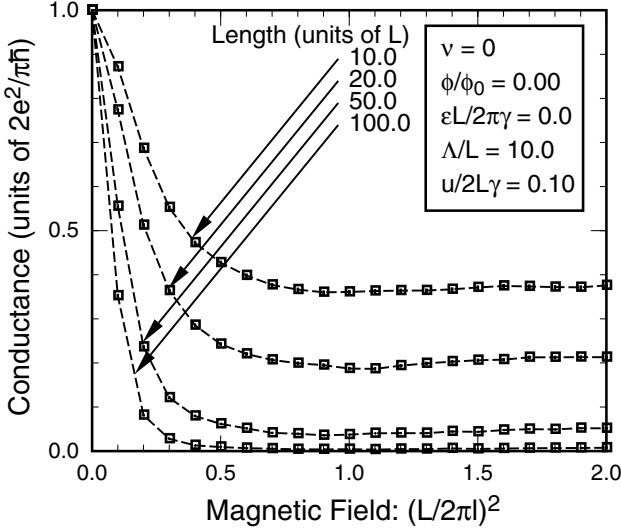
Fig. 31 Calculated conductance of finite-length nano-
tubes at $\varepsilon = 0$ as a function of the effective strength of
a magnetic field $(L/2\pi l)^2$ in the case that the effective
mean free path Λ is much larger than the circumfer-
ence L. The conductance is always given by the value
in the absence of impurities at $B = 0$.

at $\boldsymbol{r} = \boldsymbol{r}_0$ are calculated as

$$V_{K\pm K+} = \frac{1}{2A}[\pm u_A F_-(x_0)^2 + u_B F_+(x_0)^2],$$

$$V_{K'\pm K+} = \frac{1}{2A}[\mp e^{-i\eta} u_A'^* - \omega e^{i\eta} u_B'^*]F_+(x_0)F_-(x_0),$$

$$V_{K'\pm K'+} = \frac{1}{2A}[\pm u_A F_+(x_0)^2 + u_B F_-(x_0)^2],$$

$$V_{K\pm K'+} = \frac{1}{2A}[\mp e^{i\eta} u_A' - \omega^{-1} e^{-i\eta} u_B']F_+(x_0)F_-(x_0),$$

$$\text{(7.11)}$$

where the wave functions in a magnetic field are de-
fined in eq. (3.39). In high magnetic fields, the inter-
valley scattering is reduced considerably because of the
reduction in the overlap of the wavefunction, but the
intra-valley backward scattering remains nonzero be-
cause $|F_+(x_0)| \neq |F_-(x_0)|$.

It is straightforward to calculate a scattering or S
matrix for an impurity given by eq. (7.7) and a conduc-
tance of a finite-length nanotube containing many impu-
rities, combining S matrices.[49,24] Figure 31 shows some
examples of calculated conductance at $\varepsilon = 0$ in the case
that the impurity potential has a range larger than the
lattice constant, i.e., $u_A = u_B = u$ and $u_A' = u_B' = 0$. The
conductance in the absence of a magnetic field is always
quantized into $2e^2/\pi\hbar$ because of the complete absence
of backward scattering. With the increase of the mag-
netic field the conductance is reduced drastically and the
amount of the reduction becomes larger with the increase
of the length.

7.3 Neutrino Analogy

Unless the range of scattering potential is smaller
than the lattice constant, the Schrödinger equation for
the K and K' points are decoupled and given for the K
point by

$$(\mathcal{H}_0 + V)\boldsymbol{F}^K(\boldsymbol{r}) = \varepsilon \boldsymbol{F}^K(\boldsymbol{r}), \qquad \text{(7.12)}$$

with $\mathcal{H}_0 = \gamma(\vec{\sigma} \cdot \hat{\boldsymbol{k}})$ and

$$V = \begin{pmatrix} V(\boldsymbol{r}) & 0 \\ 0 & V(\boldsymbol{r}) \end{pmatrix}. \qquad \text{(7.13)}$$

The equation for the K' point can be obtained by replac-
ing σ_y by $-\sigma_y$. For such systems it can be proved that
the Born series for back-scattering vanish identically.[24]
This can be ascribed to a spinor-type property of the
wave function under a rotation in the wave vector
space.[100] In fact, an electron in the nanotube can be re-
garded as a neutrino, which has a helicity, i.e., its spin is
quantized into the direction of its wave vector, and there-
fore each scattering corresponds to a spin rotation. The
matrix element for scattering is separable into a product
of that of the impurity potential and a spin rotation.

A backward scattering corresponds to a spin rota-
tion by $+(2j+1)\pi$ with j being an appropriate integer
and its time reversal process corresponds to a spin ro-
tation by $-(2j+1)\pi$. The spinor wave function after a
rotation by $-(2j+1)\pi$ has a signature opposite to that
after a rotation by $+(2j+1)\pi$ because of the property of
a spin-rotation operator discussed in §2.4. On the other
hand, the matrix element of the time reversal process
has an identical spatial part. As a result, the sum of the
matrix elements of a back-scattering process and its time
reversal process vanishes due to the complete cancella-
tion, leading to the absence of backward scattering.[100]

In the presence of a magnetic field, the time reversal
symmetry is destroyed and backward scattering becomes
nonzero. In the band $n = 0$ of semiconducting nanotubes
with $\nu = \pm 1$, the right-going state of the K point has
the wave vector $\boldsymbol{k}_+ = (-2\pi\nu/3L, |k|)$ and the left-going
state $\boldsymbol{k}_- = (-2\pi\nu/3L, -|k|)$ with $\pm|k|$ being the wave
vector along the axis direction. Therefore, the backscat-
tering $\boldsymbol{k}_+ \to \boldsymbol{k}_-$ does not correspond to the spin rotation
by $+(2j+1)\pi$ or $-(2j+1)\pi$. As a result backscatter-
ing does not vanish and a nonzero resistance appears in
semiconducting nanotubes even in the absence of a mag-
netic field. Further discussions will be given in §7.5 in
relation to the time reversal symmetry.

A similar phase change of the back scattering pro-
cess is the origin of the so-called anti-localization effect in
systems with strong spin-orbit scattering.[101] In the ab-
sence of spin-orbit interactions, the scattering amplitude
of each process and that of corresponding time-reversal
process are equal and therefore their constructive inter-
ference leads to an enhancement in the amplitude of
back scattering processes. This gives rise to the so-called
quantum correction to the conductivity in the weak lo-
calization theory. In the presence of a strong spin-orbit
scattering, however, scattering from an impurity causes
a spin rotation and resulting phase change of the wave
function leads to a destructive interference. As a result
the quantum correction has a sign opposite to that in
the absence of a spin-orbit scattering.

7.4 Experiments

There have been some reports on experimental
study of transport in CN ropes.[102,103] However, be-
cause of the presence of large contact resistance be-
tween a nanotube and metallic electrode, the measure-
ment of the conductance of a single single-wall nano-

tube itself is quite difficult and has not been so successful. However, from measurements of single electron tunneling due to a Coulomb blockade and charging effect, important information can be obtained on the effective mean free path and the amount of backward scattering in nanotubes.[104−106] Discrete quantized energy levels were measured for a nanotube with ∼ 3 μm length, for example, showing that the electron wave is coherent and extended over the whole length.[104]

It was shown further that the Coulomb oscillation in semiconducting nanotubes is quite irregular and can be explained only if nanotubes are divided into many separate spatial regions in contrast to that in metallic nanotubes.[107] This behavior is consistent with the presence of considerable amount of backward scattering leading to a strong localization of the wave function in semiconducting tubes. In metallic nanotubes, the wave function is extended throughout the whole region of a nanotube because of the absence of backward scattering. The voltage distribution in a metallic nanotube with current was measured by electrostatic force microscopy, which showed clearly that there is essentially no voltage drop in the nanotube.[108]

Single-wall nanotubes usually exhibit large charging effects due to non-ideal contacts. Contacts problems were investigated theoretically in various models and an ideal contact was suggested to be possible under certain conditions.[109−113] Almost ideal contacts were realized and a Fabry-Perot type oscillation due to reflection by contacts was claimed to be observed.[114]

7.5 Perfectly Conducting Channel

The Fermi energy of CN is known to be controlled by a gate voltage for a wide range.[105,115−121] When the Fermi level moves away from the energy range where only linear bands are present, interband scattering appears because of the presence of several bands at the Fermi level. Even in such cases there exists a perfectly conducting channel which transmits through the system without being scattered back.[25]

Let $r_{\bar{\beta}\alpha}$ be the reflection coefficient from a state with wave vector $\boldsymbol{k}_\alpha$ to a state with $\boldsymbol{k}_{\bar{\beta}} \equiv -\boldsymbol{k}_\beta$ in a 2D graphite sheet. Here, $\bar{\beta}$ stands for the state with wave vector opposite to β. Only difference arising in nanotubes is discretization of the wave vector in the circumference k_x direction. We shall confine ourselves to states in the vicinity of the K point, but the extension to states near a K' point is straightforward.

Corresponding to the 2×2 equation (7.12) containing Pauli's spin matrices, a time reversal operation T can be defined as

$$\psi^T = K\psi^*, \qquad (7.14)$$

where the wave function is denoted by ψ for convenience instead of $\boldsymbol{F}_{sk}^K$ defined by eq. (2.27) with eq. (2.28), ψ^* represents the complex conjugate of ψ, and K is an antisymmetric unitary matrix

$$K = -\mathrm{i}\sigma_y = \begin{pmatrix} 0 & -1 \\ 1 & 0 \end{pmatrix}. \qquad (7.15)$$

The corresponding operation for an operator P is given

by[122]

$$P^T = K\,{}^tPK^{-1}, \qquad (7.16)$$

where ${}^tP$ is the transpose of P. Note that

$$K^2 = -1. \qquad (7.17)$$

For this definition, we have the identity

$$(\psi_1, P\psi_2) = (\psi_2^T, P^T\psi_1^T), \qquad (7.18)$$

where (ψ, ψ') stands for the inner product of ψ and ψ'.

It is easy to show that the Hamiltonian $\mathcal{H}_0$ in the absence of scatterers is invariant under the time reversal operation. Further, the potential is given by a real and diagonal matrix and therefore invariant also. Consequently the T matrix is also invariant under time reversal. Under the time reversal operation, the wave functions are transformed as

$$\psi_{s\alpha}^T = -s\,u_\alpha^*\psi_{s\bar{\alpha}}, \quad \psi_{s\bar{\alpha}}^T = s\,u_\alpha^*\psi_{s\alpha}, \qquad (7.19)$$

with

$$u_\alpha = \mathrm{sgn}[-\theta(\boldsymbol{k}_\alpha)]\mathrm{e}^{\mathrm{i}\phi_s(\boldsymbol{k}_\alpha)+\mathrm{i}\phi_s(\boldsymbol{k}_{\bar{\alpha}})}, \qquad (7.20)$$

where $\mathrm{sgn}(t)$ denotes the signature of t. This shows that $\psi_{s\alpha}$ and $\psi_{s\bar{\alpha}}$ are indeed connected to each other through the time reversal. With the use of eq. (7.19), we have

$$(\psi_{s\alpha}^T)^T = -s\,u_\alpha\psi_{s\bar{\alpha}}^T = -\psi_{s\alpha}, \qquad (7.21)$$

which agrees with the result obtained directly using eq. (7.17), i.e.,

$$(\psi_{s\alpha}^T)^T = K^2\psi_{s\alpha} = -\psi_{s\alpha}. \qquad (7.22)$$

Introduce a T matrix defined by

$$T = V + V\frac{1}{\varepsilon - \mathcal{H}_0 + \mathrm{i}0}V + V\frac{1}{\varepsilon - \mathcal{H}_0 + \mathrm{i}0}V\frac{1}{\varepsilon - \mathcal{H}_0 + \mathrm{i}0}V + \cdots. \qquad (7.23)$$

The scattering matrix S for scattering from channel α to β is written as

$$S_{\alpha\beta} = \delta_{\alpha\beta} - \mathrm{i}\frac{A}{\hbar\sqrt{v_\alpha v_\beta}}T_{\alpha\beta}, \qquad (7.24)$$

where v_α and v_β are the velocity of channels α and β, respectively.

Because of the time-reversal invariance of T matrix, we have

$$T_{\bar{\beta}\alpha} = (\psi_{\bar{\beta}}, T\psi_\alpha) = (\psi_\alpha^T, T\psi_{\bar{\beta}}^T), \qquad (7.25)$$

which gives

$$T_{\bar{\beta}\alpha} = -u_\alpha T_{\bar{\alpha}\beta}\,u_\beta^*. \qquad (7.26)$$

The negative sign in the right hand side appears because apart from a trivial phase factor ψ_α^T can be replaced by $\psi_{\bar{\alpha}}$ while $\psi_{\bar{\beta}}^T$ should be replaced by $-\psi_\beta$.

Therefore, apart from a trivial phase factor arising from the choice in the phase of the wave function, the reflection coefficients satisfy the symmetry relation:

$$r_{\bar{\beta}\alpha} = -r_{\bar{\alpha}\beta}. \qquad (7.27)$$

This leads to the absence of backward scattering $r_{\bar{\alpha}\alpha} = -r_{\bar{\alpha}\alpha} = 0$ in the single-channel case as discussed in §7.3. Define the reflection matrix r by $[r]_{\alpha\beta} = r_{\bar{\alpha}\beta}$. Then, we have $r = -\,{}^tr$. In general we have $\det{}^tP = \det P$ for any matrix P. In metallic nanotubes, the number of traveling

modes n_c is always given by an odd integer and therefore $\det(-r) = -\det(r)$, leading to $\det(r) = 0$.

By definition, $r_{\bar{\beta}\alpha}$ represents the amplitude of a reflective wave $\bar{\beta}$ with wave function $\psi_{\bar{\beta}}(\mathbf{r})$ corresponding to an in-coming wave α with wave function $\psi_\alpha(\mathbf{r})$. The vanishing determinant of r shows that there exists at least one nontrivial solution for the equation

$$\sum_{\alpha=1}^{n_c} r_{\bar{\beta}\alpha} a_\alpha = 0. \qquad (7.28)$$

Then, there is no reflected wave for the incident wave $\sum_\alpha a_\alpha \psi_\alpha(\mathbf{r})$, which therefore becomes a perfectly conducting channel.

Figure 32 shows some examples of the length dependence of the calculated conductance in the presence of scatterers for different values of the energy. There are three and five traveling modes for $1 < \varepsilon(2\pi\gamma/L)^{-1} < 2$ and $2 < \varepsilon(2\pi\gamma/L)^{-1} < 3$, respectively. The upward arrows show the mean free path of traveling modes obtained by solving the Boltzmann transport equation (see §7.6). Although detailed behavior varies as a function of energy relative to the band edge, we can safely conclude that the relevant length scale over which the conductance decreases down to the ideal single-channel result is given by the mean free path.

The "time-reversal" symmetry introduced above is not the real time reversal-symmetry present in 2D graphite. In fact, in semiconducting tubes, the present symmetry is destroyed by the fictitious flux $\phi = -(\nu/3)\phi_0$ for the K point arising from the boundary conditions and giving rise to a nonzero gap as discussed in §3.3. As a result, backscattering is present and there is no perfectly conducting channel in semiconducting nanotubes. The real time-reversal symmetry changes the wave function at the K point into that at the K' point because they are mutually complex conjugate and therefore cannot give any information on scattering within the K point or the K' point.

7.6 Inelastic Scattering

The transport may be discussed using a conventional Boltzmann equation. The transport equation in a CN is the same as that in quantum wires[123] and written as

$$-\frac{e}{\hbar} E \frac{\partial g_{mk}}{\partial k} = \sum_{m'k'} W_{m'k'mk}(g_{m'k'} - g_{mk}), \qquad (7.29)$$

where E is the electric field in the axis direction and g_{mk} is the distribution function for states specified by the wave vector k in the y direction and the band index m. We shall consider the case with $\varepsilon > 0$ and omit the band index s for simplicity in the following. The scattering probability is given in the Born approximation by

$$W_{m'k'mk} = \frac{2\pi}{\hbar} \langle |V_{m'k'mk}|^2 \rangle \delta(\varepsilon_{m'k'} - \varepsilon_{mk}), \qquad (7.30)$$

where $V_{m'k'mk}$ is the scattering amplitude.

The transport equation can be solved to the lowest order in the electric field as

$$g_{mk} = f(\varepsilon_{mk}) + eEv_{mk}\tau_{mk}\frac{\partial f}{\partial \varepsilon}(\varepsilon_{mk}), \qquad (7.31)$$

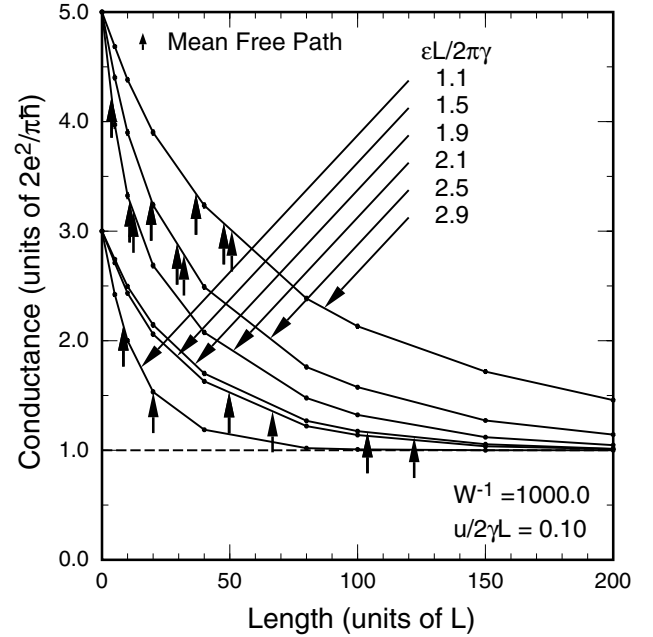where $f(\varepsilon)$ is the Fermi distribution function, τ_{mk} is the

Fig. 32　An example of the length dependence of the calculated conductance. The arrows show the mean free path of traveling modes obtained by solving the Boltzmann transport equation. For lower three curves there are three bands with $n = 0$ and ± 1 and for upper three curves there are five bands with $n = 0$, ± 1, and ± 2. The mean free path is same for bands with same $|n|$ and decreases with the increase of $|n|$. The scattering strength is characterized by dimensionless parameters $u/2\gamma L$ and $W = \langle n_i |u_i|^2 \rangle / 4\pi\gamma^2$, where n_i is the concentration of scatterers in a unit area, u_i is the integrated intensity of a scattering potential, $u = \langle |u_i| \rangle$, and $\langle \cdots \rangle$ denotes the sample average.

relaxation time, and v_{mk} is the group velocity. Substituting eq. (7.31) into eq. (7.29), we obtain the following equation for the mean free path $\Lambda_m(\varepsilon) = |v_{mk}|\tau_m$ for band m:

$$\sum_{m'} (K_{m-m'+} - K_{m+m'+})\Lambda_{m'}(\varepsilon) = 1, \qquad (7.32)$$

where m and m' denote the bands crossing the energy ε, and $+$ $(-)$ the wave vector corresponding to the positive (negative) velocity in the y direction. The kernel for the transport equation is given by

$$K_{\beta\alpha} = \frac{A\langle |V_{\beta\alpha}|^2 \rangle}{\hbar^2 |v_\beta v_\alpha|}, \qquad (7.33)$$

for $\beta \neq \alpha$, where v_α is the velocity of mode $\alpha \equiv (m\pm)$. The diagonal elements are defined by

$$K_{\alpha\alpha} = -\sum_{\beta \neq \alpha} K_{\beta\alpha}. \qquad (7.34)$$

The conductivity becomes

$$\sigma = \int d\varepsilon \left(-\frac{\partial f}{\partial \varepsilon} \right) \sigma(\varepsilon), \qquad (7.35)$$

with

$$\sigma(\varepsilon) = \frac{e^2}{\pi\hbar} \sum_m \Lambda_m(\varepsilon). \qquad (7.36)$$

The actual conductivity should be obtained by multiplication of factor four corresponding to the electron spin
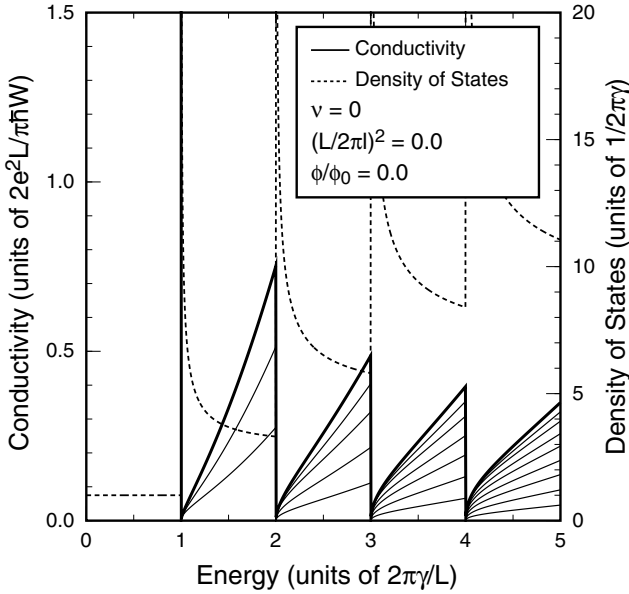
Fig. 33 An example of the energy dependence of the conductivity calculated using Boltzmann transport equation. The conductivity is infinite in the energy range $-1 < \varepsilon L/2\pi\gamma < +1$ but becomes finite in the other region where there are several bands coexist at the Fermi level. The dashed line shows the density of states and thin solid lines show the contribution of each band to the conductivity (the lowest curve represents the contribution of $m=0$, the next two $m=\pm 1$, ...).
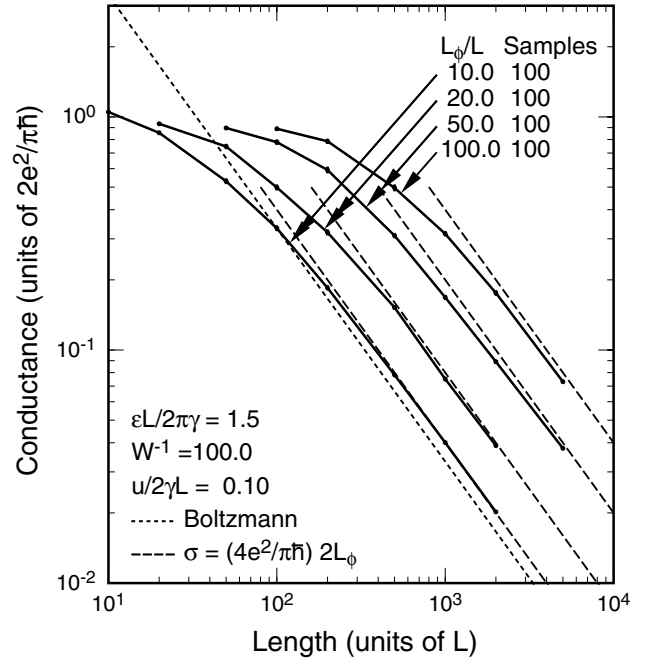

Fig. 34 An example of the conductance in the presence of inelastic scattering as a function of the length for different values of the phase coherence length L_ϕ.

and the presence of K and K' points. Note that eq. (2.16) of ref. 124 should be multiplied by two.

Figure 33 shows an example of the conductivity obtained by solving the Boltzmann equation. The Boltzmann equation gives an infinite conductivity as long as the Fermi level lies in the energy range $-1 < \varepsilon(2\pi\gamma/L)^{-1} < +1$ where only the linear metallic bands are present. However, the conductivity becomes finite when the Fermi energy moves into the range where other bands are present.

This conclusion is quite in contrast to the exact prediction discussed in the previous section that there is at least a channel which transmits through the system with probability unity, leading to the conclusion that the conductance is given by $2e^2/\pi\hbar$ independent of the energy for sufficiently long nanotubes. The difference originates from the absence of phase coherence in the approach based on a transport equation. In fact, in the transport equation scattering from each impurity is treated as a completely independent event after which an electron looses its phase memory, while in the transmission approach the phase coherence is maintained throughout the system. The same problems appears in the dynamical conductivity.[125]

Effects of inelastic scattering can be considered in a model in which the nanotube is separated into segments with length of the order of the phase coherence length L_ϕ and the electron looses the phase information after the transmission through each segment. Actually, adjacent segments are connected to each other in terms of the transmission and reflection probabilities instead of the transmission and reflection coefficients, which destroys the phase coherence between the segments. The length

of each segment is chosen at random with average L_ϕ.

Figure 34 shows some examples of calculated conductance. As long as the length is smaller than or comparable to L_ϕ, the conductance is close to the ideal value $2e^2/\pi\hbar$ corresponding to the presence of a perfect channel. When the length becomes much larger than L_ϕ, the conductance decreases in proportion to the inverse of the length. With the decrease of L_ϕ, the conductance decreases and becomes closer to the Boltzmann result given by the dotted line. These results correspond to the fact that a conductivity can be defined for finite L_ϕ such that it is proportional to L_ϕ. The presence of a perfectly conducting channel and its sensitivity to inelastic scattering were obtained also with the use of a maximum entropy approximation for the distribution of a transfer matrix.[126,127]

7.7 Effects of Symmetry Breaking

The symmetry leading to the perfectly conducting channel is destroyed obviously by a magnetic field perpendicular to the axis and a flux due to a magnetic field parallel to the axis.[128] The symmetry is affected also by scatterers with range smaller than the lattice constant a.[129] Its strength is characterized by the amount of short-range scatterers relative to the total amount of scatterers. It is destroyed also by the presence of trigonal warping of the bands around the K and K' points.[130] In fact, it is straightforward to show that $\mathcal{H}_1^T = -\mathcal{H}_1$, where $\mathcal{H}_1$ represent the higher-order $\boldsymbol{k}\cdot\boldsymbol{p}$ part of the Hamiltonian (3.43). The effect of warping is characterized by $\delta a/L$ where δ is a dimensionless quantity of the order of unity as has been discussed in §3.6.

Figure 35 shows the arithmetic average $\langle G \rangle$ and geometric average $\exp\langle \ln G \rangle$ of the conductivity as a function of the length in weak magnetic fields. The upward arrows indicate the localization length ξ, determined by $\exp\langle \ln G(A) \rangle \propto \exp(-2A/\xi)$, where A is the length of CN.
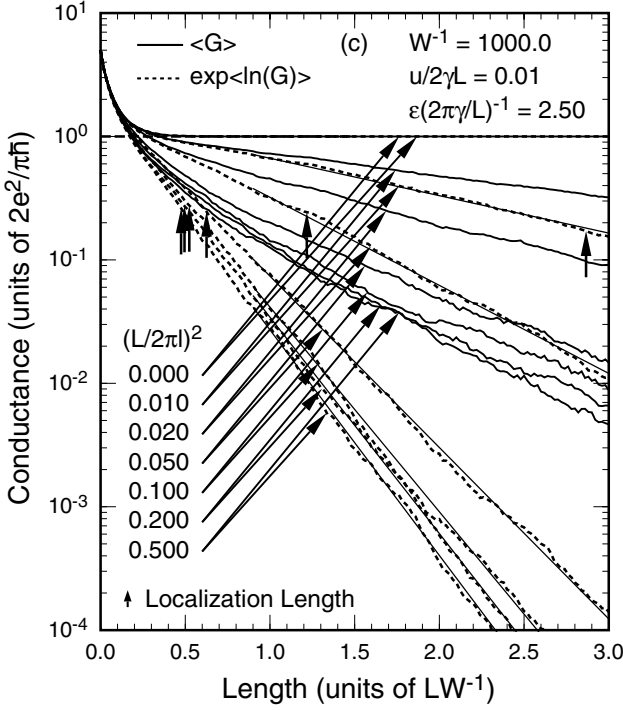
Fig. 35 The arithmetic and geometric averages of the conductivity as a function of the length in weak magnetic fields $(L/2\pi l)^2 \leq 0.5$ for $W^{-1} = 1000$. The upward arrows indicate the localization length ξ. $\varepsilon(2\pi\gamma/L)^{-1} = 1.5$.

For $\varepsilon(2\pi\gamma/L)^{-1} = 0.5$, i.e., when only the metallic linear bands exist, the decay rate of the conductance with the increase of the length remains small in weak magnetic fields $(L/2\pi l)^2 \lesssim 0.1$. The decrease of the conductance with the length becomes appreciable in stronger magnetic fields $(L/2\pi l)^2 \gtrsim 0.1$ for which the modification of the wave function itself starts to be important as discussed in §3.5. Further, the difference between two different averages becomes apparent roughly when the length exceeds the localization length.

Results for several values of the energy ε are shown

in Fig. 36 (a). The number of the bands are 1, 3, 5, and 7 for $\varepsilon(2\pi\gamma/L)^{-1} = 0.5$, 1.5, 2.5, and 3.5, respectively. When there are several bands at the Fermi level, the inverse localization length exhibits a near-plateau behavior above a small critical value. Similar results for magnetic flux, short-range scatterers, and trigonal warping are also included in Fig. 36 as (b), (c), and (d), respectively. The plateau values are nearly same in all the cases and given approximately by the inverse of the sum of the mean free path of the bands obtained in §7.6. All these results show that the perfect channel can easily be destroyed even by a very small perturbation when there are several bands at the energy, while the absence of backscattering is very robust in the energy range of metallic linear bands.

A typical single-wall metallic nanotube without helical structure is a so-called (10,10) armchair nanotube, which has $L/a = 10\sqrt{3}$, corresponding to $a/L = 0.057\cdots$. Even considering the ambiguity in the exact value of δ, we can expect that the effective strength of the trigonal warping is well in the near-plateau region unless some other effects not included make δ much smaller than unity. As a result the perfectly conducting channel is likely to be destroyed in actual single-wall nanotubes and therefore their transport properties are expected to be similar to those in conventional quantum wires with several current carrying subbands.

7.8 Multi-Wall Nanotubes

The magnetoresistance of bundles of multi-wall nanotubes was measured and a negative magnetoresistance was observed in sufficiently low magnetic fields and at low temperatures.[131] With the increase of the magnetic field the resistance starts to exhibit a prominent positive magnetoresistance. This positive magnetoresistance is in qualitative agreement with the theoretical prediction of the reappearance of backscattering in magnetic fields as discussed in §§7.2 and 7.7.

Measurements of the resistance of a single multi-wall nanotube were reported[132−136] and irregular oscillation analogous to universal conductance fluctuations
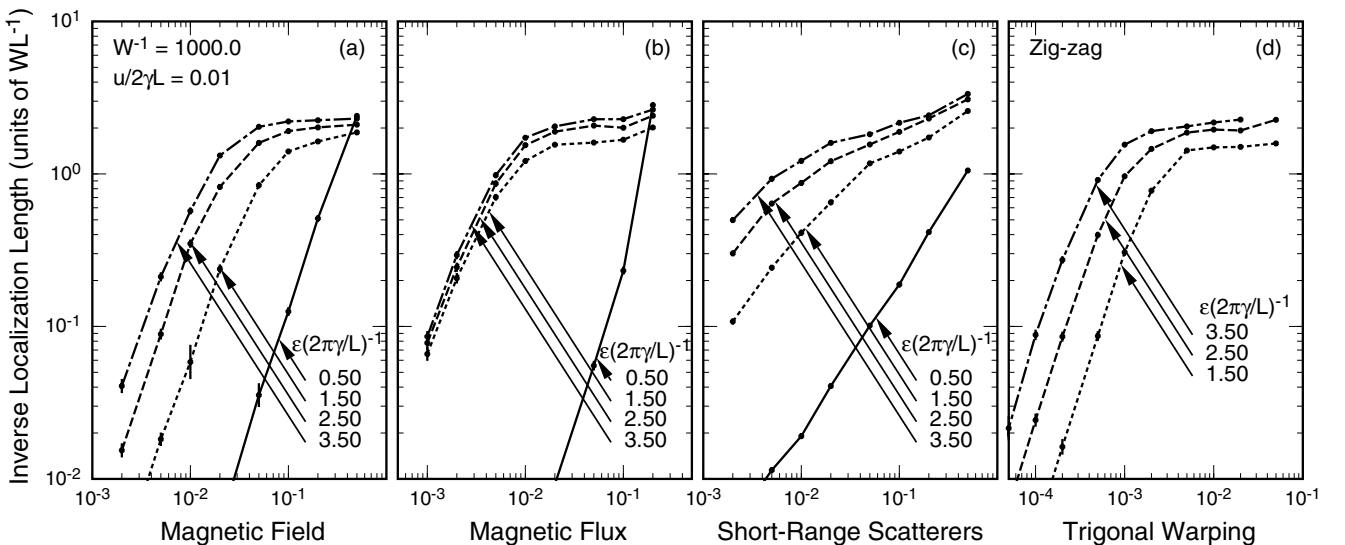

Fig. 36 The inverse localization length as a function of (a) the magnetic field (the horizontal axis denotes $(L/2\pi l)^2$), (b) the magnetic flux (ϕ/ϕ_0), (c) the amount of short-range scatterers, and (d) the trigonal warping of the band $(\delta a/L)$ in a logarithmic scale. In (d), the inverse localization length is much smaller than the range shown in the figure for $\varepsilon(2\pi\gamma/L)^{-1} = 0.5$.

was observed.[132] A resistance oscillation more regular like that of an AB type was observed in a magnetic field parallel to the CN axis.[137,138] Observed resistance oscillation in a parallel field was shown to be consistent with the AB oscillation of the band gap due to a magnetic flux passing through a CN cross section.[139]

A conductance quantization was observed in multi-wall nanotubes, although the quantized value is almost a factor two different between experiments.[140,141] This quantization may be related to the absence of backward scattering shown here, but much more works are necessary before complete understanding of the experimental result. In fact, the observation of huge positive magnetoresistance as predicted in §7.2 is considered to be an unambiguous proof of the conductance quantization due to the absence of backward scattering. Further, problems related to contacts with metallic electrodes should also be understood.[109−113]

At room temperature, where the experiment was performed, phonon scattering through deformation-potential coupling plays an important role in usual materials. In metallic nanotubes, however, the deformation potential does not contribute to the backscattering as long as the Fermi level lies in linear bands and only a weak interaction through bond-length change contribute to the resistivity as will be discussed in §8. As a result a metallic nanotube can be ballistic even at room temperatures. Note that phonon scattering is very sensitive to the presence of a magnetic field.[29]

Conductance due to inter-tube transfer was directly measured in telescoping multi-wall CN's where one end of an outermost tube is connected to an electrode and the other end is peeled open and protruding core tubes are contacted to the other electrode.[142] Measured conductance showed monotonic increase with increase of the telescoping distance suggesting that the dependence comes from localization of sates in the tube axis direction.

Theoretical studies have intensively investigated special cases of commensurate armchair or zigzag double-wall and multi-wall CN's. It was shown that shift of degenerated energy bands occurs and in less symmetric armchair tubes pseudo-gaps open which lead to reduction of the number of conducting channels.[143−146] In double-wall CN's with an infinitely long outer tube and a finite inner tube and in telescoping tubes, in particular, antiresonance of conducting channels with quasi-localized states can cause large conductance oscillations.[146,147]

In actual multi-wall nanotubes, however, the lattice structure of walls are incommensurate with each other and therefore the results for commensurate tubes mentioned above are inapplicable. There have been reported several numerical studies of electronic states[148,149] and transport properties.[150−153] Most of the results show that the transfer is negligibly small near the Fermi energy. The difference between crystal momenta of states of inner and outer tubes in the absence of inter-tube coupling was suggested to be responsible,[151] as in the case of carbon-nanotube ropes[154] and crossed carbon nanotubes.[155] Effects of inter-tube coupling are still an open issue to be clarified.

§8. Phonons and Electron-Phonon Interaction

8.1 Long Wavelength Phonons

Acoustic phonons important in the electron scattering are described well by a continuum model.[29] The potential-energy functional for displacement $\boldsymbol{u} = (u_x, u_y, u_z)$ is written as

$$U[\boldsymbol{u}] = \int \mathrm{d}x\mathrm{d}y \, \frac{1}{2}\Big(B(u_{xx}+u_{yy})^2 + S\big[(u_{xx}-u_{yy})^2+4u_{xy}^2\big]\Big),$$

$$(8.1)$$

with

$$u_{xx} = \frac{\partial u_x}{\partial x} + \frac{u_z}{R}, \quad u_{yy} = \frac{\partial u_y}{\partial y}, \quad 2u_{xy} = \frac{\partial u_x}{\partial y} + \frac{\partial u_y}{\partial x}, \quad (8.2)$$

where the term u_z/R is due to the finite radius $R = L/2\pi$ of the nanotube. The parameters B and S denote the bulk modulus and the shear modulus, respectively, for a graphite sheet ($B = \lambda + \mu$ and $S = \mu$ with λ and μ being Lame's constants). The kinetic energy is written as

$$K[\boldsymbol{u}] = \int \mathrm{d}x\mathrm{d}y \, \frac{M}{2}\big[(\dot{u}_x)^2 + (\dot{u}_y)^2 + (\dot{u}_z)^2\big], \qquad (8.3)$$

where M is the mass density given by the carbon mass per unit area, $M = 9.66 \times 10^{-7}$ kg/m^2. The corresponding equations of motion are given by

$$M\ddot{u}_x = (B+S)\frac{\partial^2 u_x}{\partial x^2} + S\frac{\partial^2 u_x}{\partial y^2} + B\frac{\partial^2 u_y}{\partial x \partial y} + \frac{B+S}{R}\frac{\partial u_z}{\partial x},$$

$$M\ddot{u}_y = B\frac{\partial^2 u_x}{\partial x \partial y} + (B+S)\frac{\partial^2 u_y}{\partial y^2} + S\frac{\partial^2 u_y}{\partial x^2} + \frac{B-S}{R}\frac{\partial u_z}{\partial y},$$

$$M\ddot{u}_z = -\frac{B+S}{R}\frac{\partial u_x}{\partial x} - \frac{B-S}{R}\frac{\partial u_y}{\partial y} - \frac{B+S}{R^2}u_z.$$

$$(8.4)$$

The phonon modes are specified by the wave vector along the circumference, $\chi(n) = 2\pi n/L$, and that along the axis q, i.e., $\boldsymbol{u}(\boldsymbol{r}) = \boldsymbol{u}_{nq}\exp[\mathrm{i}\chi(n)x + \mathrm{i}qy]$. When $n = 0$ or $\chi(n) = 0$, the eigen equation becomes

$$M\omega^2 \begin{pmatrix} u_x \\ u_y \\ u_z \end{pmatrix} = \begin{pmatrix} Sq^2 & 0 & 0 \\ 0 & (B+S)q^2 & -\mathrm{i}(B-S)qR^{-1} \\ 0 & \mathrm{i}(B-S)qR^{-1} & (B+S)R^{-2} \end{pmatrix} \begin{pmatrix} u_x \\ u_y \\ u_z \end{pmatrix},$$

$$(8.5)$$

which has three eigen-modes called twisting, stretching, and breathing modes.

The twisting mode u_x is made of pure circumference-directional deformation and its velocity v_t is equal to that of the transverse acoustic mode of a graphite sheet,

$$\omega_T(q) = v_T q, \quad v_T = v_T^G = \sqrt{\frac{S}{M}}. \qquad (8.6)$$

In the long wavelength limit $q = 0$, the radial deformation generates a breathing mode u_z with a frequency

$$\omega_B = \sqrt{\frac{B+S}{M}}\frac{1}{R}, \qquad (8.7)$$

which is inversely proportional to the radius R of the CN. In the case $|qR| \ll 1$, the deformation in the nanotube-axis direction generates a stretching mode u_y. When $\omega \ll \omega_B$, we have from the last equation of the above

$$u_z \approx -\mathrm{i}\frac{B-S}{B+S}qR\,u_y. \qquad (8.8)$$

Upon substitution of this into the second equation, we
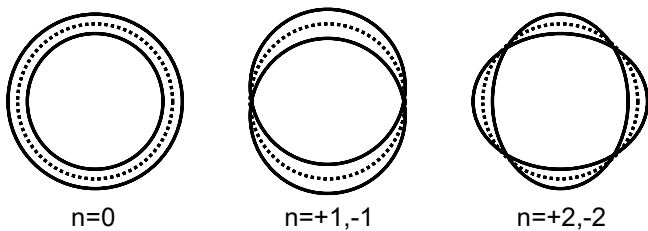
n=0   n=+1,-1   n=+2,-2

Fig. 37   Some examples of deformation of the cross section of CN with $n = 0$, ± 1, and ± 2.

have

$$\omega_S = v_S q, \quad v_S = \sqrt{\frac{4BS}{(B+S)M}}. \quad (8.9)$$

The velocity v_S is usually smaller than that of the longitudinal acoustic mode of the graphite $v_L^G = \sqrt{(B+S)/M}$.

We set $v_L^G = 21.1$ km/s and $v_T^G = 15.0$ km/s, and we obtain $v_s = 21.1$ km/s, $v_t = 15.0$ km/s, and $\hbar\omega_B = 2.04 \times 10^{-2}$ eV, or 237 K for an armchair CN with $R = 0.6785$ nm. These values show good agreement with recent results by Saito et al.[156] Note that the breathing mode can never be reproduced by a zone-folding method in which periodic boundary conditions are imposed on phonons in a 2D graphite sheet as is done for electronic states.

The above model is too simple when dealing with modes with $n \neq 0$. In order to see this fact explicitly, we shall consider the case with $q = 0$. In this case there is a displacement given by

$$u_x = -\frac{u}{n} \sin \frac{2\mathrm{i}nx}{L} = -\frac{u}{n} \sin \frac{nx}{R},$$
$$u_z = u \cos \frac{2\mathrm{i}nx}{L} = u \cos \frac{nx}{R}, \quad (8.10)$$

with arbitrary u. This displacement gives $u_{xx} = 0$ identically and also $u_{yy} = u_{xy} = 0$, giving rise to the vanishing frequency. For $n = \pm 1$, this vanishing frequency is absolutely necessary because the displacement corresponds to a uniform shift of a nanotube in a direction perpendicular to the axis. For $n \geq 2$, on the other hand, the displacement corresponds to a deformation of the cross section of the nanotube as shown in Fig. 37. Such deformations should have nonzero frequency because otherwise CN cannot maintain a cylindrical form.

Actually, we have to consider the potential energy due to nonzero curvature of the 2D graphite plane. It is written as

$$U_c[\boldsymbol{u}] = \frac{1}{2} a^2 \Xi \int \mathrm{d}x \mathrm{d}y \left[\left(\frac{\partial^2}{\partial x^2} + \frac{1}{R^2} + \frac{\partial^2}{\partial y^2} \right) u_z \right]^2, \quad (8.11)$$

where Ξ is a force constant for curving of the plane. The presence of the term $1/R^2$ guarantees that the deformation with $n = \pm 1$ given in eq. (8.10) has a vanishing frequency. This curvature energy is of the order of the fourth power of the wave vector and therefore is much smaller than $U[\boldsymbol{u}]$ as long as $qR \ll 1$ for $n = 0$ and 1 but becomes appreciable for $n \geq 2$.

Figure 38 shows phonon dispersions calculated in this continuum model. The twisting mode with a linear dispersion and the stretching and breathing modes coupled each other at their crossing are given by the solid lines. There exist modes $n = \pm 1$ with frequency which
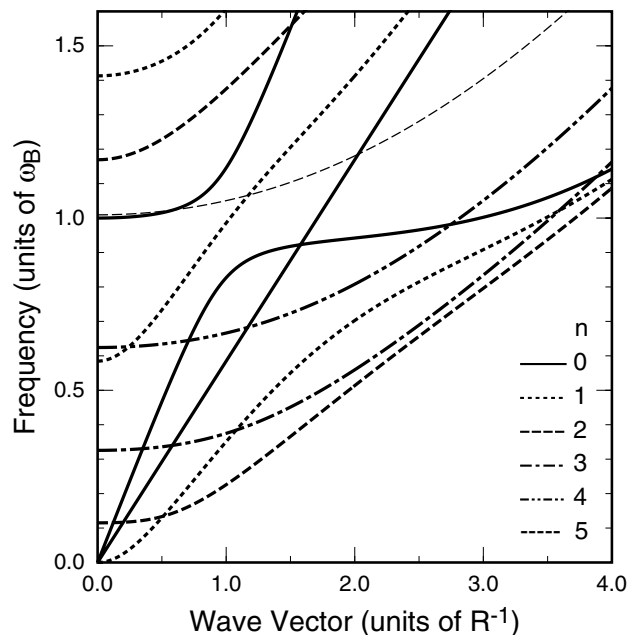

Fig. 38   Frequencies of phonons obtained in the continuum model. ω_B is the frequency of the breathing mode and R is the radius of CN.

vanishes in the long wavelength limit $q \to 0$. These modes correspond to bending motion of the tube and therefore have the dispersion $\omega \propto q^2$ like a similar mode of a rod. In ref. 156 these modes have a linear dispersion $\omega \propto |q|$ presumably due to inappropriate choice of force constants.

Phonon modes in nanotubes were calculated also based on a model 2D graphite with periodic boundary conditions (zone-folding method),[157] in a microscopic model with various force constants,[156] and in a valence-force-field model.[158] First-principles calculations were also performed.[159] A comprehensive review on experiments on phonons was published.[36]

8.2 Electron-Phonon Interaction

A long-wavelength acoustic phonon gives rise to an effective potential called the deformation potential

$$V_1 = g_1(u_{xx} + u_{yy}), \quad (8.12)$$

proportional to a local dilation. This term appears as a diagonal term in the matrix Hamiltonian in the effective-mass approximation. Consider a rectangular area $a \times a$. In the presence of a lattice deformation, the area S changes into $S + \delta S(\boldsymbol{r})$ with $\delta S(\boldsymbol{r}) = a^2 \Delta(\boldsymbol{r})$, where

$$\Delta(\boldsymbol{r}) = \frac{\partial u_x}{\partial x} + \frac{\partial u_y}{\partial y}. \quad (8.13)$$

Therefore, the ion density changes locally by $n_0 \to n_0[1 - \Delta(\boldsymbol{r})]$. The electron density should change in the same manner due to the charge neutrality condition. Consider a two-dimensional electron gas. The potential energy $\delta\varepsilon(\boldsymbol{r})$ corresponding to the density change should satisfy $\delta\varepsilon(\boldsymbol{r})D(\varepsilon_F) = n_0\Delta(\boldsymbol{r})$, where $D(\varepsilon_F)$ is the density of states at the Fermi level $D(\varepsilon) = m/\pi\hbar^2$ independent of energy. Therefore, $n_0 = D(\varepsilon_F)\varepsilon_F$, leading to $\delta\varepsilon(\boldsymbol{r}) = \varepsilon_F\Delta(\boldsymbol{r})$. This shows $g_1 = \varepsilon_F$. In the two-dimensional graphite, the electron gas model may not be so appropriate but can be used for a very rough estimation of g_1 as the Fermi energy measured from the

bottom of the valence bands (σ bands), i.e., $20-30$ eV.

A long-wavelength acoustic phonon also causes a change in the distance between nearest neighbor carbon atoms and in the transfer integral. Let $\boldsymbol{u}_A(\boldsymbol{R}_A)$ and $\boldsymbol{u}_B(\boldsymbol{R}_B)$ be a lattice displacement at A and B site, respectively. Then the transfer integral between an atom at $\boldsymbol{R}_A$ and $\boldsymbol{R}_A - \vec{\tau}_l$ changes from $-\gamma_0$ by the amount

$$-\frac{\partial \gamma_0(b)}{\partial b}\Big[\big|\vec{\tau}_l + \boldsymbol{u}_A(\boldsymbol{R}_A) - \boldsymbol{u}_B(\boldsymbol{R}_A - \vec{\tau}_l)\big| - b\Big]$$
$$= -\frac{\partial \gamma_0(b)}{\partial b}\frac{1}{b}\vec{\tau}_l \cdot \big[\boldsymbol{u}_A(\boldsymbol{R}_A) - \boldsymbol{u}_B(\boldsymbol{R}_A - \vec{\tau}_l)\big], \quad (8.14)$$

where $b = |\vec{\tau}_l| = a/\sqrt{3}$. Therefore, the extra term appearing in the right hand side of eq. (2.19) is calculated as

$$\sum_l \sum_{\boldsymbol{R}_A} g(\boldsymbol{r} - \boldsymbol{R}_A)\boldsymbol{a}(\boldsymbol{R}_A)\boldsymbol{b}(\boldsymbol{R}_A - \vec{\tau}_l)^\dagger\Big(-\frac{\partial \gamma_0(b)}{\partial b}\Big)$$
$$\times \frac{1}{b}\vec{\tau}_l \cdot \big[\boldsymbol{u}_A(\boldsymbol{R}_A) - \boldsymbol{u}_B(\boldsymbol{R}_A - \vec{\tau}_l)\big]\boldsymbol{F}_B(\boldsymbol{r})$$
$$= \sum_l \begin{pmatrix} -\omega \mathrm{e}^{\mathrm{i}\eta}\mathrm{e}^{-\mathrm{i}\boldsymbol{K}\cdot\vec{\tau}_l} & 0 \\ 0 & \mathrm{e}^{-\mathrm{i}\eta}\mathrm{e}^{-\mathrm{i}\boldsymbol{K}'\cdot\vec{\tau}_l} \end{pmatrix}\Big(-\frac{\partial \gamma_0(b)}{\partial b}\Big)$$
$$\times \frac{1}{b}\vec{\tau}_l \cdot \big[\boldsymbol{u}_A(\boldsymbol{r}) - \boldsymbol{u}_B(\boldsymbol{r} - \vec{\tau}_l)\big]\boldsymbol{F}_B(\boldsymbol{r}). \quad (8.15)$$

Because $\boldsymbol{u}_A(\boldsymbol{r}) - \boldsymbol{u}_B(\boldsymbol{r} - \vec{\tau}_l)$ involves displacements of different sublattices, it is determined mostly by optical modes and the contribution of acoustic modes is much smaller. In the long-wavelength limit, we can set

$$\vec{\tau}_l \cdot \big[\boldsymbol{u}_A(\boldsymbol{r}) - \boldsymbol{u}_B(\boldsymbol{r} - \vec{\tau}_l)\big] = \lambda_1 \vec{\tau}_l \cdot \big[\boldsymbol{u}(\boldsymbol{r}) - \boldsymbol{u}(\boldsymbol{r} - \vec{\tau}_1)\big]$$
$$= \lambda_1 (\vec{\tau}_l \cdot \vec{\nabla})\,\vec{\tau}_l \cdot \boldsymbol{u}(\boldsymbol{r}), \quad (8.16)$$

where λ_1 is a constant much smaller than unity. This λ_1 depends on details of a microscopic model of phonons and becomes factor $\sim 1/3$ smaller than unity in a simple valence-force-field model.[29,158]

Now, we shall use the identity

$$\sum_l \mathrm{e}^{-\mathrm{i}\boldsymbol{K}\cdot\vec{\tau}_l}\big((\tau_l^x)^2 \ \ \tau_l^x\tau_l^y \ \ (\tau_l^y)^2\big) = \frac{\omega^{-1}}{4}a^2\left(-1 \ \ -\mathrm{i} \ \ +1\right),$$
$$\sum_l \mathrm{e}^{-\mathrm{i}\boldsymbol{K}'\cdot\vec{\tau}_l}\big((\tau_l^x)^2 \ \ \tau_l^x\tau_l^y \ \ (\tau_l^y)^2\big) = \frac{1}{4}a^2\left(-1 \ \ +\mathrm{i} \ \ +1\right).$$
$$(8.17)$$

Then, we have

$$\frac{3\lambda_1\lambda_2}{4}\gamma_0\begin{pmatrix} \mathrm{e}^{\mathrm{i}\eta}\big(\frac{\partial}{\partial x}+\mathrm{i}\frac{\partial}{\partial y}\big)(u_x+\mathrm{i}u_y) & 0 \\ 0 & -\mathrm{e}^{-\mathrm{i}\eta}\big(\frac{\partial}{\partial x}-\mathrm{i}\frac{\partial}{\partial y}\big)(u_x-\mathrm{i}u_y) \end{pmatrix},$$
$$(8.18)$$

with

$$\lambda_2 = -\frac{b}{\gamma_0}\frac{\partial \gamma_0}{\partial b} = -\frac{\mathrm{d}\ln\gamma_0}{\mathrm{d}\ln b}. \quad (8.19)$$

The above quantities are those in the coordinate system fixed onto the graphite sheet and become in the coordinate system defined in the nanotube

$$u_x \pm \mathrm{i}u_y \to \mathrm{e}^{\pm\mathrm{i}\eta}(u_x\pm\mathrm{i}u_y), \quad \frac{\partial}{\partial x}\pm\mathrm{i}\frac{\partial}{\partial y} \to \mathrm{e}^{\pm\mathrm{i}\eta}\Big(\frac{\partial}{\partial x}\pm\mathrm{i}\frac{\partial}{\partial y}\Big).$$
$$(8.20)$$

Similar expressions can be obtained for $\boldsymbol{F}_B$ and the ef-

fective Hamiltonian becomes

$$\mathcal{H}'_K = \begin{pmatrix} 0 & V_2 \\ V_2^* & 0 \end{pmatrix}, \quad \mathcal{H}'_{K'} = \begin{pmatrix} 0 & -V_2^* \\ -V_2 & 0 \end{pmatrix}, \quad (8.21)$$

with

$$V_2 = g_2\mathrm{e}^{3\mathrm{i}\eta}(u_{xx}-u_{yy}+2\mathrm{i}u_{xy}), \quad (8.22)$$

where

$$g_2 = \frac{3\lambda_1\lambda_2}{4}\gamma_0. \quad (8.23)$$

Usually, we have $\lambda_2 \sim 2$ for s and p electrons,[160] which combined with $\lambda_1 \sim 1/3$ gives $g_2 \sim \gamma_0/2$ or $g_2 \sim 1.5$ eV. This coupling constant is much smaller than the deformation potential constant $g_1 \sim 30$ eV.

8.3 Resistivity

Consider the wave function corresponding to (3.26) with eqs. (3.27) and (3.28) in the presence of AB flux. Apart from the spatial part of the wave function, the (pseudo) spin part of the matrix element is given by

$$\Big(s, n, -k\Big|\begin{pmatrix} V_1 & V_2 \\ V_2^* & V_1 \end{pmatrix}\Big|s, n, +k\Big)$$
$$= \frac{\kappa_{\nu\varphi}(n)[\kappa_{\nu\varphi}(n)-\mathrm{i}k]}{\kappa_{\nu\varphi}(n)^2+k^2}V_1 + \frac{s[\kappa_{\nu\varphi}(n)-\mathrm{i}k]}{\sqrt{\kappa_{\nu\varphi}(n)^2+k^2}}\mathrm{Re}V_2. \quad (8.24)$$

The absolute value of the coefficient of the larger deformation potential is given by $|\kappa_{\nu\varphi}(n)|/\sqrt{\kappa_{\nu\varphi}(n)^2+k^2}$. For the bands with $\kappa_{\nu\varphi}(n) \neq 0$ like in semiconducting CN's, the matrix element is close to V_1 near the band edges $|k| \ll |\kappa_{\nu\varphi}(n)|$ and decreases slowly with the increase of k. For bands with $\kappa_{\nu\varphi}(n) = 0$ having a linear dispersion, however, the coefficient of the deformation potential vanishes identically.

This means that the diagonal deformation-potential term does not contribute to the backward scattering in a metallic linear bands and only the real part of the much smaller off-diagonal term contributes to the backward scattering. We have

$$\mathrm{Re}V_2 = g_2[\cos 3\eta(u_{xx}-u_{yy}) - 2\sin 3\eta\,u_{xy}]. \quad (8.25)$$

In metallic armchair nanotubes with $\eta = \pi/6$, we have $\mathrm{Re}V_2 = -2g_2u_{xy}$ and only shear or twist waves contribute to the scattering. In metallic zigzag nanotubes with $\eta = 0$, on the other hand, $\mathrm{Re}V_2 = g_2(u_{xx}-u_{yy})$ and only stretching and breathing modes contribute to the scattering. Note that the off-diagonal term due to bond-length change is not important in semiconducting nanotubes because of the presence of much larger deformation potential coupling and therefore this dependence on the structure of CN's is absent.

Consider metallic CN's. When a high-temperature approximation is adopted for phonon distribution function, the resistivity for an armchair nanotube is calculated as

$$\rho_A(T) = \frac{\hbar}{e^2}\frac{1}{R}\frac{g_2^2 k_B T}{2\gamma^2 S}. \quad (8.26)$$

At temperatures much higher than the frequency of the breathing mode ω_B, the resistivity of a zigzag nanotube is same as $\rho_A(T)$, i.e., $\rho_Z(T) = \rho_A(T)$. At temperatures lower than ω_B, on the other hand, the breathing mode does not contribute to the scattering and therefore the resistivity becomes smaller than that of an armchair nanotube with same radius, i.e., $\rho_Z(T) = \rho_A(T)B/(B+$
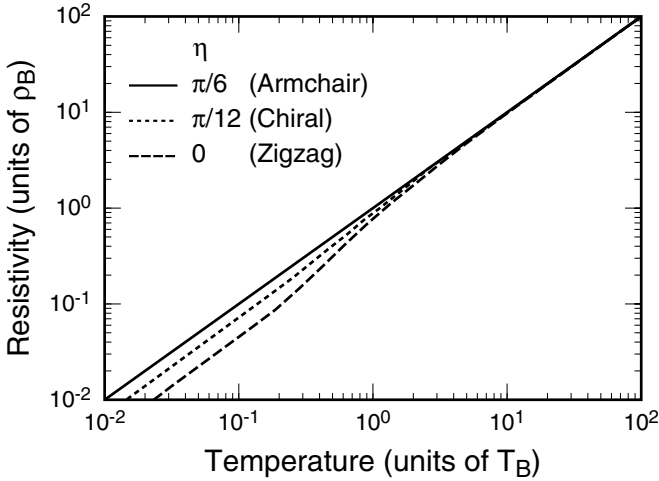
Fig. 39 The resistivity of armchair (solid line) and zigzag (dotted line) nanotubes in units of $\rho_A(T_B)$ which is the resistivity of the armchair nanotube at $T = T_B$, and T_B denotes the temperature of the breathing mode, $T_B = \hbar\omega_B/k_B$.
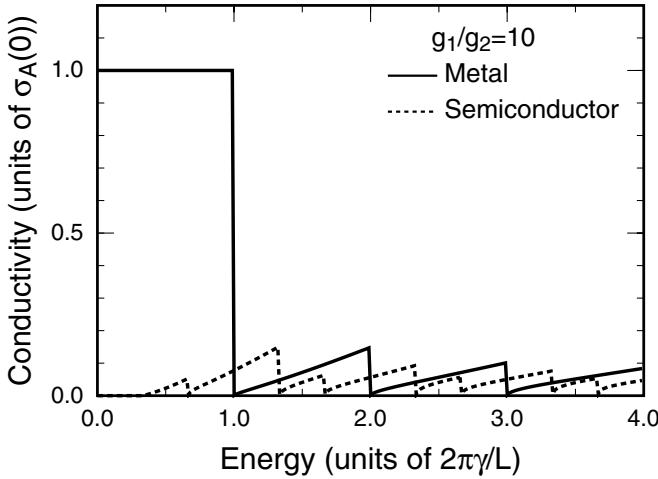

Fig. 40 Fermi-energy dependence of conductivity for metallic (solid line) and semiconducting (broken line) CN's with $g_1/g_2 = 10$ in units of $\sigma_A(0)$ denoting the conductivity of an armchair CN with $\varepsilon = 0$.

S). Figure 39 shows calculated temperature dependence of the resistivity. Because of the small coupling constant g_2 the absolute value of the resistivity is much smaller than that in bulk 2D graphite dominated by much larger deformation-potential scattering. The resistivity of an armchair CN is same as that obtained in ref. 53 except for a significant difference in g_2.

8.4 Multi-Band Transport

When several bands coexist at the Fermi level, it is necessary to solve the Boltzmann transport equation taking scattering between bands into account.[124,161] It is easy to solve the transport equation if elastic-scattering approximation valid at room temperature is employed as has been discussed in §7.6. Figure 40 shows the resulting Fermi energy dependence of conductivity for metallic and semiconducting CN's.

In metallic CN's, when $\varepsilon(2\pi\gamma/L)^{-1} < 1$, the diagonal potential g_1 causes no backward scattering between two bands with linear dispersion and smaller off-diagonal potential g_2 determines the resistivity. However, when the

Fermi energy becomes higher and the number of sub-bands increases, g_1 dominates the conductivity due to interband scattering. This is the reason that the conductivity changes drastically depending on the Fermi energy in metallic CN's. On the other hand, such a drastic change disappears for semiconducting CN's and smaller conductivity compared to that of a metallic CN shows dominance of the diagonal potential independent of the Fermi energy. One noticeable feature is that the conductivity decreases in spite of the increasing number of conducting modes. The reason is that the interband scattering becomes increasingly important than the number of conducting modes as in the case with the impurity scattering.[124]

§9. Lattice Vacancies

9.1 Conductance Quantization

A point defect leads to peculiar electronic states. Scanning-tunneling-micrograph images of a graphene sheet, simulated in the presence of a local point defect, showed that a $\sqrt{3} \times \sqrt{3}$ interference pattern is formed in the wave function near the impurity.[162] This is intuitively understood by a mixing of wave functions at K and K' points. Some experiments suggest the existence of defective nanotubes of carpet-roll or papier-mâché forms.[163,164] These systems have many disconnections of the π electron network and therefore are expected to exhibit properties different from those in perfect CN's. In a graphite sheet with a finite width, for examples, localized edge states are formed at $\varepsilon = 0$, when the boundary is in a certain specific direction.[165]

Effects of scattering by a vacancy in armchair nanotubes have been studied within a tight-binding model.[166,167] Figure 41 shows three typical vacancies: (a) A, (b) AB, and (c) A_3B. In the vacancy (a) a single carbon site (site A) is removed, in the vacancy (b) a pair of A and B sites are removed, and in the vacancy (c) one A site and three B sites are removed. The vacancy (d) is equivalent to (c). It has been shown that the conductance at $\varepsilon = 0$ in the absence of a magnetic field is quantized into zero, one, and two times of the conductance quantum $e^2/\pi\hbar$ for vacancy (c) A_3B, (a) A, and (b) AB, respectively.[167]

Numerical calculations were performed for about 1.5 $\times 10^5$ vacancies.[167] Let N_A and N_B be the number of removed atoms at A and B sublattice points, respectively, and $\Delta N_{AB} = N_A - N_B$. Then, the numerical results show that for vacancies much smaller than the circumference, the conductance vanishes for $|\Delta N_{AB}| \geq 2$ and quantized into one and two times of $e^2/\pi\hbar$ for $|\Delta N_{AB}| = 1$ and
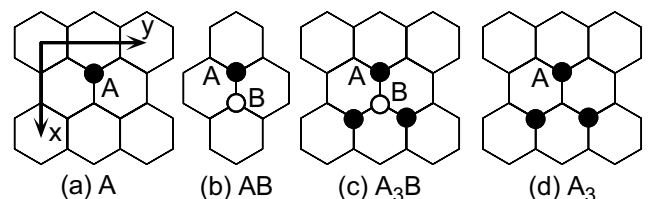

Fig. 41 Schematic illustration of vacancies in an armchair nanotube. The closed and open circles denote A and B lattice points, respectively. (a) A, (b) AB, (c) A_3B, and (d) A_3.

0, respectively. Figure 42(a) shows the histogram giving the distribution of the conductance for CN's with a general defect for $L/\sqrt{3}a = 50$. It has a very small tail on the left-hand side for $\Delta N_{AB} = 0$ and 1. This deviation from the quantized conductance arises mainly from the defects which are exceptionally long in the circumference direction. An example of such defects is illustrated in the inset.

When the circumference of CN's is not large enough compared with the size of a defect, the conductance quantization is destroyed, as shown in Fig. 42(b) for $L/\sqrt{3}a = 10$. In this case, the distribution function has a broad peak around $G = 1.6 \times e^2/\pi\hbar$ when $\Delta N_{AB} = 0$ and has a sharp peak at $G = e^2/\pi\hbar$ accompanied by a long tail for $\Delta N_{AB} = 1$. When $\Delta N_{AB} \geq 2$, however, the conductance is always given by $G = 0$ and a perfect reflection occurs.

9.2 Effective-Mass Description

Effects of impurities with a strong and short-range potential can be studied also in a $\boldsymbol{k}\cdot\boldsymbol{p}$ scheme.[26] As has been discussed in §7.1, for an impurity localized at a carbon A site $\boldsymbol{r}_j$ and having the integrated intensity u, we have[24]

$$V(\boldsymbol{r}) = V_j \delta(\boldsymbol{r} - \boldsymbol{r}_j), \tag{9.1}$$

with

$$V_j = u \begin{pmatrix} 1 & 0 & e^{i\phi_j^A} & 0 \\ 0 & 0 & 0 & 0 \\ e^{-i\phi_j^A} & 0 & 1 & 0 \\ 0 & 0 & 0 & 0 \end{pmatrix}, \tag{9.2}$$

and $\phi_j^A = (\boldsymbol{K}' - \boldsymbol{K}) \cdot \boldsymbol{r}_j + \eta$. For an impurity at a carbon B site we have

$$V_j = u \begin{pmatrix} 0 & 0 & 0 & 0 \\ 0 & 1 & 0 & e^{i\phi_j^B} \\ 0 & 0 & 0 & 0 \\ 0 & e^{-i\phi_j^B} & 0 & 1 \end{pmatrix}, \tag{9.3}$$

with $\phi_j^B = (\boldsymbol{K}' - \boldsymbol{K}) \cdot \boldsymbol{r}_j - \eta + (\pi/3)$.

For this scatterer, the T matrix is solved as

$$(\alpha|T|\beta) = \sum_{ij} \boldsymbol{F}_\alpha^\dagger T_{ij} \boldsymbol{F}_\beta \exp(-i\kappa_\alpha x_i - i k_\alpha y_i)$$
$$\times \exp(i\kappa_\beta x_j + i k_\beta y_j), \tag{9.4}$$

where κ_α and κ_β are the wave vectors in the circumference direction corresponding to channel α and β, k_α and k_β are the wave vectors in the axis direction, $\boldsymbol{F}_\alpha$ and $\boldsymbol{F}_\beta$ are corresponding four-component eigenvectors defined by

$$\boldsymbol{F}_\alpha(\boldsymbol{r}) = \frac{1}{\sqrt{LA}} \boldsymbol{F}_\alpha \exp(i\kappa_\alpha x + i k_\alpha y), \quad \text{etc.}, \tag{9.5}$$

and

$$T_{ij} = \left[\left(1 - \frac{1}{AL} V G(\varepsilon + i0) \right)^{-1} \frac{1}{AL} V \right]_{ij}, \tag{9.6}$$

with $V_{jj'} = V_j \delta_{jj'}$. The Green's function $G_{ij} = G(\boldsymbol{r}_i - \boldsymbol{r}_j)$ is written as

$$G(\boldsymbol{r}) = \frac{-iA}{2\gamma} \begin{pmatrix} G_0 & G_1 & 0 & 0 \\ \bar{G}_1 & G_0 & 0 & 0 \\ 0 & 0 & G_0 & \bar{G}_1 \\ 0 & 0 & G_1 & G_0 \end{pmatrix}, \tag{9.7}$$

with

$$G_0(x, y) = \frac{i\gamma}{\pi} \int dk \sum_n g_0[\varepsilon(n, k)] \frac{\varepsilon\, e^{i\kappa(n)x + iky}}{(\varepsilon + i0)^2 - \gamma^2[\kappa(n)^2 + k^2]},$$

$$G_1(x, y) = \frac{i\gamma}{\pi} \int dk \sum_n g_0[\varepsilon(n, k)] \frac{\gamma[\kappa(n) - ik]\, e^{i\kappa(n)x + iky}}{(\varepsilon + i0)^2 - \gamma^2[\kappa(n)^2 + k^2]},$$
$$\tag{9.8}$$

and $\bar{G}_1(x, y) = G_1(x, -y)$, where $\kappa(n) = \kappa_{\nu\varphi}(n)$ with $\nu = 0$ and $\varphi = 0$, for simplicity.

For a few impurities, the T matrix can be obtained analytically and becomes equivalent to that of lattice vacancies in the limit of strong scatterers, i.e., $|u| \to \infty$. Figure 43 shows the conductance as a function of the Fermi energy in the presence of vacancies A, AB, and A_3B in an armchair nanotube illustrated in Fig. 41. In the case of the A vacancy (a), the conductance becomes
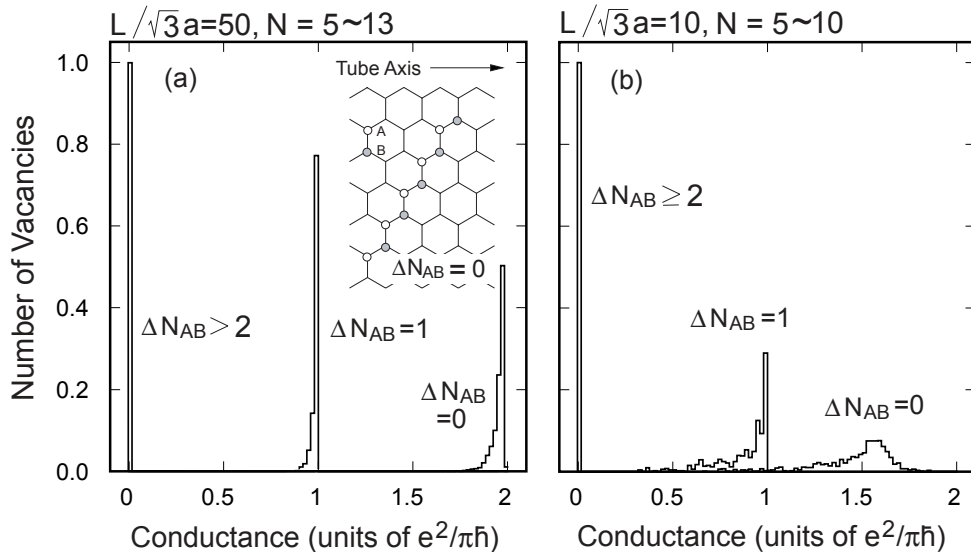

Fig. 42 Calculated distribution of the conductance of armchair CN's with a general defect for (a) $L/a = 50\sqrt{3}$ and for (b) $L/a = 10\sqrt{3}$. The histogram has a width 5.0×10^{-2} in units of $e^2/\pi\hbar$ and is normalized by the total number of defects having specified ΔN_{AB}. The inset shows an example of a defect which causes a large deviation from the quantized conductance.
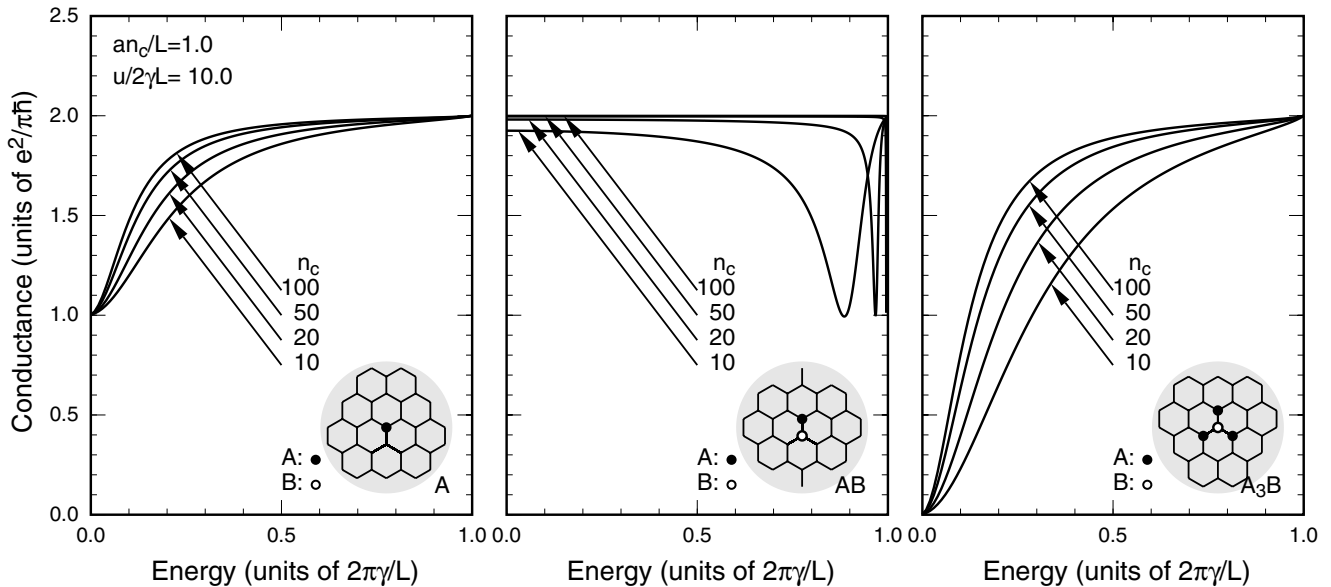
Fig. 43 The energy dependence of the conductance of a vacancy in an armchair nanotube. n_c is a cutoff number corresponding to the condition $\gamma\kappa(n_c) \approx \varepsilon_c$, i.e., $n_c \sim L/a$.

the half of the ideal value $G = e^2/\pi\hbar$ at $\varepsilon = 0$, increases gradually with the increase of ε, and reaches the ideal value $G = 2e^2/\pi\hbar$ at $\varepsilon(2\pi\gamma/L)^{-1} = 1$. The results are in agreement with those obtained in a tight-binding model[167] including the dependence on $n_c \sim L/a$.

In the case of the AB vacancy pair (b) the conductance is slightly smaller than the ideal value $G = 2e^2/\pi\hbar$ and approaches it with the increase of $n_c \sim L/a$ except in the vicinity of $\varepsilon = 2\pi\gamma/L$. Near $\varepsilon = 2\pi\gamma/L$ the conductance exhibits a dip with $G = e^2/\pi\hbar$, which moves to the higher energy side with the increase of $n_c \sim L/a$. At $\varepsilon = 2\pi\gamma/L$ the conductance recovers the ideal value $G = 2e^2/\pi\hbar$. In the case of the A_3B vacancy (c) , the conductance vanishes at $\varepsilon = 0$ and reaches the ideal value $G = 2e^2/\pi\hbar$ at $\varepsilon(2\pi\gamma/L)^{-1} = 1$. These behaviors are in agreement with those in a tight-binding model.[167]

At $\varepsilon = 0$, in particular, we have

$$G_0(x,y) = 1, \qquad G_1(x,y) = \frac{\cos[\pi(x+iy)/L]}{\sin[\pi(x+iy)/L]}. \quad (9.9)$$

The off-diagonal Green's function G_1 is singular in the vicinity of $\boldsymbol{r} = 0$. Therefore, for impurities localized within a distance of a few times of the lattice constant, the off-diagonal Green's function becomes extremely large. This singular behavior is the origin of the peculiar dependence of the conductance on the difference in the number of vacancies at A and B sublattices.

In the limit of $a/L \to 0$ and a strong scatterer the behavior of the conductance at $\varepsilon = 0$ can be studied analytically for arbitrary values of N_A and N_B. The results explain the numerical tight-binding result that $G = 0$ for $|\Delta N_{AB}| \geq 2$, $G = e^2/\pi\hbar$ for $|\Delta N_{AB}| = 1$, and $G = 2e^2/\pi\hbar$ for $\Delta N_{AB} = 0$. The origin of this interesting dependence on N_A and N_B is a reduction of the scattering potential by multiple scattering on a pair of A and B scatterers. In fact, multiple scattering between an A impurity at $\boldsymbol{r}_i$ and a B impurity at $\boldsymbol{r}_j$ reduces their effective potential by the factor $|G_1(\boldsymbol{r}_i - \boldsymbol{r}_j)|^{-2} \propto (a/L)^2$. By eliminating AB pairs successively,

some A or B impurities remain. The conductance is determined essentially by the number of these unpaired impurities.

Such a direct pair-elimination procedure is not rigorous because there are many different ways in the elimination of AB pairs and multiple scattering between unpaired and eliminated impurities cannot be neglected completely because of large off-diagonal Green's functions. However, a correct mathematical procedure can be formulated in which a proper combination of A and B impurities leads to a vanishing scattering potential and the residual potential is determined by another combination of remaining A or B impurities.[26]

Effects of a magnetic field were studied for three types of vacancies shown in Fig. 41.[167] The results show a universal dependence on the field component in the direction of the vacancy position. These results are analytically derived in the effective-mass scheme.[168] Effects of a single B and N atom on transport in a (10,10) CN were studied using an *ab initio* pseudopotential method,[169] which showed that doped B and N produce a quasi-bound impurity state slightly above the Fermi energy corresponding to a finite potential height of the order of γ_0.

The singularity of the off-diagonal Green's function $\propto L/a$ becomes important when the local site energy u/a^2 becomes comparable to γ_0. Therefore, the effective potential of scatterers, eqs. (7.3) and (7.5), obtained in §7 is valid under the condition that $|u_A(\boldsymbol{R}_A)/\gamma_0| \ll 1$ and $|u_B(\boldsymbol{R}_B)/\gamma_0| \ll 1$ and becomes inappropriate when $u_A(\boldsymbol{R}_A)$ and $u_B(\boldsymbol{R}_B)$ are comparable or larger than γ_0.

§10. Junctions and Topological Defects

10.1 Five- and Seven-Membered Rings

A junction which connects CN's with different diameters through a region sandwiched by a pentagon-heptagon pair has been observed in the transmission electron microscope.[2] In fact, a pair of five- and seven-
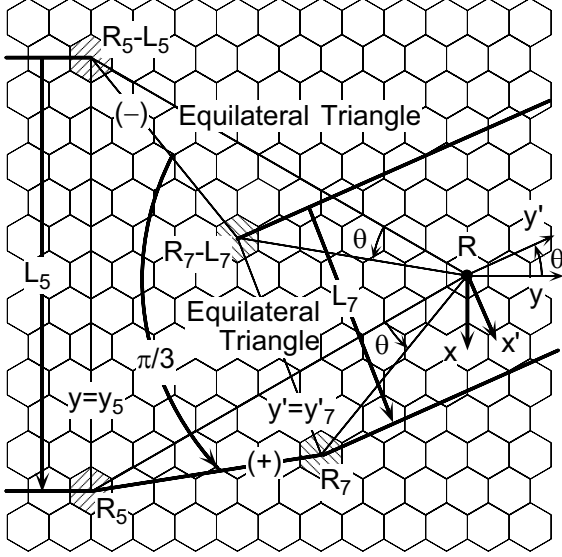
Fig. 44 The structure of a junction consisting of two nanotubes with chiral vector $\boldsymbol{L}_5$ and $\boldsymbol{L}_7$ not parallel to each other (θ is their angle).

membered rings makes it possible to connect two different types of CN's and thus construct various kinds of CN junctions.[170,171] Some theoretical calculations within a tight-binding model were reported for junctions between metallic and semiconducting nanotubes and those between semiconducting nanotubes.[171,172] In particular tight-binding calculations for junctions consisting of two metallic tubes with different chirality or diameter demonstrated that the conductance exhibits a universal power-law dependence on the ratio of the circumference of two nanotubes.[173]

A bend-junction was observed experimentally and the conductance across such a junction between a (6,6) armchair CN and a (10,0) zigzag CN was discussed.[174] Energetics of bend junctions were calculated.[175] Transport measurements of both metal-semiconductor and metal-metal junctions were reported.[176] The bend junction is a special case of the general junction. Junctions can contain many pairs of topological defects. Effects of three pairs present between metallic (6,3) and (9,0) nanotubes were studied,[166] which shows that the conductance vanishes for junctions having a three-fold rotational symmetry, but remains nonzero for those without the symmetry. Three-terminal CN systems are also formed with a proper combination of five- and n-membered ($n \geq 8$) rings.[177−179]

A Stone-Wales defect or *azupyrene* is a kind of topological defect in graphite network.[180] They are composed of two pairs of five- and seven-membered rings, which can be introduced by rotating a C-C bond inside four adjacent six-membered rings. There are many other interesting CN networks. For example, a lot of pairs of five- and seven-membered rings aligned periodically along the tube length can form another interesting networks such as toroidals[181,182] and helically-coiled CN's.[170,183−185] A new type of carbon particles was produced by laser ablation method in bulk quantities. An individual particle is a spherical aggregate of many single-walled tubule-like structures with conical tips with an

average cone angle of 20°. The conical tips of individual tubules are protruding out of the surface of the aggregate like horns, and they are called carbon nanohorns.[186]

10.2 Boundary Conditions

Let us consider a junction having a general structure. Figure 44 shows an example of such junctions.[171] The junction is characterized by two equilateral triangles with a common vertex point and sides parallel to the chiral vectors $\boldsymbol{L}_5$ and $\boldsymbol{L}_7$ with tilt angle θ of two nanotubes. There is a five-member ring (whose position is denoted as $\boldsymbol{R}_5$) at the boundary of the thicker nanotube and the junction region and a seven-member ring ($\boldsymbol{R}_7$) at the boundary of the junction region and the thinner nanotube. For any site close to the upper boundary denoted as $(-)$, there exists a corresponding site near the lower boundary denoted as $(+)$ obtained by a rotation $R_{\pi/3}$ around $\boldsymbol{R}$ by $\pi/3$.

By a proper extrapolation of the wave functions outside of the junction region, we can generalize the boundary conditions as

$$
\begin{aligned}
\psi_A(\boldsymbol{R}'_A) &= \psi_B(\boldsymbol{R}_B), \\
\psi_B(\boldsymbol{R}'_B) &= \psi_A(\boldsymbol{R}_A),
\end{aligned}
\tag{10.1}
$$

with

$$
\begin{aligned}
\boldsymbol{R}'_A &= R_{\pi/3}(\boldsymbol{R}_B - \boldsymbol{R}) + \boldsymbol{R}, \\
\boldsymbol{R}'_B &= R_{\pi/3}(\boldsymbol{R}_A - \boldsymbol{R}) + \boldsymbol{R},
\end{aligned}
\tag{10.2}
$$

for all lattice points $\boldsymbol{R}_A$ and $\boldsymbol{R}_B$.

In terms of the envelope functions, these conditions can be written explicitly as

$$
\begin{aligned}
\boldsymbol{a}(\boldsymbol{R}'_A)^\dagger \boldsymbol{F}_A(\boldsymbol{R}'_A) &= \boldsymbol{b}(\boldsymbol{R}_B)^\dagger \boldsymbol{F}_B(\boldsymbol{R}_B), \\
\boldsymbol{b}(\boldsymbol{R}'_B)^\dagger \boldsymbol{F}_B(\boldsymbol{R}'_B) &= \boldsymbol{a}(\boldsymbol{R}_A)^\dagger \boldsymbol{F}_A(\boldsymbol{R}_A).
\end{aligned}
\tag{10.3}
$$

In the following we shall choose the origin at $\boldsymbol{R}$, i.e., $\boldsymbol{R}=0$. Because $R_{\pi/3}^{-1}\boldsymbol{K} = \boldsymbol{K}'$, we have

$$
\begin{aligned}
\exp(i\boldsymbol{K}\cdot\boldsymbol{R}'_A) &= \exp\left(i[R_{\pi/3}^{-1}\boldsymbol{K}]\cdot\boldsymbol{R}_B\right) = \exp(i\boldsymbol{K}'\cdot\boldsymbol{R}_B), \\
\exp(i\boldsymbol{K}\cdot\boldsymbol{R}'_B) &= \exp\left(i[R_{\pi/3}^{-1}\boldsymbol{K}]\cdot\boldsymbol{R}_A\right) = \exp(i\boldsymbol{K}'\cdot\boldsymbol{R}_A).
\end{aligned}
\tag{10.4}
$$

Further, we have $R_{\pi/3}^{-1}\boldsymbol{K}' = \boldsymbol{K} - \boldsymbol{b}^*$. Noting that $\boldsymbol{R}_A = n_a\boldsymbol{a} + n_b\boldsymbol{b} - \vec{\tau}_3$ and $\boldsymbol{R}_B = n_a\boldsymbol{a} + n_b\boldsymbol{b} + \vec{\tau}_2$ with integers n_a and n_b, we have

$$
\begin{aligned}
\exp(i\boldsymbol{K}'\cdot\boldsymbol{R}'_A) &= \exp[i(\boldsymbol{K}-\boldsymbol{b}^*)\cdot\boldsymbol{R}_B] = \omega\exp(i\boldsymbol{K}\cdot\boldsymbol{R}_B), \\
\exp(i\boldsymbol{K}'\cdot\boldsymbol{R}'_B) &= \exp[i(\boldsymbol{K}-\boldsymbol{b}^*)\cdot\boldsymbol{R}_A] = \omega^{-1}\exp(i\boldsymbol{K}\cdot\boldsymbol{R}_A),
\end{aligned}
\tag{10.5}
$$

where use has been made of $\exp(-i\boldsymbol{b}^*\cdot\vec{\tau}_3) = \omega$ and $\exp(i\boldsymbol{b}^*\cdot\vec{\tau}_2) = \omega^{-1}$.

We first multiply $g(\boldsymbol{r}-\boldsymbol{R}_B)\boldsymbol{b}(\boldsymbol{R}_B)$ from the left on both sides of the first of eq. (10.3) and sum them up over $\boldsymbol{R}_B$ to have

$$
\begin{aligned}
&\sum_{\boldsymbol{R}_B} g(\boldsymbol{r}-\boldsymbol{R}_B)\boldsymbol{b}(\boldsymbol{R}_B)\boldsymbol{a}(\boldsymbol{R}'_A)^\dagger \boldsymbol{F}_A(R_{\pi/3}\boldsymbol{r}) \\
&= \sum_{\boldsymbol{R}_B} g(\boldsymbol{r}-\boldsymbol{R}_B)\boldsymbol{b}(\boldsymbol{R}_B)\boldsymbol{b}(\boldsymbol{R}_B)^\dagger \boldsymbol{F}_B(\boldsymbol{r}).
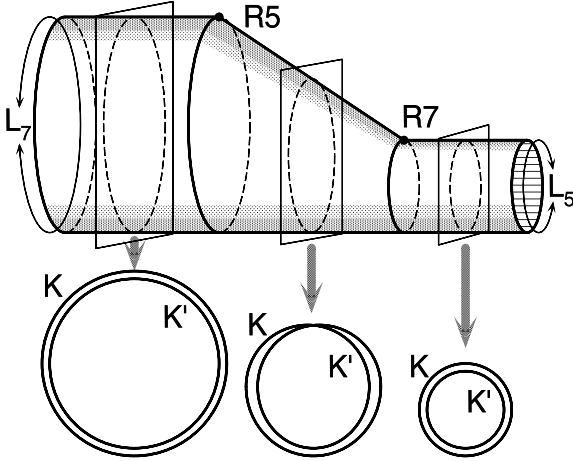\end{aligned}
\tag{10.6}
$$

Fig. 45 Schematic illustration of the topological structure of a junction of two carbon nanotubes with different diameter. In the nanotube regions, two cylinders corresponding to spaces associated with the K and K' points are independent of each other and completely decoupled. In the junction region, on the contrary, they are interconnected to each other.

We have

$$\boldsymbol{b}(\boldsymbol{R}_B)\boldsymbol{b}(\boldsymbol{R}_B)^\dagger = \begin{pmatrix} 1 & -\omega e^{-i\eta}e^{i(\boldsymbol{K}'-\boldsymbol{K})\cdot\boldsymbol{R}_B} \\ -\omega e^{i\eta}e^{-i(\boldsymbol{K}'-\boldsymbol{K})\cdot\boldsymbol{R}_B} & 1 \end{pmatrix},$$

$$\boldsymbol{b}(\boldsymbol{R}_B)\boldsymbol{a}(\boldsymbol{R}_A')^\dagger = \begin{pmatrix} -\omega^{-1}e^{-i\eta}e^{i(\boldsymbol{K}'-\boldsymbol{K})\cdot\boldsymbol{R}_B} & -1 \\ 1 & \omega e^{i\eta}e^{-i(\boldsymbol{K}'-\boldsymbol{K})\cdot\boldsymbol{R}_B} \end{pmatrix}.$$

(10.7)

Therefore, we have

$$\boldsymbol{F}_A(R_{\pi/3}\boldsymbol{r}) = \begin{pmatrix} 0 & 1 \\ -1 & 0 \end{pmatrix} \boldsymbol{F}_B(\boldsymbol{r}). \qquad (10.8)$$

Similarly, the second equation of eq. (10.3) gives

$$\boldsymbol{F}_B(R_{\pi/3}\boldsymbol{r}) = \begin{pmatrix} 0 & -\omega^{-1} \\ \omega & 0 \end{pmatrix} \boldsymbol{F}_A(\boldsymbol{r}). \qquad (10.9)$$

As a result, the boundary conditions for the envelope functions in the junction region are written as[27]

$$\boldsymbol{F}(R_{\pi/3}\boldsymbol{r}) = T_{\pi/3}\,\boldsymbol{F}(\boldsymbol{r}), \qquad (10.10)$$

with

$$T_{\pi/3} = \begin{pmatrix} 0 & 0 & 0 & 1 \\ 0 & 0 & -\omega^{-1} & 0 \\ 0 & -1 & 0 & 0 \\ \omega & 0 & 0 & 0 \end{pmatrix}, \qquad (10.11)$$

where

$$\boldsymbol{F}(\boldsymbol{r}) = \begin{pmatrix} \boldsymbol{F}^K(\boldsymbol{r}) \\ \boldsymbol{F}^{K'}(\boldsymbol{r}) \end{pmatrix}. \qquad (10.12)$$

It is straightforward to show that this should be modified into

$$T_{\pi/3} = \begin{pmatrix} 0 & 0 & 0 & e^{i\psi(\boldsymbol{R})} \\ 0 & 0 & -\omega^{-1}e^{i\psi(\boldsymbol{R})} & 0 \\ 0 & -e^{-i\psi(\boldsymbol{R})} & 0 & 0 \\ \omega e^{-i\psi(\boldsymbol{R})} & 0 & 0 & 0 \end{pmatrix},$$

(10.13)

with

$$e^{i\psi(\boldsymbol{R})} = \exp[i(\boldsymbol{K}'-\boldsymbol{K})\cdot\boldsymbol{R}], \qquad (10.14)$$

if $\boldsymbol{R}$ is not chosen at the origin, i.e., $\boldsymbol{R} \neq 0$. Physical quantities do not depend on the choice of the origin and
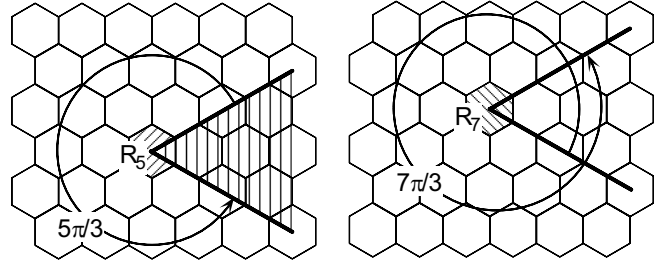

Fig. 46 The structure of a 2D graphite sheet in the vicinity of a five- and seven-member ring.

consequently on the phase $\psi(\boldsymbol{R})$.

Figure 45 gives an illustration of the topological structure of the junction.[27] In the nanotube region, the K and K' points are completely decoupled and therefore belong to different subspaces. In the junction region, the wave function F_A^K turns into $F_B^{K'}$ with an extra phase $e^{-i\psi(\boldsymbol{R})}$ when being rotated once around the axis. After another rotation, it comes back to F_A^K with an extra phase $\omega^{-1} = \exp(-2\pi i/3)$. On the other hand, F_B^K turns into $F_A^{K'}$ with phase $-\omega e^{-i\psi(\boldsymbol{R})}$ under a rotation and then into F_B^K with phase $\omega = \exp(2\pi i/3)$ after another rotation.

The above boundary conditions for nanotubes and their junctions have been obtained based on the nearest-neighbor tight-binding model. The essential ingredients of the boundary conditions lie in the fact that the 2D graphite system is invariant under the rotation of $\pi/3$ followed by the exchange between A and B sublattices. Therefore, the conditions given by eq. (10.10) with eqs. (10.11) or (10.13) are quite general and valid in more realistic models of the band structure.

The present method can be used also to obtain boundary conditions around a five- and seven-member ring schematically illustrated in Fig. 46. First, around the five-member ring, we note that

$$T_{5\pi/3}\,T_{\pi/3} = T_{2\pi} = 1. \qquad (10.15)$$

This immediately gives the conditions

$$\boldsymbol{F}(R_{5\pi/3}\boldsymbol{r}) = T_{5\pi/3}\,\boldsymbol{F}(\boldsymbol{r}), \qquad (10.16)$$

with

$$T_{5\pi/3} = T_{\pi/3}^{-1} = \begin{pmatrix} 0 & 0 & 0 & \omega^{-1} \\ 0 & 0 & -1 & 0 \\ 0 & -\omega & 0 & 0 \\ 1 & 0 & 0 & 0 \end{pmatrix}. \qquad (10.17)$$

Around the seven member ring, on the other hand, we have

$$\boldsymbol{F}(R_{7\pi/3}\boldsymbol{r}) = T_{7\pi/3}\,\boldsymbol{F}(\boldsymbol{r}), \qquad (10.18)$$

with $T_{7\pi/3} = T_{\pi/3}$.

10.3 Conductance

Next, we consider envelope functions in the junction region for $\varepsilon = 0$ choosing the origin of (x, y) at $\boldsymbol{R}$. First, we should note

$$\hat{k}_x + i\hat{k}_y = \frac{2}{i}\frac{\partial}{\partial z_-}, \quad \hat{k}_x - i\hat{k}_y = \frac{2}{i}\frac{\partial}{\partial z_+}, \qquad (10.19)$$

with $z_\pm = x \pm iy$. This means that F_A^K and $F_B^{K'}$ are functions of $z = x + iy$ and F_B^K and $F_A^{K'}$ are functions of $\bar{z} = x - iy$. Therefore, the boundary conditions for F_A^K
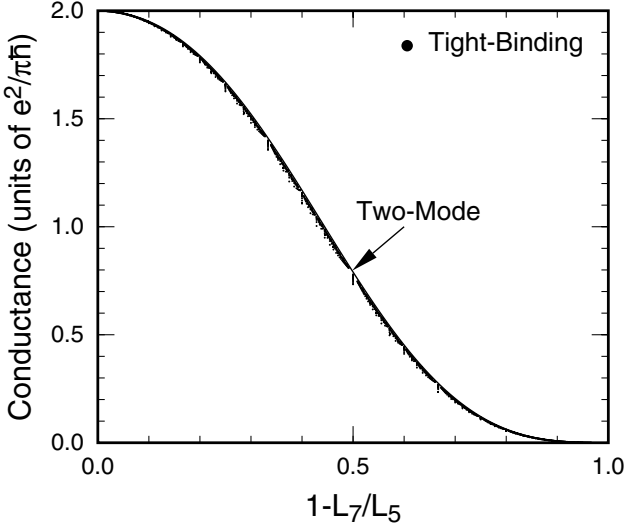
Fig. 47　The conductance obtained in the two-mode approximation and tight-binding results of armchair and zigzag nanotubes versus the effective length of the junction region $(L_5 - L_7)/L_5$.

and $F_B^{K'}$ are given by

$$
\begin{aligned}
F_A^K(\sqrt{\omega}z) &= e^{i\psi(\boldsymbol{R})} F_B^{K'}(z), \\
F_B^{K'}(\sqrt{\omega}z) &= \omega e^{-i\psi(\boldsymbol{R})} F_A^K(z).
\end{aligned}
\tag{10.20}
$$

We seek the solution of the form $F_A^K(z) \propto z^{n_A}$ and $F_B^{K'}(z) \propto z^{n_B}$. The substitution of these into the boundary conditions gives $n_A = n_B = 3m+1$ with m being an integer. Similar relations are also obtained for $F_B^K(\bar{z})$ and $F_A^{K'}(\bar{z})$. We have[27]

$$
\boldsymbol{F}_m^{JA}(z) = \frac{1}{\sqrt{L_5}}
\begin{pmatrix} 1 \\ 0 \\ 0 \\ (-)^m e^{-i\psi'} \end{pmatrix}
\left(\frac{+iz}{L_5} \right)^{3m+1}, \quad (10.21)
$$

and

$$
\boldsymbol{F}_m^{JB}(\bar{z}) = \frac{1}{\sqrt{L_5}}
\begin{pmatrix} 0 \\ 1 \\ (-)^{m+1} e^{-i\psi'} \\ 0 \end{pmatrix}
\left(\frac{-i\bar{z}}{L_5} \right)^{3m+1}, \quad (10.22)
$$

with $e^{-i\psi'} = \sqrt{\omega} e^{-i\psi(\boldsymbol{R})}$.

　　Consider the case $\theta = 0$ for simplicity. The amplitude of the above wave functions decays or grows roughly in proportion to y^{3m+1} with the change of y. In particular, we have

$$
\int_{-L(y)/2}^{+L(y)/2} \boldsymbol{F}_m^{JA*} \cdot \boldsymbol{F}_m^{JA} dx \propto \left(\frac{L(y)}{L_5} \right)^{6m+3}, \quad (10.23)
$$

with $L(y) = -(2/\sqrt{3})y$. This shows that the squared amplitude integrated over x varies in proportion to $[L(y)/L_5]^{6m+3}$ with the change of $L(y)$. In the case of a sufficiently long junction, i.e., for small L_7/L_5, the wave function is dominated by that corresponding to $m=0$. This means that the conductance decays in proportion to $(L_7/L_5)^3$, explaining results of numerical calculations in a tight-binding model quite well.[173]

　　An approximate expression for the transmission T and reflection probabilities R can be obtained by ne-
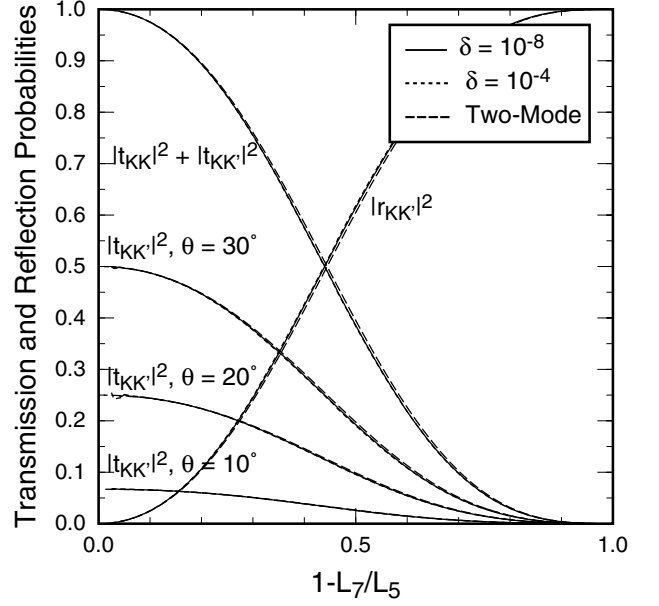

Fig. 48　Calculated transmission and reflection probabilities versus the effective length of the junction region $(L_5 - L_7)/L_5$. Contributions of inter-valley scattering to the transmission are plotted for $\theta = 10°$, $20°$, and $30°$. The results are almost independent of the value of δ.

glecting evanescent modes decaying exponentially into the thick and thin nanotubes. The solution gives

$$
T = \frac{4L_5^3 L_7^3}{(L_5^3 + L_7^3)^2}, \quad R = \frac{(L_5^3 - L_7^3)^2}{(L_5^3 + L_7^3)^2}. \quad (10.24)
$$

We have $T \sim 4(L_7/L_5)^3$ in the long junction $(L_7/L_5 \ll 1)$. When they are separated into different components,

$$
T_{KK} = T\cos^2\left(\frac{3}{2}\theta \right), \quad T_{KK'} = T\sin^2\left(\frac{3}{2}\theta \right), \quad (10.25)
$$

and

$$
R_{KK} = 0, \quad R_{KK'} = R, \quad (10.26)
$$

where the subscript KK means intra-valley scattering within K or K' point and KK' stands for inter-valley scattering between K and K' points. As for the reflection, no intra-valley scattering is allowed. The dependence on the tilt angle θ originates from two effects. One is $\theta/2$ arising from the spinor-like character of the wave function in the rotation θ. Another θ comes from the junction wave function with $m=0$ which decays most slowly along the y axis. Figure 47 shows comparison of the two-mode solution with tight-binding results[173] for $\theta = 0$.

　　In actual calculations, we have to limit the total number of eigen-modes in both nanotube and junction regions. In the junction region the wave function for $m \geq 0$ decays and that for $m < 0$ becomes larger in the positive y direction. We shall choose cutoff M of the number of eigen-modes in the junction region, i.e., $-M-1 \leq m \leq M$, for a given value of L_7/L_5 in such a way that $(\sqrt{3}L_7/2L_5)^{3M} < \delta$, where δ is a positive quantity much smaller than unity. With the decrease of δ, the number of the modes included in the calculation increases.

　　Figure 48 shows some examples of calculated transmission and reflection probabilities for $\delta = 10^{-4}$ and
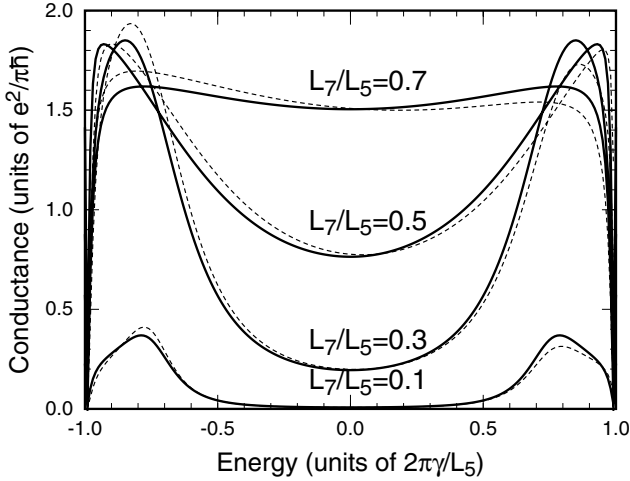
Fig. 49 Calculated conductance versus the energy ε ($-2\pi/L_5 < \varepsilon/\gamma < +2\pi/L_5$) for various values of the junction length. Solid lines represent the results of the $\boldsymbol{k}\cdot\boldsymbol{p}$ method, while dashed lines show tight-binding data for $L_5 = 50\sqrt{3}a$ (a is the lattice constant). The conductance grows with the energy and has a peak before the first band edge $\varepsilon/\gamma = \pm 2\pi/L_5$, followed by an abrupt fall-off.

10^{-8}. As for the transmission, contributions from inter-valley scattering ($K \to K'$) are plotted together for several values of θ. The dependence on the value of δ is extremely small and is not important at all, showing that the analytic expressions for the transmission and reflection probabilities obtained above are almost exact.

Explicit calculations were performed also for $\varepsilon \neq 0$ and Fig. 49 shows an example.[27] The conductance grows with the energy and has a peak before the first band edge $\varepsilon = \pm 2\pi\gamma/L_5$. Near the band edge, the conductance decreases abruptly and falls off to zero. This behavior cannot be obtained if we ignore the evanescent modes in the tube region.[173] This implies the formation of a kind of resonant state in the junction region, which would bring forth the total reflection into the thicker tube region. The tight-binding results[173] show a small asymmetry between $\varepsilon > 0$ and $\varepsilon < 0$. The asymmetry arises presumably from the presence of five- and seven-member rings and is expected to be reduced with the increase of the circumference length.

Effects of a magnetic field perpendicular to the axis were also studied.[187] The results show a universal dependence on the field-component in the direction of the pentagonal and heptagonal rings, similar to that in the case of vacancies.[167] On the other hand, $\boldsymbol{k}\cdot\boldsymbol{p}$ calculation shows that the junction conductance is independent of the magnetic field.[27] In high magnetic fields, the conductance is very sensitive to small perturbations because of a huge buildup of the density of states at $\varepsilon = 0$ as discussed in §3.5. As a result a slight deviation from the effective-mass scheme present in a tight-binding model can cause a large difference.

Some carbon nanotubes are closed by a half fullerene called a cap at the end.[188] According to Euler's theorem there are six five-membered rings in a cap if it contains no other topological defects. Patterns associated with the presence of six five-membered rings were observed by a field emission microscopy.[189] The local density of states

of caps of a nanotube was calculated in a tight-binding model and the presence of states localized in a cap was predicted.[190] Nanotube caps were studied by scanning tunneling microscopy or spectroscopy and a sharp peak was observed in the cap region and similar peaks were obtained theoretically for a model cap structure.[191,192] The boundary conditions around a five-membered ring obtained above have been used for the study of electron scattering by a cap and states localized inside a cap.[23]

10.4 Stone-Wales Defect

As illustrated in Fig. 50 (a), a Stone-Wales defect[180] is realized by bond alternation within four nearest honeycombs. An effective-mass Hamiltonian for a nonlocal Stone-Wales defect can be derived by following a procedure similar to that of impurities or short-range defects.[28]

To express this system we have various choices, as shown in Figs. 50 (b)–(d):

(b) Cut $\boldsymbol{R}_{A1}$–$\boldsymbol{R}_{B3}$ and $\boldsymbol{R}_{B1}$–$\boldsymbol{R}_{A2}$ and connect $\boldsymbol{R}_{A1}$–$\boldsymbol{R}_{A2}$ and $\boldsymbol{R}_{B1}$–$\boldsymbol{R}_{B3}$.

(c) Cut $\boldsymbol{R}_{A1}$–$\boldsymbol{R}_{B2}$ and $\boldsymbol{R}_{B1}$–$\boldsymbol{R}_{A3}$ and connect $\boldsymbol{R}_{A1}$–$\boldsymbol{R}_{A3}$ and $\boldsymbol{R}_{B1}$–$\boldsymbol{R}_{B2}$.

(d) Add $\boldsymbol{R}_{C1}$ and $\boldsymbol{R}_{C2}$ and connect $\boldsymbol{R}_{C1}$–$\boldsymbol{R}_{A2}$, $\boldsymbol{R}_{C1}$–$\boldsymbol{R}_{B2}$, $\boldsymbol{R}_{C2}$–$\boldsymbol{R}_{A3}$, $\boldsymbol{R}_{C2}$–$\boldsymbol{R}_{B3}$, and $\boldsymbol{R}_{C1}$–$\boldsymbol{R}_{C2}$. Set the amplitude of wave functions zero at $\boldsymbol{R}_{A1}$ and $\boldsymbol{R}_{B1}$ by introducing an on-site potential u_0 and letting it sufficiently large.

These bond constructions are classified into two types, asymmetrical way (b) and (c) and symmetrical way (d). The effective Hamiltonian depends on these choices.

Figure 51 shows results of numerical calculations for each model. The conductance exhibits two dips at a positive energy and a negative energy. Except in the vicinity of the dips, the conductance is close to the ideal value $2e^2/\pi\hbar$. With the increase of the circumference, the dip energies approach the band edges and the deviation of the conductance from the ideal value becomes smaller.
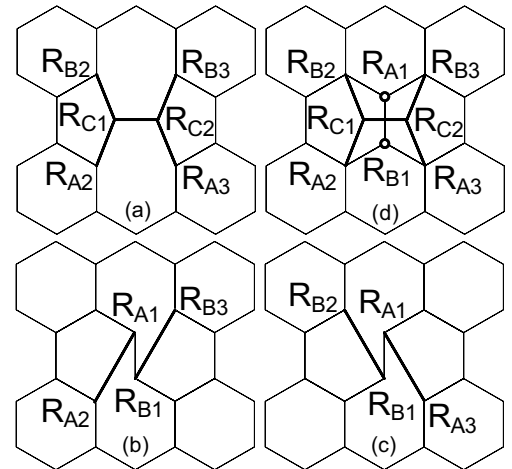

Fig. 50 (a) Stone-Wales defect in 2D graphite sheet. Bond alternation makes this type of defect, consisting of heptagons and pentagons. (b) and (c) Two ways to make non-local potential of the Stone-Wales defect in the $\boldsymbol{k}\cdot\boldsymbol{p}$ scheme. In this case, bond alternation is asymmetric contrary to the original defect. (d) Another way of making a Stone-Wales defect. The bond potential becomes symmetric.
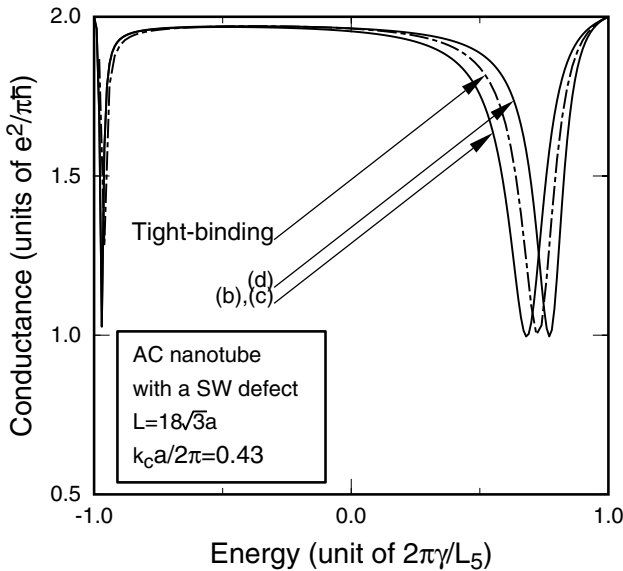
Fig. 51   Conductance of armchair nanotubes $L = \sqrt{3}ma$ ($m = 18$) with a Stone-Wales defect. Results of tight-binding calculation are also plotted in a dot-dashed line.

The results in the $\boldsymbol{k \cdot p}$ scheme are in good agreement with tight-binding results.

The two-dip structure corresponds to the case of a pair of vacancies at A and B sites although two dips lie at positions asymmetric around $\varepsilon = 0$. A Stone-Wales defect can be obtained by first removing a pair of neighboring A and B sites and then adding a pair in the perpendicular direction. The above result shows that the removal of a pair is likely to be more dominant than the addition of nonlocal transfer between neighboring sites.

Effects of a magnetic field can be studied also.[28] The conductance is scaled completely by the field component in the direction of a defect and the field-dependence is similar to that of an A and B pair defect. The bond alternation manifests itself as a small conductance plateau in high magnetic fields. The conductance of CN with $L/a = 10\sqrt{3}$ containing a Stone-Wales defect has been calculated by pseudopotential method.[193]

§**11. Summary**

Electronic and transport properties of carbon nanotubes have been discussed from a theoretical point of view. The effective-mass or $\boldsymbol{k \cdot p}$ scheme is particularly suitable for understanding global and essential features. In this scheme, the motion of electrons in carbon nanotubes is described by Weyl's equation for a massless neutrino with a helicity. As a result, electrons in nanotubes can be regarded as (charged) neutrinos on the cylinder surface with a fictitious Aharonov-Bohm magnetic flux. The amount of the flux, determined by the structure of nanotubes, vanishes in metallic nanotubes but is nonzero in semiconducting tubes.

In particular, we have exotic transport properties of metallic nanotubes such as the absence of backward scattering and the conductance quantization in the presence of scatterers unless the potential range is smaller than the lattice constant, the presence of a perfectly conducting channel when several bands coexist and its sensitivity to

various symmetry breaking effects, and a conductance quantization in the presence of strong and short-range scatterers such as lattice vacancies. At high temperatures scattering by phonons starts to play some role, but is not important in metallic nanotubes because conventional deformation potential coupling is absent and only much smaller coupling through bond-length change contributes to the scattering. On the other hand, semiconducting nanotubes do not have such peculiar properties because of the presence of deformation-potential scattering but behave like conventional quasi-1D systems such as quantum wires fabricated on semiconductor heterostructures.

Optical properties of semiconducting nanotubes are interesting because of one-dimensional nature. In fact, optical absorption is appreciable only for the light polarization parallel to the axis and almost all the intensity is transfered to excitons from continuum interband transitions. A band-gap renormalization due to electron-electron interactions play important roles also. Further, the band structure is strongly modified by magnetic flux due to Aharonov-Bohm effects.

By a pair of five- (pentagon) and seven-membered (heptagon) rings, two nanotubes with different diameter and structure can be connected to each other. The presence of such a topological defect leads to interesting boundary conditions on the wave function such that the K and K' points are exchanged as well as A and B sublattices. For junctions between metallic nanotubes, the conductance exhibits a characteristic power-law dependence on the junction length. Such topological effects are absent for a Stone-Wales defect consisting of two heptagon-pentagon pairs next to each other.

1) S. Iijima: Nature (London) **354** (1991) 56.
2) S. Iijima, T. Ichihashi, and Y. Ando: Nature (London) **356** (1992) 776.
3) S. Iijima and T. Ichihashi: Nature (London) **363** (1993) 603.
4) D. S. Bethune, C. H. Kiang, M. S. de Vries, G. Gorman, R. Savoy, J. Vazquez, and R. Beyers: Nature (London) **363** (1993) 605.
5) N. Hamada, S. Sawada, and A. Oshiyama: Phys. Rev. Lett. **68** (1992) 1579.
6) J. W. Mintmire, B. I. Dunlap, and C. T. White: Phys. Rev. Lett. **68** (1992) 631.
7) M. S. Dresselhaus, G. Dresselhaus, and R. Saito: Phys. Rev. B **45** (1992) 6234.
8) R. Saito, M. Fujita, G. Dresselhaus, and M. S. Dresselhaus: Phys. Rev. B **46** (1992) 1804.
9) K. Tanaka, K. Okahara, M. Okada and T. Yamabe:

Chem. Phys. Lett. **191** (1992) 469.

10) Y. D. Gao and W. C. Herndon: Mol. Phys. **77** (1992) 585.

11) D. H. Robertson, D. W. Brenner, and J. W. Mintmire: Phys. Rev. B **45** (1992) 12592.

12) H. Ajiki and T. Ando: J. Phys. Soc. Jpn. **62** (1993) 1255.

13) H. Ajiki and T. Ando: J. Phys. Soc. Jpn. **62** (1993) 2470. [Errata: J. Phys. Soc. Jpn. **63** (1994) 4267.]

14) H. Ajiki and T. Ando: Physica B **201** (1994) 349; Jpn. J. Appl. Phys. Suppl. **34-1** (1995) 107.

15) T. Ando: J. Phys. Soc. Jpn. **66** (1997) 1066.

16) T. Ando: J. Phys. Soc. Jpn. **73** (2004) 3351.

17) H. Sakai, H. Suzuura, and T. Ando: J. Phys. Soc. Jpn. **72** (2003) 1698; Physica E **22** (2004) 704.

18) N. A. Viet, H. Ajiki, and T. Ando: J. Phys. Soc. Jpn. **63** (1994) 3036.

19) H. Suzuura and T. Ando: *Proceedings of 25th International Conference on the Physics of Semiconductors*, edited by N. Miura and T. Ando (Springer, Berlin, 2001), p. 1525.

20) H. Ajiki and T. Ando: J. Phys. Soc. Jpn. **64** (1995) 260; *ibid* **65** (1996) 2976; Physica B **227** (1996) 342.

21) H. Ajiki and T. Ando: J. Phys. Soc. Jpn. **64** (1995) 4382.

22) T. Ando: J. Phys. Soc. Jpn. **69** (2000) 1757.

23) T. Yaguchi and T. Ando: J. Phys. Soc. Jpn. **70** (2001) 3641; *ibid* **71** (2002) 2224; Physica E **18** (2003) 220; *ibid* **22** (2004) 692.

24) T. Ando and T. Nakanishi: J. Phys. Soc. Jpn. **67** (1998) 1704.

25) T. Ando and H. Suzuura: J. Phys. Soc. Jpn. **71** (2002) 2753.

26) T. Ando, T. Nakanishi, and M. Igami: J. Phys. Soc. Jpn. **68** (1999) 3994.

27) H. Matsumura and T. Ando: J. Phys. Soc. Jpn. **67** (1998) 3542; *ibid* **70** (2001) 2401; Mol. Crys. Liq. Crys. **340** (2000) 725; *Proceedings of 25th International Conference on the Physics of Semiconductors*, edited by N. Miura and T. Ando (Springer, Berlin, 2001), p. 1655.

28) H. Matsumura and T. Ando: J. Phys. Soc. Jpn. **70** (2001) 2657.

29) H. Suzuura and T. Ando: Physica E **6** (2000) 864; Mol. Cryst. Liq. Cryst. **340** (2000) 731; Phys. Rev. B **65** (2002) 235412.

30) M. S. Dresselhaus, G. Dresselhaus, and P. C. Eklund: *Science of Fullerenes and Carbon Nanotubes*, (Academic Press 1996).

31) H. Ajiki and T. Ando: Solid State Commun. **102** (1997) 135.

32) R. Saito, G. Dresselhaus and M. S. Dresselhaus: *Physical Properties of Carbon Nanotubes*, (Imperial College Press, London, 1998).

33) P. J. F. Harris: *Carbon Nanotubes and Related Structures: New Materials for the Twenty-First Century* (Cambridge University Press, Cambridge, 1999).

34) T. Ando: Semicond. Sci. & Technol. **15** (2000) R13.

35) *Carbon Nanotubes: Synthesis, Structure, Properties, and Applications*, edited by M. S. Dresselhaus, G. Dresselhaus, and P. Avouris (Springer-Verlag, Berlin, 2000).

36) M. S. Dresselhaus and P. C. Eklund: Adv. Phys. **49** (2000) 705.

37) S. Reich, C. Thomsen, and J. Maultzsch: *Carbon Nanotubes* (Wiley-VCH, Weinheim, 2004).

38) X. Blase, L. X. Benedict, E. L. Shirley, and S. G. Louie: Phys. Rev. Lett. **72** (1994) 1878.

39) K. Kanamitsu and S. Saito: J. Phys. Soc. Jpn. **71** (2002) 483.

40) M. V. Berry: Proc. Roy. Soc. London **A392** (1984) 45.

41) B. Simon: Phys. Rev. Lett. **51** (1983) 2167.

42) N. H. Shon and T. Ando: J. Phys. Soc. Jpn. **67** (1998) 2421.

43) T. Ando, Y. Zheng, and H. Suzuura: J. Phys. Soc. Jpn. **71** (2002) 1318.

44) Y. Zheng and T. Ando: Phys. Rev. B **65** (2002) 245420.

45) W. -D. Tian and S. Datta: Phys. Rev. B **49** (1994) 5097.

46) S. Zaric, G. N. Ostojic, J. Kono, J. Shaver, V. C. Moore, M. S. Strano, R. H. Hauge, R. E. Smalley, and X. Wei: Science **304** (2004) 1129.

47) H. Ajiki and T. Ando: J. Phys. Soc. Jpn. **65** (1996) 505.

48) R. Saito, G. Dresselhaus, and M. S. Dresselhaus: Phys. Rev. B **50** (1994) 14698. [Erratum, Phys. Rev. B, **53**, 10408 (1996).]

49) T. Ando and T. Seri: J. Phys. Soc. Jpn. **66** (1997) 3558.

50) C. L. Kane and E. J. Mele: Phys. Rev. Lett. **78** (1997) 1932.

51) L. Yang, M. P. Anantram, J. Han, and J. P. Lu: Phys. Rev. B **60** (1999) 13874.

52) L. Yang and J. Han: Phys. Rev. Lett. **85** (2000) 154.

53) C. L. Kane, E. J. Mele, R. S. Lee, J. E. Fischer, P. Petit, H. Dai, A. Thess, R. E. Smalley, A. R. M. Verschueren, S. J. Tans, and C. Dekker: Europhys. Lett. **41** (1998) 683.

54) H. Suzuura and T. Ando: *Nanonetwork Materials*, edited by S. Saito, T. Ando, Y. Iwasa, K. Kikuchi, M. Kobayashi, and Y. Saito (American Institute of Physics, New York, 2001), p. 269.

55) S. M. Bachilo, M. S. Strano, C. Kittrell, R. H. Hauge, R. E. Smalley, and R. B. Weisman: Science **298** (2002) 2361.

56) A. Hagen and T. Hertel: Nano Lett. **3** (2003) 383.

57) J. W. McClure: Phys. Rev. **104** (1956) 666.

58) J. Heremans, C. H. Olk, and D. T. Morelli: Phys. Rev. B **49** (1994) 15122.

59) J. P. Lu: Phys. Rev. Lett. **74** (1995) 1123.

60) S. Zaric, G. N. Ostojic, J. Kono, J. Shaver, V. C. Moore, R. H. Hauge, R. E. Smalley, and X. Wei: Nano Lett. **4** (2004) 2219.

61) J. W. Wildoer, L. C. Venema, A. G. Rinzler, R. E. Smalley, and C. Dekker: Nature (London) **391** (1998) 59.

62) T. W. Odom, J. -L. Huang, P. Kim, and C. M. Lieber: Nature **391** (1998) 62.

63) See, for example, A. G. S. Filho, A. Jorio, G. Dresselhaus, M. S. Dresselhaus, R. Saito, A. K. Swan, M. S. Ünlü, B. B. Goldberg, J. H. Hafner, C. M. Lieber, and M. A. Pimenta: Phys. Rev. B **65** (2002) 035404, and references cited therein.

64) E. A. Taft and H. R. Philipp: Phys. Rev. **138** (1965) A197.

65) L. Wang, P. S. Davids, A. Saxena, and A. R. Bishop: Phys. Rev. B **46** (1992) 7175.

66) M. -F. Lin and K. W. -K. Shung: Phys. Rev. B **47**

(1993) 6617; *ibid* **48** (1993) 5567.

67) O. Sato, Y. Tanaka, M. Kobayashi, and A. Hasegawa: Phys. Rev. B **48** (1993) 1947.

68) P. J. Lin-Chung and A. K. Rajagopal: Phys. Rev. B **49** (1994) 8454.

69) T. M. Rice: Ann. Phys. (N.Y.) **31** (1965) 100.

70) D. F. Du Bois: Ann. Phys. (N.Y.) **7** (1959) 174.

71) S. Tomonaga: Prog. Theor. Phys. **5** (1950) 544.

72) J. M. Luttinger: J. Math. Phys. **4** (1963) 1154.

73) L. Balents and M. P. A. Fisher: Phys. Rev. B **55** (1997) 11973.

74) Yu. A. Krotov, D. -H. Lee, and S. G. Louie: Phys. Rev. Lett. **78** (1997) 4245.

75) C. Kane, L. Balents, and M. P. A. Fisher: Phys. Rev. Lett. **79** (1997) 5086.

76) R. Egger and A. O. Gogolin: Eur. Phys. J. B **3** (1998) 281.

77) H. Yoshioka and A. A. Odintsov: Phys. Rev. Lett. **82** (1999) 374.

78) D. H. Cobden, M. Bockrath, P. L. McEuen, A. G. Rinzler, and R. E. Smalley: Phys. Rev. Lett. **81** (1998) 681.

79) S. J. Tans, M. H. Devoret, R. J. A. Groeneveld, and C. Dekker: Nature (London) **394** (1998) 761.

80) M. Bockrath, D. H. Cobden, L. Jia, A. G. Rinzler, R. E. Smalley, L. Balents, and P. L. McEuen: Nature (London) **397** (1999) 598.

81) H. Ishii, H. Kataura, H. Shiozawa, H. Yoshioka, H. Otsubo, Y. Takayama, T. Miyahara, S. Suzuki, Y. Achiba, M. Nakatake, T. Narimura, M. Higashiguchi, K. Shimada, H. Namatame, and M. Taniguchi: Nature **426** (2003) 540.

82) J. Voit: Phys. Rev. B **47** (1993) 6740.

83) V. Meden and K. Schonhammer: Phys. Rev. B **46** (1992) 15753.

84) R. Loudon: Am. J. Phys. **27** (1959) 649.

85) R. J. Elliot and R. Loudon: J. Phys. Chem. Solids **8** (1959) 382; *ibid* **15** (1960) 196.

86) T. Ogawa and T. Takagahara: Phys. Rev. B **43** (1991) 14325; *ibid* **44** (1991) 8138.

87) H. Kataura, Y. Kumazawa, Y. Maniwa, I. Umezu, S. Suzuki, Y. Ohtsuka and Y. Achiba: Synth. Met. **103** (1999) 2555.

88) M. Ichida, S. Mizuno, Y. Tani, Y. Saito, and A. Nakamura: J. Phys. Soc. Jpn. **68** (1999) 3131.

89) M. Ichida, S. Mizuno, Y. Saito, H. Kataura, Y. Achiba, and A. Nakamura: Phys. Rev. B **65** (2002) 241407.

90) M. J. O'Connell, S. M. Bachilo, C. B. Huffman, V. C. Moore, M. S. Strano, E. H. Haroz, K. L. Rialon, P. J. Boul, W. H. Noon, C. Kittrell, J. Ma, R. H. Hauge, R. B. Weisman, and R. E. Smalley: Science **297** (2002) 593.

91) S. Lebedkin, K. Arnold, F. Hennrich, R. Krupke, B. Renker, and M. M. Kappes: New J. Phys. **5** (2003) 140.

92) R. B. Weisman and S. M. Bachilo: Nano Lett. **3** (2003) 1235.

93) Ge. G. Samsonidze, R. Saito, N. Kobayashi, A. Grüneis, J. Jiang, A. Jorio, S. G. Chou, G. Dresselhaus, and M. S. Dresselhaus: Appl. Phys. Lett. **85** (2004) 5703.

94) T. Miyake and S. Saito: Phys. Rev. B **68** (2003) 155424.

95) C. D. Spataru, S. Ismail-Beigi, L. X. Benedict, and S. G. Louie: Phys. Rev. Lett. **92** (2004) 077402.

96) E. Chang, G. Bussi, A. Ruini, and E. Molinari: Phys. Rev. Lett. **92** (2004) 196401.

97) Z. M. Li, H. J. Liu, J. T. Ye, C. T. Chan, and Z. K. Tang: Appl. Phys. A **78** (2004) 1121.

98) T. G. Pedersen: Phys. Rev. B **67** (2003) 073401.

99) V. Perebeinos, J. Tersoff, and Ph. Avouris: Phys. Rev. Lett. **92** (2004) 257402.

100) T. Ando, T. Nakanishi, and R. Saito: J. Phys. Soc. Jpn. **67** (1998) 2857.

101) See, for example: *Anderson Localization*, edited by Y. Nagaoka and H. Fukuyama (Springer, Berlin, 1982); *Localization, Interaction, and Transport Phenomena*, edited by B. Kramer, G. Bergmann, and Y. Bruynseraede (Springer, Berlin, 1984); P. A. Lee and T. V. Ramakrishnan: Rev. Mod. Phys. **57** (1985) 287; *Anderson Localization*, edited by T. Ando and H. Fukuyama (Springer, Berlin, 1988); D. J. Thouless: Phys. Reports C **13** (1974) 93; G. Bergmann: Phys. Rept. **107** (1984) 1.

102) J. E. Fischer, H. Dai, A. Thess, R. Lee, N. M. Hanjani, D. L. Dehaas, and R. E. Smalley: Phys. Rev. B **55** (1997) R4921.

103) M. Bockrath, D. H. Cobden, P. L. McEuen, N. G. Chopra, A. Zettl, A. Thess, and R. E. Smalley: Science **275** (1997) 1922.

104) S. J. Tans, M. H. Devoret, H. Dai, A. Thess, R. E. Smalley, L. J. Geerligs, and C. Dekker: Nature (London) **386** (1997) 474.

105) S. J. Tans, R. M. Verschuren, and C. Dekker: Nature (London) **393** (1998) 49.

106) A. Bezryadin, A. R. M. Verschueren, S. J. Tans, and C. Dekker: Phys. Rev. Lett. **80** (1998) 4036.

107) P. L. McEuen, M. Bockrath, D. H. Cobden, Y. -G. Yoon, and S. G. Louie: Phys. Rev. Lett. **83** (1999) 5098.

108) A. Bachtold, M. S. Fuhrer, S. Plyasunov, M. Forero, E. H. Anderson, A. Zettl, and P. L. McEuen: Phys. Rev. Lett. **84** (2000) 6082.

109) J. Tersoff: Appl. Phys. Lett. **74** (1999) 2122.

110) M. P. Anantram, S. Datta, and Y. -Q. Xue: Phys. Rev. B **61** (2000) 14219.

111) K. -J. Kong, S. -W. Han, and J. -S. Ihm: Phys. Rev. B **60** (1999) 6074.

112) H. J. Choi, J. Ihm, Y. -G. Yoon, and S. G. Louie: Phys. Rev. B **60** (1999) R14009.

113) T. Nakanishi and T. Ando: J. Phys. Soc. Jpn. **69** (2000) 2175.

114) J. Kong, E. Yenilmez, T. W. Tombler, W. Kim, H. J. Dai, R. B. Laughlin, L. Liu, C. S. Jayanthi, and S. Y. Wu: Phys. Rev. Lett. **87** (2001) 106801.

115) R. Martel, T. Schmidt, H. R. Shea, T. Hertel, and Ph. Avouris: Appl. Phys. Lett. **73** (1998) 2447.

116) H. T. Soh, C. F. Quate, J. Kong, and H. -J. Dai: Appl. Phys. Lett. **75** (1999) 627.

117) R. Martel, V. Derycke, C. Lavoie, J. Appenzeller, K. K. Chan, J. Tersoff, and Ph. Avouris: Phys. Rev. Lett. **87** (2001) 256805.

118) J. Park and P. L. McEuen: Appl. Phys. Lett. **79** (2001) 1363.

119) A. Bachtold, P. Hadley, T. Nakanishi, and C. Dekker: Science **294** (2001) 1317.

120) J. Appenzeller, J. Knoch, V. Derycke, R. Martel, S. Wind, and Ph. Avouris: Phys. Rev. Lett. **89** (2002)

126801.

121) A. Bachtold, P. Hadley, T. Nakanishi, and C. Dekker: Physica E **16** (2003) 42.

122) F. J. Dyson: J. Math. Phys. **3** (1962) 140; *ibid* **3** (1962) 157; *ibid* **3** (1962) 166; *ibid* **3** (1962) 1191; *ibid* **3** (1962) 1199; *ibid* **4** (1963) 701; *ibid* **4** (1963) 713.

123) H. Akera and T. Ando: Phys. Rev. B **43** (1991) 11676.

124) T. Seri and T. Ando: J. Phys. Soc. Jpn. **66** (1997) 169.

125) T. Ando: J. Phys. Soc. Jpn. **71** (2002) 2505.

126) Y. Takane and K. Wakabayashi: J. Phys. Soc. Jpn. **72** (2003) 2710.

127) Y. Takane: J. Phys. Soc. Jpn. **73** (2004) 9.

128) T. Ando: J. Phys. Soc. Jpn. **73** (2004) 1273.

129) T. Ando and K. Akimoto: J. Phys. Soc. Jpn. **73** (2004) 1895.

130) K. Akimoto and T. Ando: J. Phys. Soc. Jpn. **73** (2004) 2194.

131) S. N. Song, X. K. Wang, R. P. H. Chang, and J. B. Ketterson: Phys. Rev. Lett. **72** (1994) 697.

132) L. Langer, V. Bayot, E. Grivei, J. -P. Issi, J. P. Heremans, C. H. Olk, L. Stockman, C. Van Haesendonck, and Y. Bruynseraede: Phys. Rev. Lett. **76** (1996) 479.

133) A. Yu. Kasumov, I. I. Khodos, P. M. Ajayan, and C. Colliex: Europhys. Lett. **34** (1996) 429.

134) T. W. Ebbesen, H. J. Lezec, H. Hiura, J. W. Bennett, H. F. Ghaemi, and T. Thio: Nature (London) **382** (1996) 54.

135) H. Dai, E.W. Wong, and C. M. Lieber: Science **272** (1996) 523.

136) A. Yu. Kasumov, H. Bouchiat, B. Reulet, O. Stephan, I. I. Khodos, Yu. B. Gorbatov, and C. Colliex: Europhys. Lett. **43** (1998) 89.

137) A. Bachtold, C. Strunk, J. P. Salvetat, J. M. Bonard, L. Forro, T. Nussbaumer, and C. Schönenberger: Nature (London) **397** (1999) 673.

138) C. Schönenberger, A. Bachtold, C. Strunk, J. -P. Salvetat, and L. Forró: Appl. Phys. A **59** (1999) 283.

139) A. Fujiwara, K. Tomiyama, H. Suematsu, M. Yumura, and K. Uchida: Phys. Rev. B **60** (1999) 13492.

140) S. Frank, P. Poncharal, Z. L. Wang, and W. A. de Heer: Science **280** (1998) 1744.

141) A. Urbina, I. Echeverría, A. Pérez-Garrido, A. Díaz-Sánchez, and J. Abellán: Phys. Rev. Lett. **90** (2003) 106603.

142) J. Cumings and A. Zettl: Phya. Rev. Lett. **93** (2004) 086801.

143) R. Saito, M. Fujita, G. Dresselhaus, and M. S. Dresselhaus: Mater. Sci. Eng. B **19** (1993) 185.

144) Y. -K. Kwon and D. Tomanek: Phys. Rev. B **58** (1998) R16001.

145) S. Sanvito, Y. -K. Kwon, D. Tomanek, and C. J. Lambert: Phys. Rev. Lett. **84** (2000) 1974.

146) P. Kim, L. Shi, A. Majumdar, and P. L. McEuen: Phys. Rev. Lett. **87** (2001) 215502.

147) D. -H. Kim and K. J. Chang: Phys. Rev. B **66** (2002) 155402.

148) Ph. Lambin, V. Meunier, and A. Rubio: Phys. Rev. B **62** (2000) 5129.

149) K. -H. Ahn, Y. -H. Kim, J. Wiersig, and K. J. Chang: Phys. Rev. Lett. **90** (2003) 026601.

150) S. Roche, F. Triozon, A. Rubio, and D. Mayou: Phys. Rev. B **64** (2001) 121401.

151) Y. -G. Yoon, P. Delaney, and S. G. Louie: Phys. Rev. B **66** (2002) 073407.

152) F. Triozon, S. Roche, A. Rubio, and D. Mayou: Phys. Rev. B **69** (2004) 121410(R).

153) S. Uryu: Phys. Rev. B **69** (2004) 075402.

154) A. A. Maarouf, C. L. Kane, and E. J. Mele: Phys. Rev. B **61** (2000) 11156.

155) T. Nakanishi and T. Ando: J. Phys. Soc. Jpn. **70** (2001) 1647.

156) R. Saito, T. Takeya, and T. Kimura, G. Dresselhaus, and M. S. Dresselhaus: Phys. Rev. B **57** (1998) 4145.

157) R. A. Jishi, M. S. Dresselhaus, and G. Dresselhaus: Phys. Rev. B **47** (1993) 16671.

158) L. M. Woods and G. D. Mahan: Phys. Rev. B **61** (2000) 10651; G. D. Mahan: Phys. Rev. B **65** (2002) 235402; G. D. Mahan and G. S. Jeon: Phys. Rev. **70** (2004) 75405.

159) O. Dubay, G. Kresse, and H. Kuzmany: Phys. Rev. Lett. **88** (2002) 235506; O. Dubay and G. Kresse: Phys. Rev. B **67** (2003) 035401.

160) See for example, W. A. Harrison: *Electronic Structure and the Properties of Solids* (W.H. Freeman and Company, San Francisco, 1980).

161) A. S. Maksimenko and G. Ya. Slepyan: Phys. Rev. Lett. **84** (2000) 362.

162) H. A. Mizes and J. S. Foster: Science **244** (1989) 559.

163) O. Zhou, R. M. Fleming, D. W. Murphy, R. C. Haddon, A. P. Ramirez, and S. H. Glarum: Science **263** (1994) 1744.

164) S. Amelinckx, D. Bernaerts, X. B. Zhang, G. Van Tendeloo, and J. Van Landuyt: Science **267** (1995) 1334.

165) M. Fujita, K. Wakabayashi, K. Nakada and K. Kusakabe: J. Phys. Soc. Jpn. **65** (1996) 1920.

166) L. Chico, L. X. Benedict, S. G. Louie, and M. L. Cohen: Phys. Rev. B **54** (1996) 2600. [Errata: Phys. Rev. B **61** (2000) 10511.]

167) M. Igami, T. Nakanishi, and T. Ando: J. Phys. Soc. Jpn. **68** (1999) 716; *ibid* **68** (1999) 3146; Physica B **284-288** (2000) 1746; Mol. Cryst. Liq. Cryst. **340** (2000) 719.

168) M. Igami, T. Nakanishi, and T. Ando: J. Phys. Soc. Jpn. **70** (2001) 481.

169) H. J. Choi, J. -S. Ihm, S. G. Louie, and M. L. Cohen: Phys. Rev. Lett. **84** (2000) 2917.

170) B. I. Dunlap: Phys. Rev. B **46** (1992) 1933; *ibid* **49** (1994) 5643; *ibid* **50** (1994) 8134.

171) R. Saito, G. Dresselhaus, and M. S. Dresselhaus: Phys. Rev. B **53** (1996) 2044.

172) L. Chico, V. H. Crespi, L. X. Benedict, S. G. Louie, and M. L. Cohen: Phys. Rev. Lett. **76** (1996) 971.

173) R. Tamura and M. Tsukada: Phys. Rev. B **55** (1997) 4991; Z. Phys. D **40** (1997) 432; Phys. Rev. B **58** (1998) 8120; J. Phys. Soc. Jpn. **68** (1999) 910; Phys. Rev. B **61** (2000) 8548.

174) J. Han, M. P. Anantram, R. L. Jaffe, J. Kong, and H. Dai: Phys. Rev. B **57** (1998) 14983.

175) V. Meunier, L. Henrard, and Ph. Lambin: Phys. Rev. B **57** (1998) 2586.

176) Z. Yao, H. W. C. Postma, L. Balents, and C. Dekker: Nature (London) **402** (1999) 273.

177) M. Menon and D. Srivastava: Phys. Rev. Lett. **79**

(1997) 4453.

178) J. Li, C. Papadopoulos, and J. Xu: Nature (London) **402** (1999) 253.

179) G. Treboux, P. Lapstun, Z. Wu, and K. Silverbrook: J. Phys. Chem. B **47** (1999) 8671; G. Treboux: *ibid* **47** (1999) 10381.

180) A. J. Stone and D. J. Wales: Chem. Phys. Lett. **128** (1986) 501.

181) S. Itoh and S. Ihara: Phys. Rev. B **48** (1993) 8323.

182) V. Meunier, Ph. Lambin, and A. A. Lucas: Phys. Rev. B **57** (1998) 14886.

183) V. Ivanov, J. B. Nagy, Ph. Lambin, A. A. Lucas, X. B. Zhang, X. F. Zhang, D. Bernaerts, G. van Tendeloo, S. Amelinckx, and J. van Lunduyt: Chem. Phys. Lett. **223** (1994) 329.

184) S. Ihara and S. Itoh: Carbon **33** (1995) 931.

185) K. Akagi, R. Tamura, M. Tsukada, S. Itoh, and S. Ihara: Phys. Rev. Lett. **74** (1995) 2307.

186) S. Iijima, M. Yudasaka, R. Yamada, S. Bandow, K. Suenaga, F. Kokai, and K. Takahashi: Chem. Phys. Lett. **309** (1999) 165.

187) T. Nakanishi and T. Ando: J. Phys. Soc. Jpn. **66** (1997) 2973.

188) S. Iijima: Mater. Sci. Eng. **B19** (1993) 172.

189) Y. Saito, K. Hata, and T. Murata: Jpn. J. Appl. Phys. **39** (2000) 271

190) R. Tamura and M. Tsukada: Phys. Rev. B **52** (1995) 6015.

191) D. L. Carroll, P. Redlich, P. M. Ajayan, J. C. Charlier, X. Blase, A. De Vita, and R. Car: Phys. Rev. Lett. **78** (1997) 2811.

192) P. Kim, T. W. Odom, J. -L. Huang, and C. M. Lieber: Phys. Rev. Lett. **82** (1999) 1225.

193) H. J. Choi and J. Ihm: Phys. Rev. B **59** (1999) 2267.